ISSN en trámite

Geofísica Internacional

Revista Trimestral Publicada por el Instituto de Geofísica de la Universidad Nacional Autónoma de México

México
Volume 55 Number 4
October - December
2016

— Geofísica Internacional —

GEOFÍSICA INTERNACIONAL, Año 55, Vol. 55, Núm. 4, octubre - diciembre de 2016 es una publicación trimestral, editada por la Universidad Nacional Autónoma de México, Ciudad Universitaria, Alcaldía Coyoacán, C.P. 04150, Ciudad de México, a través del Instituto de Geofísica, Circuito de la Investigación Científica s/n, Ciudad Universitaria, Alcaldía Coyoacán, C.P. 04150, Ciudad de México, Tel. (55)56 22 41 15. URL: http://revistagi.geofisica.unam.mx, correo electrónico: revistagi@igeofisica.unam.mx. Editora responsable: Andrea Rostan Robledo. Certificado de Reserva de Derechos al uso Exclusivo del Título: 04-2022-081610251200-102, ISSN: en trámite, otorgados por el Instituto Nacional del Derecho de Autor (INDAUTOR). Responsable de la última actualización Saúl Armendáriz Sánchez, Editor Técnico. Fecha de la última modificación: 30 de septiembre 2016, Circuito de la Investigación Científica s/n, Ciudad Universitaria, Alcaldía Coyoacán, C.P. 04150, Ciudad de México.

Geofísica Internacional

Vol. 55, Núm. 4, octubre-diciembre de 2016

Contents

Geofísica Internacional (2016) 55-4: 227-238

Original paper

Resistivity and induced polarization to support morphological modeling in limestone mining

Antonio Carlos Martins, Vagner Elis, Giorgio de Tomi*, Jorge Bettencourt and Tatiane Marin

Received: July 16, 2015; accepted: August 09, 2016; published on line: October 01, 2016

DOI: 10.19155/geofint.2016.055.4.1

Resumen

Este artículo presenta los resultados de la aplicación de estudios geofísicos usados para la actualización del modelo morfológico de un depósito de caliza y gneis perteneciente a una compañía minera cerca de la ciudad de Taubaté, estado de Sao Paulo, Brasil. La investigación comenzó con un test de verificación de exactitud del método geofísico de estudio, el cual fue realizado con una campaña de perforación realizada previamente en la misma área de estudio, con el objetivo de confirmar la posibilidad de utilizar los métodos de Sondeo Eléctrico Vertical (SEV) y de Polarización Inducida (IP) para obtener la información requerida para el modelado del depósito morfológico. Como resultado, la aplicación de los métodos geofísicos en el área de estudio redujo el tiempo de recolección hasta un 75% y presentaron un nivel de precisión similar al de los métodos de exploración convencionales utilizados para los mismos objetivos del estudio.

Palabras clave: Geofísica, electro resistividad, polarización inducida, modelado morfológico, minería de caliza.

Abstract

This paper presents the results of the application of geophysical surveys to update the morphological model of a limestone and gneiss deposit of a mining company near the city of Taubaté, Brazil. The research began with a test to verify the accuracy of the geophysical survey method and it was conducted in the same area as a previous drilling campaign with the aim of confirming the possibility of using Vertical Electrical Sounding (VES) and induced polarization (IP) methods, in order to obtain the required information for the deposit morphological modeling. As a result, the application of geophysical methods in the study area reduced up to 75% the data collection time and presented similar accuracy levels as conventional exploration methods used for the same research objectives.

Key words: Geophysics, electro-resistivity, induced polarization, morphological modeling, limestone mining.

A. C. Martins
Department of Mining and Petroleum Engineering
Universidade of São Paulo
São Paulo, Brazil

V. Elis
Professor Doctor II in the Geophysics Department at IAG/USP
Universidade of São Paulo
São Paulo, Brazil

G. de Tomi*
Professor of Mining Engineering and Director
USP Center for Responsible Mining (NAP.Mineração)
Universidade of São Paulo
São Paulo, Brazil
*Corresponding author: gdetomi@usp.br

J. Bettencourt
Emeritus Professor of the Geosciences Institute at the
Universidade of São Paulo
São Paulo, Brazil

T. Marin
Department of Mining and Petroleum Engineering
Universidade of São Paulo
São Paulo, Brazil

Introduction

Geophysical surveys were employed to update the morphological model of a mineral deposit owned by an aggregate mining company located near the city of Taubaté, Brazil. The company owns a mining title encompassing an area of 50 ha and it has recently applied for an extension of its mining title to an exploration permit for an area of 246 ha, as shown in Figure 1 (UTM SF-23). The deposit is a limestone orebody surrounded by gneiss. The company traditionally produces limestone and gneiss for aggregates. A new exploitation stage is planned for the extended exploration permit, which will be focused on the gneiss occurrence. For the planning of this new stage, it is important to know the thickness of the layer of soil above the gneiss bedrock.

The purpose of this paper is to describe the application of geophysics in order to streamline data collection for updating of the morphological model in the area of the new mining title of the company to meet the time limits specified by the company. Due to the low cost and the possibility of covering broad areas in a short time, geophysical methods are an important tool in mineral research (REM). Ravindran (2010) conducted a geoelectric resistivity survey along a 14-km transect at the boundary between Kericho and Nakuru counties (India) to observe the structure beneath and its relation to groundwater occurrence. In this case, 2D electrical resistivity (ER) imaging has proved to be an excellent tool to delineate groundwater potential zones and subsurface lithology. According to Frasheri *et al.* (1995), the most important geophysical methods used for this purpose are electrical prospecting, gravity, magnetics, and electromagnetics.

The conventional method that is usually used by the company for this type of data collection is based on rotary drilling holes with core recovery. However, due to the deadlines set by the company, an exploration campaign using the conventional procedures would take about 60 days to complete using between three and four drilling equipment units.

To reduce the time taken by the data collection required to update the morphological modeling of the deposit, geophysical methods were introduced that made it possible to obtain reliable data on the variables of interest (including the thickness of the soil layer and the depth of the top of the bedrock). According to

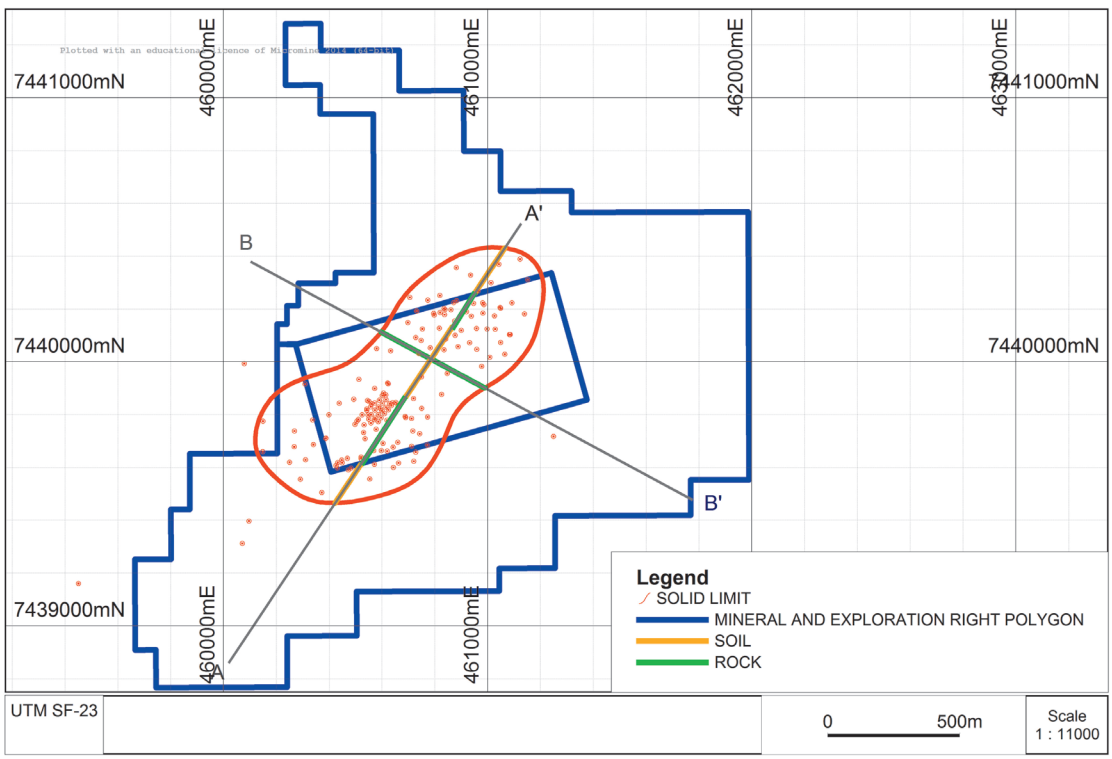

Figure 1. Current mining title (rectangle in the centre) with mining manifest and new title with exploration permit (external polygon).

Bery and Saad (2012), the resistivity method can be used for measuring soil electrical properties, and the ER was tested in different soil studies. Haile and Atsbaha (2014) comments that geophysical techniques are routinely used as part of geological investigations to provide information on site parameters and to map the subsurface geology and geological structures at the site. According to Ogilvy and Bogoslovsky (1979), observation of the changes in specific electrical resistivities with time on the slopes of quarries is an effective method of assessing slope stability and predicting landslide hazards.

The work began with a test to verify the accuracy of the geophysical methods used. The test was performed in the same location as an existing exploration campaign, which validated the compliance of the results of the geophysical survey with the data from drill cores. The feasibility of using the ER and induced polarization (time domain IP) methods to identify the geological contact between soil and bedrock was confirmed in this way. The technique chosen for data collection was vertical electrical sounding (VES) with a Schlumberger array. Due to the satisfactory results, 31 VESs have been planned and carried out in the southern portion of the new mining title area. Currently many surveys are performed with the VES technique. Atzemoglou *et al.* (2003) reports that a survey conducted in the NW Amynteon basin, by combining the interpretation of results of 1D VES, produced 2D and 3D results in full agreement with the local geology.

Geophysical methods and techniques used

Electrical Resistivity (ER) Method

The ER method uses an artificial electrical current that is introduced into the land through two electrodes (known as A and B) with the aim of measuring the potential generated in two other electrodes (known as M and N) near the current flow (Elis, 1999). The introduction of an electrical current into the land through the electrodes A, B, M, and N results in a power difference (ΔV), thus allowing the calculation of the apparent resistivity through the equation (1):

$$\rho_a = K\frac{\Delta V}{I}(ohm.m) \qquad (1)$$

Thus, it is possible to identify the different layers of soil, weathered rock, and bedrock through the resistivity values obtained in field trials.

Vertical Electrical Sounding (VES) Technique

The VES technique consists of a succession of chargeability and resistivity measurements made with the same type of array and increasing separation between the emission and reception electrodes and the center of the array (allocation point test), and its orientation is kept fixed (Figure 2).

This procedure allows for the observation of apparent resistivity and chargeability values at a fixed point, at increasing depths, by increasing the separation between the current electrodes A and B. There are several electrode arrays for field trials; however, the Schlumberger array was used in this research. This array was chosen because it has a superior vertical resolution and it is able to record higher quality data (especially IP data) than other arrangements. Another important advantage over alternative arrays (such as Wenner and others) is the possibility of improving the signal to noise ratio by moving only the MN electrodes during data acquisition.

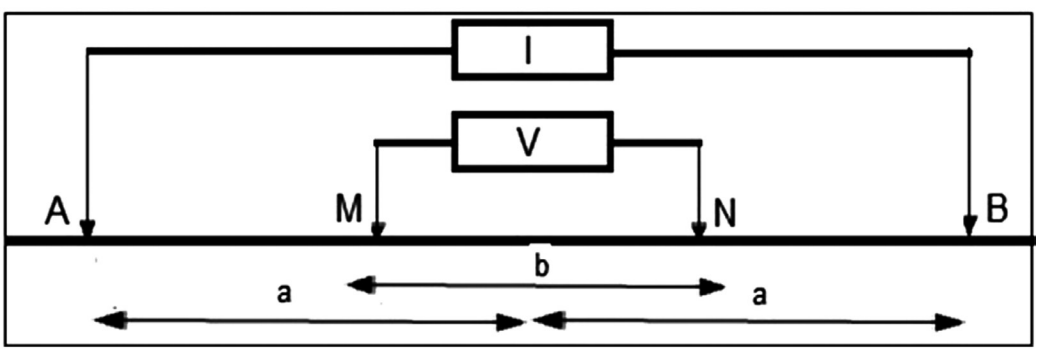

Figure 2. Arrangement in the field – VES Schlumberger array.

Induced Polarization (IP) Method

IP is a phenomenon stimulated by an electric current, observed as a delayed response to voltage in natural materials (Sumner, 1976). By establishing an electrical current flow through the electrodes A and B on the sur-face, a primary potential difference ΔVp is established. A (ΔVp) varies with time and acquires the shape of a curve ΔVIP = f(t). This curve connects the steady-state asymptote ΔVp with the zero asymptote after cutting the current. The method's concept is based on the amplitude of a ΔVIP (t) value and is related to the geological material's greater or lesser capacity to polarize, constituting, therefore, the basis of the method (Figure 3).

The decay curve can be studied as a whole or just sampled at some intervals of time (Telford *et al*., 1990).

The parameter measured in the IP (time domain) is called chargeability (M) and can be expressed in milliseconds (ms) or millivolts/ volt (mV/V):

$$M = \frac{1}{V_P}\int_{t1}^{t2} \Delta V_{IP}(t)dtmV / V \qquad (2)$$

According to Orellana (1972), the explanation for the IP phenomenon is commonly attributed to two factors: electrode polarization and membrane polarization. In this particular case, what prevailed was membrane polarization occurring in rocks with a low content of metal elements. The changes in clay content in the different layers of soil and bedrock caused different IP responses and therefore assisted in the individualization of the layers of interest.

Tests Conducted

Thirty-one VESs were planned and implemented in the southern portion of the exploration permit area shown on the map in Figure 4 and Table 1. According to Sahbi *et al*. (1997), when electric soundings are made over an irregular terrain, topographic effects can influence the values of apparent resistivity and lead to erroneous 1D interpretation. Due to this fact, VESs were not performed in very irregular locations to avoid this unwanted effect. VESs surveys were carried out with AB spacing varying between 200 and 500 m. The AB spacing has been adjusted according to the soil thickness. The depth of investigation was between 50 and 125 m, as shown in Table 2. The fitting errors between field data and the models varied between 2.9 and 9.4%.

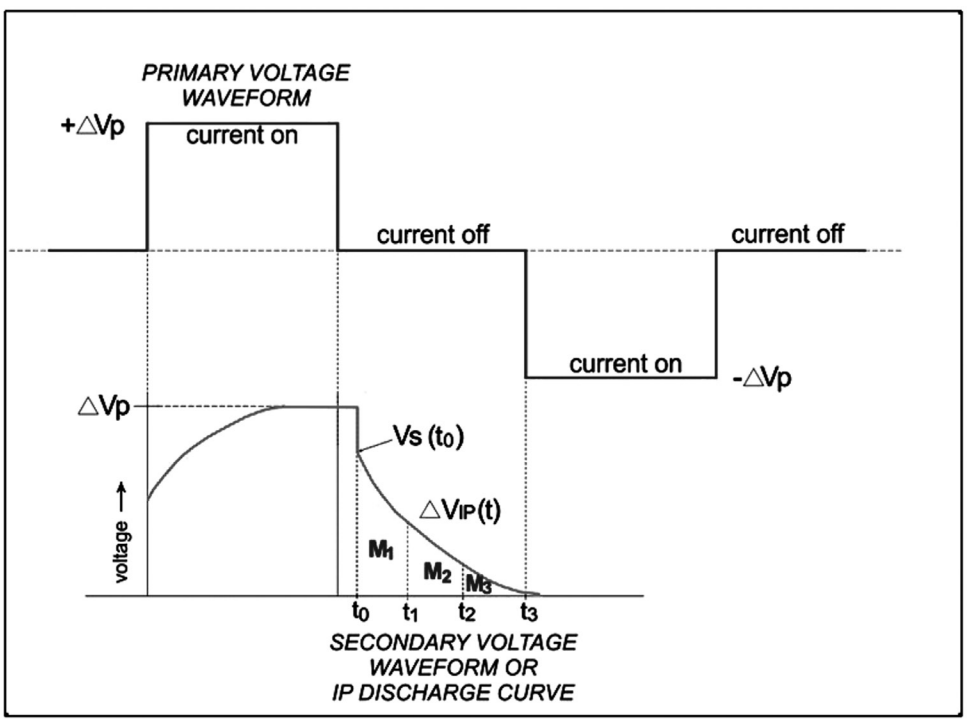

Figure 3. IP decay curve – time domain.

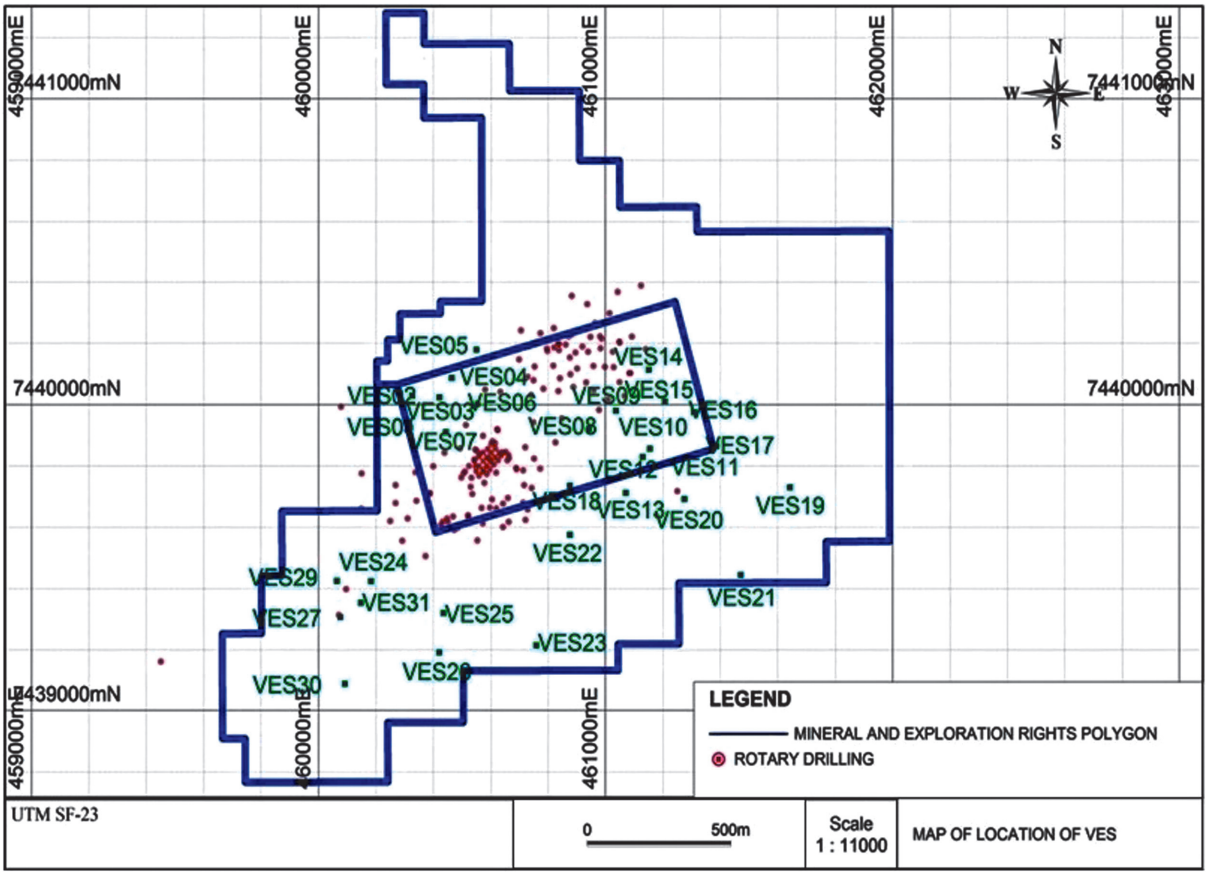

Figure 4. Location of the drill holes (as red dots) and the VESs (as green dots) within the area of interest.

Table 1. Coordinates of the VESs implemented in the area of interest (UTM SF-23).

Point	Coord UTM E-W	Coord UTM N-S	Point	Coord UTM E-W	Coord UTM N-S
VES 01	460272	7439974	VES 16	460272	7439890
VES 02	460292	7440072	VES 17	461323	7439776
VES 03	460390	7440046	VES 18	460810	7439708
VES 04	460440	7440103	VES 19	461562	7439608
VES 05	460530	7440217	VES 20	461193	7439613
VES 06	460465	7440008	VES 21	461365	7439346
VES 07	460394	7439931	VES 22	460776	7439552
VES 08	460889	7439888	VES 23	460622	7439201
VES 09	460991	7439935	VES 24	460080	7439474
VES 10	461093	7439772	VES 25	460318	7439337
VES 11	461153	7439735	VES 26	460283	7439194
VES 12	461063	7439772	VES 27	459959	7439368
VES 13	460999	7439659	VES 29	459962	7439499
VES 14	461111	7440079	VES 30	459948	7439144
VES 15	461163	7439947	VES 31	460036	7439407

Table 2. AB/2 and MN/2 spacing used during field acquisition.

AB/2	MN/2	K
1.5	0.5	6.28
2.0	0.5	11.78
3.0	0.5	27.48
4.0	0.5	49.48
5.0	0.5	77.75
6.0	0.5	112.31
6.0	1.0	54.98
8.0	0.5	200.18
8.0	1.0	98.91
10.0	0.5	313.35
10.0	1.0	155.43
12.0	1.0	224.51
15.0	1.0	351.68
15.0	2.0	173.57
20.0	1.0	626.75
20.0	2.0	311.01
25.0	2.0	487.73

AB/2	MN/2	K
30.0	2.0	703.71
40.0	2.0	1253.49
40.0	5.0	494.80
50.0	2.0	1960.35
50.0	5.0	777.54
60.0	5.0	1123.11
60.0	10.0	549.77
80.0	5.0	2020.70
80.0	10.0	989.10
100.0	5.0	3133.74
100.0	10.0	1555.09
150.0	5.0	7070.72
150.0	10.0	3518.58
200.0	5.0	12558.51
100.0	10.0	6267.47
250.0	5.0	19627.15
250.0	10.0	9801.79

In the area where the first test was conducted, the results showed that the layers of soil with higher porosity, higher clay content, and higher moisture content than the bedrock presented resistivity and chargeability values that allowed these materials to be differentiated. The VES tests were performed between the existing drill holes F02–F–121-02 and F06–F–99-03. These drill holes presented 27 to 30 m of soil on gneiss and/or weathered gneiss.

The VES results are shown in Figure 5 and Table 3 with a five-layer model. The fitting error was 6.9%. The first four layers characterize the topsoil and weathered gneiss soil/rock. The resistivity variations reflect the changes in porosity and moisture content that are a part of the soil's profile. The gneiss presents higher resistivity (1207 ohm.m) from 24.3 m deep, which is quite consistent with data from the drill holes.

The VES surveys were performed in order to separate the soil layers from the gneiss. The soil, due to its higher porosity, higher clay content, and higher moisture content than the compact rock, tends to have lower resistivity values.

Table 3. VES test conducted between drill holes F02–F–121-02 and F06–F–99-03.

Layer	r (ohm.m)	M (mV/V)	Top Depth	Interpretation
1	852	3.7	0	Alteration Soil
2	1174	12	2.1	Alteration Soil
3	489	1.1	5.7	Alteration Soil
4	136	5.4	10.4	Alteration Soil
5	1207	9.8	24.3	Gneiss/weathered Gneiss

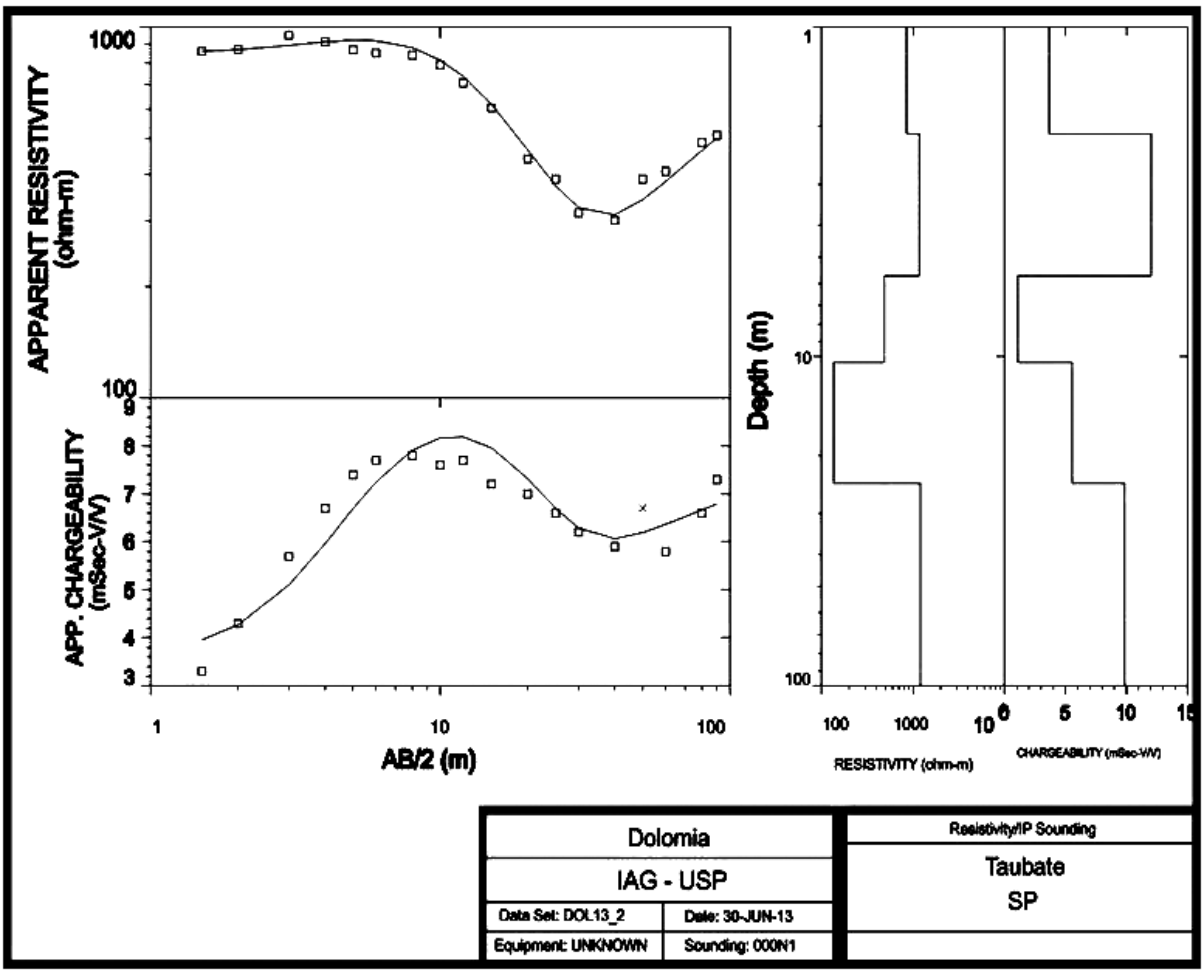

Figure 5. VES test conducted between drill holes F02– F–121-02 and F06–F–99-03.

Therefore, as resistivity is a property that responds to changes in the factors described above, it was the basis of the interpretation of the VES. According to Okay *et al*. (2013), IP is a geophysical method that is potentially sensitive to the presence of cracks in porous rocks. In this case, the chargeability data were used on a flat surface to assist in the definition of contacts and to refine the interpretation. In general, the curves show chargeability models with a higher value for the bedrock, but since this parameter is affected by small variations in the type and amount of clay minerals, some VESs showed a small decrease in chargeability for the last layer.

Discussion of Results

Layer Interpretation

The results show that it was possible to identify the layers of interest established according to the aims of the study.

Most VESs presented models of four layers. Layers 1, 2, and 3 were interpreted respectively as topsoil (low to medium resistivity, low to medium chargeability), unsaturated alteration soil (high resistivity due to low moisture content and medium chargeability), and saprolite or alteration soil (low to medium resistivity and low chargeability). The fourth layer typically showed high resistivity values (greater than 2000 ohm.m) and higher chargeability (typically above 10 mV/V) and was interpreted as bedrock gneiss. Higher resistivity values are expected for gneiss due to the low degree of alteration and low porosity. The larger chargeability values may be related to accessory metallic minerals in the gneiss, which have not yet been processed by weathering conditions.

To illustrate these results, Figure 6 and Table 4 summarize the geo-electrical model of VES 10 with the succession of layers of soil above the bedrock gneiss.

In the data concerning VESs 05, 06, 24, 27, and 28, resistivity values below 1000 ohm.m were observed for the last layer, which is interpreted as saprolite or weathered gneiss. These relatively low values suggest a rock with some degree of alteration and/or fracturing.

Figure 7 and Table 5 present the geo-electrical model for VES 05, in which the fourth layer is characterized as saprolite or weathered gneiss.

Another VES with results that clash with the other models is VES 19, where the resistivity of the layer above the layer interpreted as bedrock is relatively high (greater than 2000 ohm.m). Here it is possible that the third layer is characterized by a slightly weathered or fractured rock.

Table 4. VES 10 with a succession of soil layers on top of the bedrock.

Layer	r (ohm.m)	M (mV/V)	Thickness (m)	Top Depth	Interpretation
1	37.4	0.3	0.5	0.0	Top soil
2	2270.9	8.3	2.3	0.5	Unsaturated soil
3	96.5	4.2	2.5	2.9	Low saturated soil/saprolite
4	7633.5	29.6		5.4	Gneiss

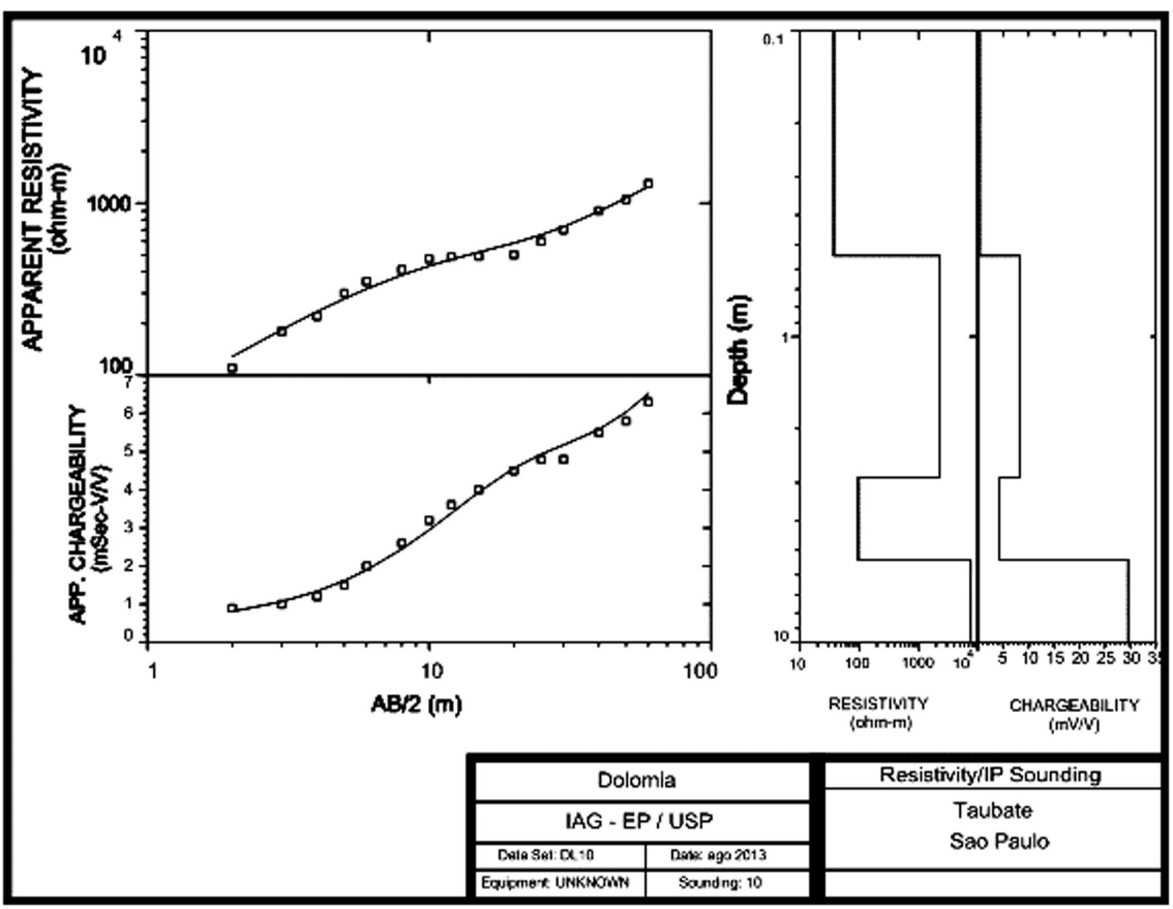

Figure 6. Geo-electrical model of VES 10.

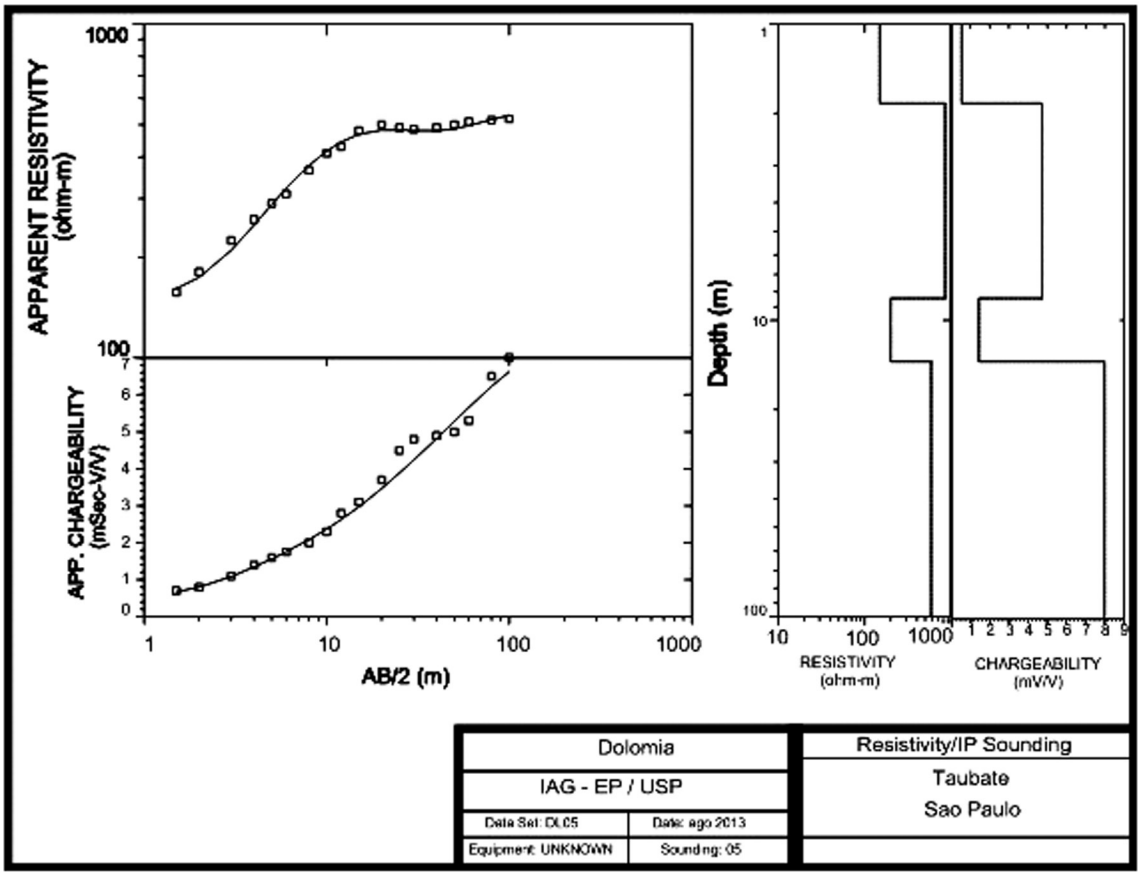

Figure 7 – Geo-electrical model of VES 05.

Table 5. VES 05, in which the fourth layer is characterized as saprolite or weathered gneiss.

Layer	r (ohm.m)	M (mV/V)	Thickness (m)	Top Depth	Interpretation
1	148.8	0.5	1.9	0	Top soil
2	851.6	4.7	6.6	1.9	Unsaturated soil
3	198.8	1.4	5.3	8.4	Low saturated saprolite/soil
4	585.9	8		13.8	Saprolite/weathered gneiss

Morphological Model Update

Table 6 shows the interpreted depth of the rock top, which was used for updating the morphological model.

The interpreted data of the top of the rock layer in all VESs conducted in the area of interest were used to update the morphological model of the area.

Figure 8 shows the geological sections across the updated morphological model. Figures 9 and 10 show the geological sections AA' and BB' with the original model and the expanded interpretation using data from VESs.

Table 6. Interpreted depth of the bedrock contact for updating the morphological model.

Point	Rock top depth (m)	Point	Rock top depth (m)
VES 01	18.20	VES 16	15.10
VES 02	11.80	VES 17	17.90
VES 03	26.10	VES 18	8.60
VES 04	8.60	VES 19	17.00
VES 05	13.80	VES 20	26.80
VES 06	21.00	VES 21	18.60
VES 07	26.30	VES 22	24.00
VES 08	34.50	VES 23	24.40
VES 09	28.50	VES 24	11.40
VES 10	5.40	VES 25	16.60
VES 11	7.20	VES 26	35.60
VES 12	7.20	VES 27	7.40
VES 13	38.40	VES 29	8.80
VES 14	16.00	VES 30	8.30
VES 15	13.20	VES 31	7.20

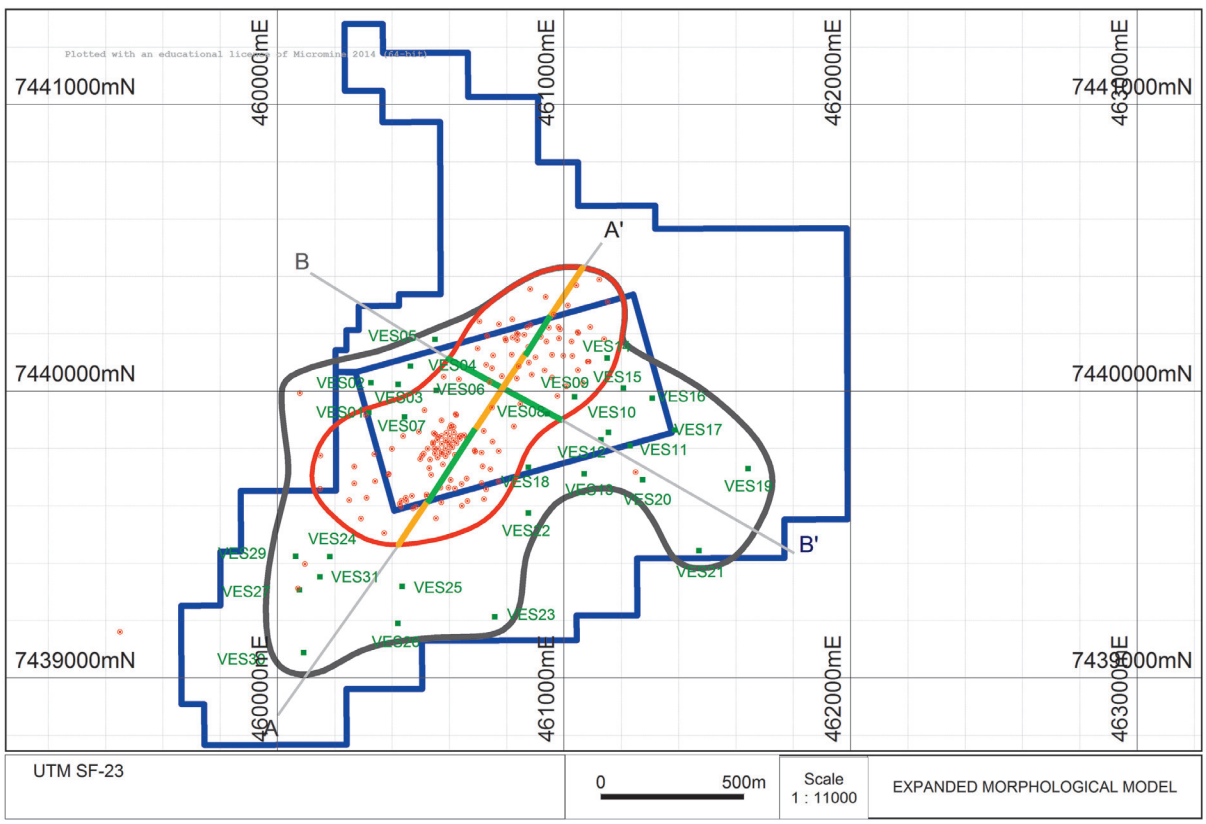

Figure 8. Position of the geological sections across the updated morphological model.

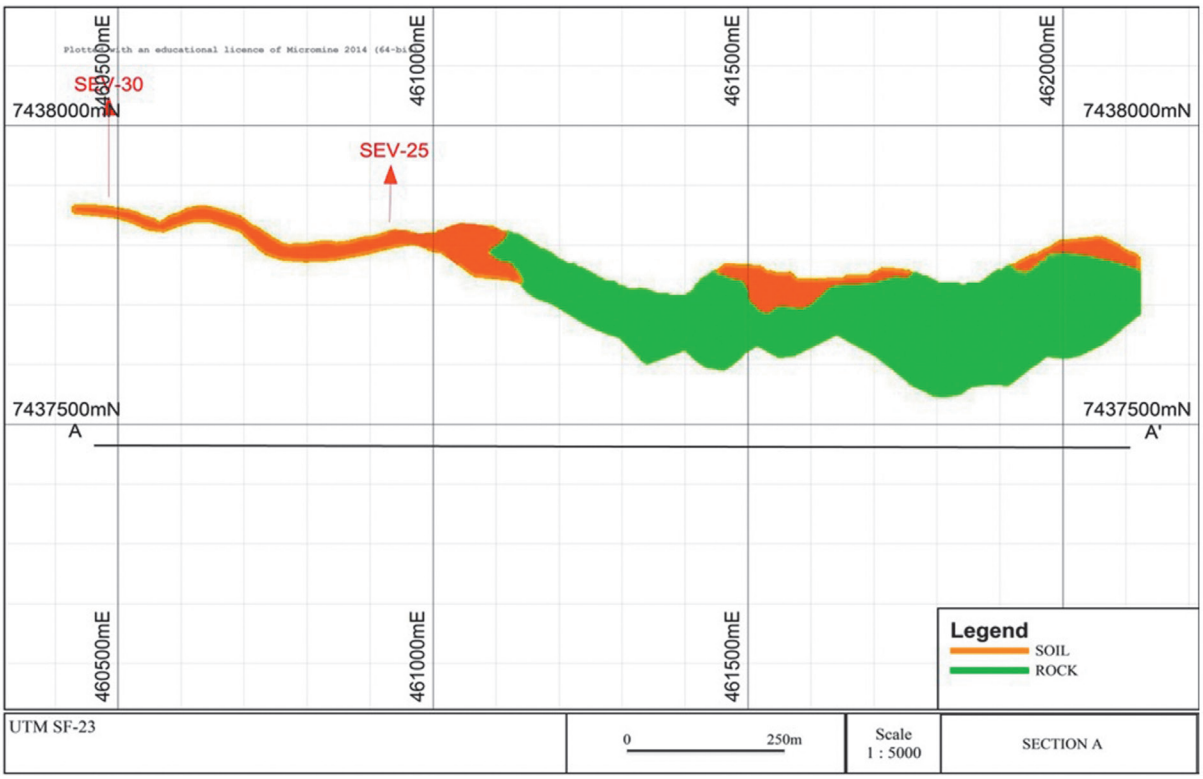

Figure 9. Geological section AA'.

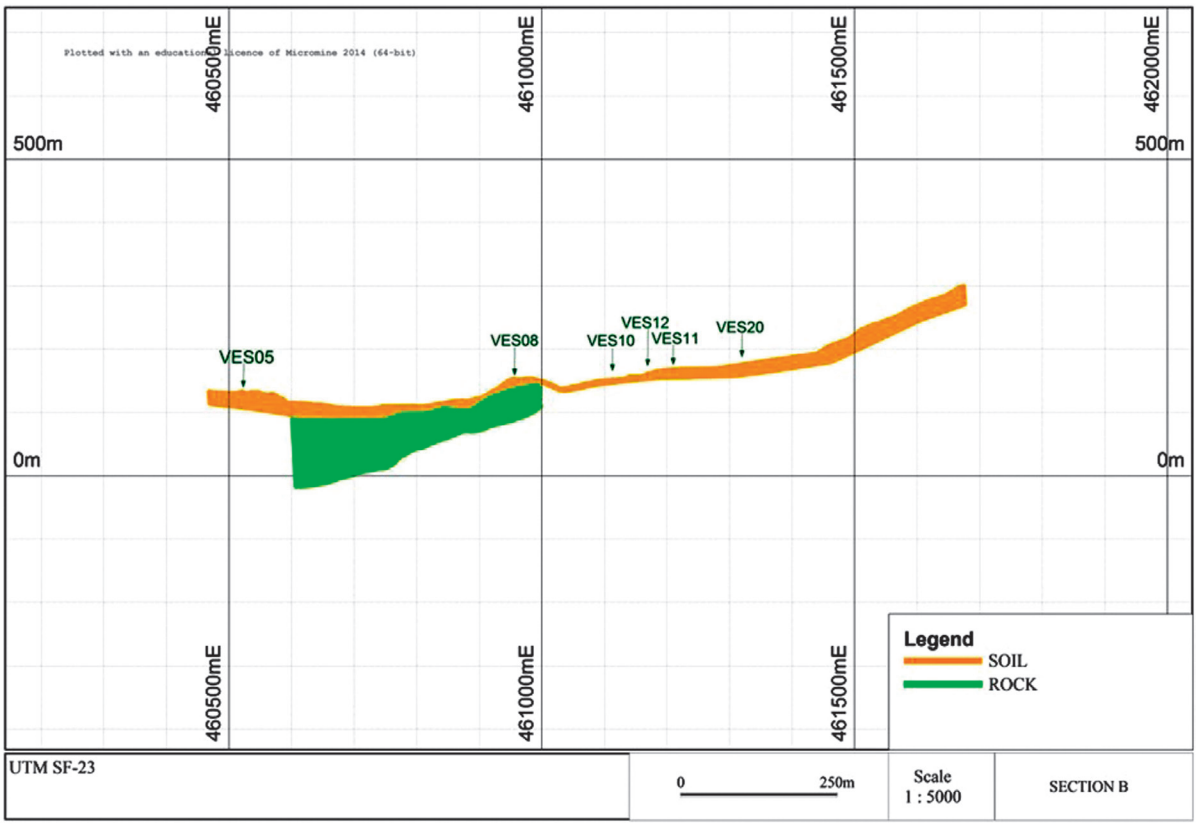

Figure 10. Geological section BB'.

Conclusion

The geophysical study carried out allowed the efficient expansion of the morphological model of the deposit within the exploration permit area, taking into account the aims established:

- to interpret, with adequate accuracy, the lithological units of interest (soil layer depth and the contact between soil and bedrock)

- to carry out the exploration campaign in the entire area of interest within the deadlines set by the company.

The study results show that the geophysical methods proposed in this paper can be used to determine the thickness of the soil layer on the top of the bedrock and to identify the layers of interest. That is, this research has proved that geophysics can improve the level of geological knowledge for morphological modeling purposes and its application has the potential to be extended and increased within the associated activities in the mine planning cycle of a mining operation.

In practical terms, the introduction of the proposed geophysical methods and techniques allowed the gathering of information necessary for updating the morphological model, which would normally have been carried out in approximately 60 days (using between three and four drilling equipment), in 15 days, which means a 70% reduction in the work time.

It is suggested that some drill holes are carried out right next to the VESs that showed low resistivity of the gneiss to validate the interpretation of this particular lithology.

It is likely that some differences in position between the interfaces defined by geophysics and the drill holes should occur. This can be explained by the limitations of the methods and geophysical techniques in the identification of contact within highly irregular topography.

Acknowledgements

The authors are grateful for the support provided by to FAPESP (Foundation for Support to the Research of the State of São Paulo, Brazil), CNPq (National Counsel of Technological and Scientific Development, Brazil) and Micromine Pty Ltd. (Australia).

References

Atzemoglou A., Tsourlos P., Pavlides S., 2003, Investigation of the tectonic structure of the NW part of the Amynteon Basin (NW Greece) by means of a Vertical Electrical Sounding (VES) survey. *J. Balkan Geophys. Soc.,* 6, 4, 188–201.

Bery A.A., Saad A. 2012, Tropical clayey sand soil's behaviour analysis and its empirical correlations via geophysics electrical resistivity method and engineering soil characterizations. *International J. Geosci.,* 3, 111–116, Scientific Research.

Elis V.R., 1999, Avaliação da aplicabilidade de métodos elétricos de prospecção geofísica no estudo de áreas utilizadas para disposição de resíduos. Tese de Doutorado, Instituto de Geociências e Ciências Exatas, UNESP, Campus de Rio Claro-SP, 264 p.

Frasheri A., Lubonja L., Alikaj P., 1995, On the application of geophysics in the exploration for copper and chrome ores in Albania. *Geophys. Prospect.,* 43, 6, 743–757.

Haile T., Atsbaha S., 2014, Electrical resistivity tomography, VES and magnetic surveys for dam site characterization, Wukro, Northern Ethiopia*. J. African Earth Sci.,* 97, 67–77.

Ogilvy A.A., Bogoslovsky V.A., 1979, The possibilities of geophysical methods applied for investigating the impact of man on the geological medium. *Geophys. Prospect.,* 27, 4, 775–789.

Okay G., Cosenza P., Ghorbani A., Camerlynck C., Cabrera J., Florsch N., Revil A., 2013, Localization and characterization of cracks in clay rocks using frequency and time domain induced polarization. *Geophys. Prospect.,* 61, 1, 134–152.

Orellana E., 1972, Prospeccion Geoelectrica en Corriente Continua. Ed. Paraninfo, Madrid, 523 p.

Ravindran A.A., 2010, Characterization of the geology of subsurface shallow conglomerate using 2D electrical resistivity imaging at Baragadi, Panna District, Madhyapradesh, India. *J. Appl. Sci. Environ. Manag.,* 14, 3.

Sahbi H., Jongmans D., Charlier R., 1997, Theoretical study of slope effects in resistivity surveys and applications*. Geophys. Prospect.,* 45, 5, 795–808.

Sumner J.S., 1976, Principles of Induced Polarization for Geophysical Exploration. Elsevier Scientific Publishing Co., Amsterdam, 227 p.

Telford W.M., Geldart L.P., Sheriff R.E., 1990, Applied Geophysics. Cambridge University Press, Cambridge, 770 p.

Geofísica Internacional (2016) 55-4: 239-253

Original paper

Geoelectrical investigation of saline water intrusion into freshwater aquifers: A case study of Nador coastal aquifer, Tipaza, Algeria

Abdelkader Bouderbala*, Boualem Remini and Abdelamir Saaed Hamoudi

Received: August 11, 2015; accepted: August 08, 2016; published on line: October 01, 2016

DOI: 10.19155/geofint.2016.055.4.2

Resumen

El agua subterránea en el acuífero costero plio-cuaternario de Nador tuvo una alta salinidad en el año 1995, debido a la intrusión de agua de mar, ya que la conductividad eléctrica (CE) superó 9.000 µS.cm-$^{-1}$. Después de la construcción de la presa de Boukourdane, hubo una reducción del bombeo de las aguas subterráneas y se aseguró el riego desde la presa y con el agua resultante de la planta de tratamiento de aguas residuales.
El análisis físico-químico de la calidad del agua subterránea para el año 2013 muestra que hay una reducción de la salinidad en comparación con el año 1995, con valores de CE de menos de 4.400 µS.cm^{-1}. Esto indica también que más del 45% de los parámetros físico-químicos tienen valores por encima de los límites permisibles de la norma de la OMS para agua de consumo. El estudio geofísico está dirigido principalmente a la comprensión de las características geofísicas de las aguas subterráneas en Nador obtenido a partir de un estudio de la distribución de la resistividad eléctrica del subsuelo mediante la aplicación de las técnicas de sondeo eléctrico vertical (SEV) y tomografía de resistividad eléctrica (ERT). Un total de 47 SEV y 3 perfiles de ERT, se llevaron a cabo para entender la distribución de la resistividad de la zona. La interpretación de los resultados ha identificado un acuífero costero altamente salino y delinea el agua dulce río arriba a más de 2 kilómetros.

Palabras clave: acuífero costero, intrusión de agua salina, calidad del agua subterránea, métodos geoeléctricos, Argelia.

Abstract

The groundwater in Nador coastal plio-quaternary aquifer had high salinity in 1995, due to a seawater intrusion, where the Electrical Conductivity (EC) exceeded 9000 µS.cm^{-1}. After the implementation of Boukourdane's dam, a pumping reduction of groundwater occured, and the irrigation was ensured by the dam and the water resulting from the sewage treatment plant.
The physico-chemical analysis of the groundwater quality for the year 2013 shows that there is a dilution of the salinity compared to 1995 with values of EC less than 4400 µS.cm^{-1}. It also shows that more than 45% of the physico-chemical parameters have values above the permissible limits of the WHO standard for drinking purpose. The geophysical study is aimed mainly to understand the geophysical characteristics of groundwater in Nador plain by studying the electrical resistivity distribution of the subsurface saturated layers by applying the Vertical Electrical Sounding (VES) and Electrical Resistivity Tomography (ERT) techniques. A total of 47 VES and 3 profiles of ERT were carried out to understand the resistivity distribution of the area. The interpretation of the results has identified a highly saline coastal aquifer and delineates the freshwater in the upstream at more than 2 km.

Key words: coastal aquifer, saline water intrusion, groundwater quality, geoelectrical tools, Algeria.

A. Bouderbala*
Faculty of nature and earth sciences
University of Khemis Miliana
Ain Defla 44000, Algeria
*Corresponding author: bouderbala.aek@gmail.com

B. Remini
Department of Water Sciences
Blida University
Blida 9000, Algeria

A. Saaed Hamoudi
Department of Hydraulic
Chlef University
Chlef 2000, Algeria

Introduction

Algeria has a very long coastline of about 1200 km and 25% of the country's population live in the coastal zone. The high population density along the banks of coast increases the water necessity for the human activities. The coastal aquifers can be polluted by natural or anthropogenic pollution, such as marine intrusion, discharge of untreated wastewater and chemical weathering of natural geological deposits. The problem of seawater intrusion is one of the major threats to coastal area freshwater resources. Algeria has been identified as one of the countries where the problem has felt most severely (Bouderbala and Remini, 2014).

The plio-quaternary aquifer of Tipaza which is directly recharged from the infiltration of rainfall, was considered before 2000 the main source of groundwater in Tipaza province (Figure 1). The excessive pumping due to the rapid increase of water demand for agriculture and drinking purposes during the last two decades changed the balance between fresh water in the aquifer and saline water intruding from the Mediterranean Sea. On the other hand, drought conditions prevailed between 1985 and 2000, the groundwater pumped increased and the level of the water table decreased under sea level, reversing the groundwater flow. The piezometric levels indicate that groundwater reached its lowest level since 1995. Many wells dried and several farmers leaved their farmland. This severe decline in the groundwater levels is naturally associated with a significant deterioration of groundwater quality. The seawater migrated into the aquifer causing a considerable increase in the groundwater salinity, where the wells and drillings have registered high values of electrical conductivity exceeding 9000 $\mu S.cm^{-1}$ (in dry period 1995). In front of these situations, the majority of these hydraulic structures were abandoned in this sector, and the water demand has been ensured by Boukourdane's dam (Bouderbala, 2015; Bouderbala *et al*., 2016). Geophysical techniques combined with hydrochemical methods have been recognized as the most efficient tools to investigate the saline water intrusion. Geophysical methods are used essentially for the quantitative and qualitative assessment of groundwater resources. It has been successfully used to demarcate the saltwater–freshwater interface in different coastal settings around the world (Nowroozi *et al*., 1999; Abu-Zeid *et al*., 2004; Sherif *et al*., 2006; Bouderbala and Remini, 2014). The chemistry of groundwater is largely a function of the mineral composition of the aquifer through which it flows. The hydrochemical processes and hydrogeochemistry of the groundwater vary spatially and temporally, depending on the geology and chemical characteristics of the aquifer (Pulido-Leboeuf, 2004).

The present study illustrates the applications of geo-electrical techniques along with major ion chemistry of groundwater to assess the saline water intrusion and to determine the present status of groundwater quality in the Nador plain.

Study area

The Nador Plain, also called Nador Valley, is part of a large hill range known as the Sahel of Algiers. It is located approximately 75 km west of Algiers. The study covers an area of 19 km². It is bounded on the north by the Mediterranean Sea; in the south and east by the slopes of the Sahel; and in the west by the Chenoua Massif (Figure 1). It lies between latitudes 36° 33′, 36° 36′ and longitudes 2° 21′, 2° 27′. This valley follows a syncline oriented NE-SW, whose main axis is occupied by the Wadi Nador, which gives the study area its name. The plain is characterized by a slope generally varying from 0 to 1%, while the hillslope and piedmont on the right part of the plain (the slopes of Sahel) and the left side of the plain (Chenoua massif) have slopes of 1 to 10%. The population of Tipaza and neighboring cities has reached more than 45000, with a yearly growth rate of 2.5%.

Geology and hydrogeology

The geological formations that outcrop in the study area are Pliocene and Quaternary terrains (Figure 1).

-The pliocene is constituted by clay and marl of middle Pliocene age, surmounted by limestone and sandstone of upper pliocene age, which forms the most important aquifer in this area. The clay and marl of middle pliocene form the substratum of the aquifer.

-The quaternary formations are visible in the centre of the plain, with a thickness that can reach 30 m. They rest in discordance on the upper pliocene layers and are formed by sands, clay, and gravel and conglomerate. These deposits have an important hydraulic conductivity of interstices (about 10^{-3} $m.s^{-1}$) and a transmissivity of about 10^{-2} $m^2.s^{-1}$. They are surmounted by a layer of clay and silts in surface.

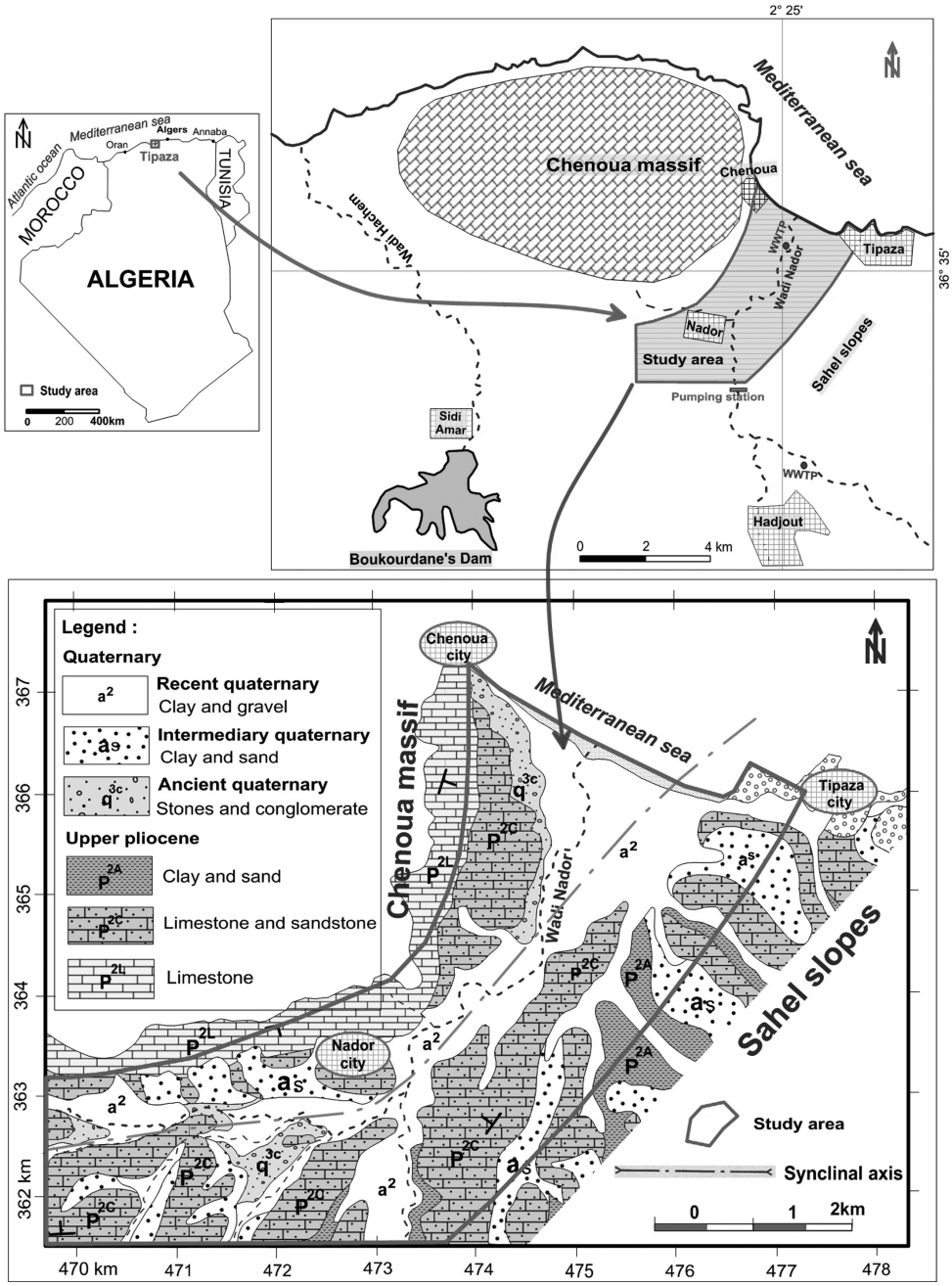

Figure 1. Geographic and geologic location of the studied area.

The Plio–Quaternary aquifer of Nador is formed by the Quaternary alluvium (sand, gravel and conglomerate), as well as sandstone and limestone of Upper Pliocene. In the centre of plain, the aquifer is confined under the impermeable layer of Quaternary (clay and sandy silt), while the aquifer in the two parts of the plain is unconfined. The aquifer's Quaternary and Pliocene horizons are in hydraulic communication. The substratum is formed mainly by marl of Middle Pliocene age.

The recharge to this Plio–Quaternary aquifer comes from the rainfall infiltration on the outcrops of the plain. The recharge also occurs by return flow of the irrigation water. The recharge of the aquifer by wadi Nador is very low because the flow is temporary, and the shores of the watercourses are clogged with clay.

The geological sections show that the thickness of the aquifer increases regularly

from upstream to downstream, reaching a maximum depth in the centre of the plaine of about 80m. However, the axis of the syncline coincides with the flow trajectory of wadi Nador. This indicates the continuity of the aquifer towards the sea. So there is a direct contact between the aquifer and the marine waters.

The hydrodynamic characteristics of the aquifer have been derived from bibliographic data pumping tests. Seven pumping tests carried out in the Nador plain show that values of hydraulic conductivity and transmissivity varied from 0.43 x 10^{-4} $m.s^{-1}$ to 6.83 x 10^{-4} $m.s^{-1}$ and from 5.28 x 10^{-3} $m^2.s^{-1}$ to 2.01 x 10^{-2} $m^2.s^{-1}$, respectively, from the upstream to the downstream. This variation in values of the hydrodynamic parameters is due to the increased thickness of the aquifer, the structure of the aquifer and the inhomogeneity of layers constituting the reservoir.

Materials and Methodology

Hydrochemical methods

For the assessment of groundwater quality, 18 groundwater samples were collected in the dry and wet periods in 2013. Samples were analyzed for major and minor ions (Ca^{2+}, Mg^{2+}, Na^+, K^+, Cl^-, SO_4^{2-}, HCO_3^-, NO_3^- and for physical parameters (pH, EC and temperature). Samples from all wells were collected in 500 mL polyethylene bottles, following the standard guidelines (Schoenleber, 2005). The samples were analyzed immediately for hydrogen ion concentration (pH), temperature (T °C) and electrical conductivity (EC). Other parameters were later analyzed in the laboratory of the National Agency of Hydraulic Resources. Concentration of calcium, magnesium, sodium, potassium, bicarbonate, chloride, sulphate, and nitrate were determined by standard procedures (APHA, 2005). Major ions like chlorides and bicarbonates were analyzed using volumetric methods. Calcium, magnesium, sodium and potassium were analyzed using atomic absorption spectrometry. Nitrates were measured by a colorimetric method. Sulphates were estimated by the UV–visible spectrophotometer. All concentrations are expressed in milligrams per liter ($mg.L^{-1}$), except pH and EC. The EC is expressed in microsiemens per centimeter ($\mu S.cm^{-1}$) at 25 °C. The reliability of all the obtained results was checked using the ionic balance of water.

Results indicate percentages ranging from -5 to + 5%, which corresponds to an acceptable reliability for the unit of the chemical results. The analysis of depths of the wells used in the study area revealed that all the measurement points are in the same hydrogeological context, with depths ranging from 8 m to 40 m, all capturing water from the Plio-quaternary aquifer. A pumping time of at least 30 min was required before the sample was collected. The pumps are usually installed near the bottom of the wells.

For this study, the analysis of samples in the wet period 2013 are also compared to these of the wet period 1995 to show the effect of irrigation by reuse water and pumping reduction in the groundwater quality.

Geophysical methods

The electrical geophysical prospecting method consists to determine the distribution of a physical parameter that is characteristic of the subsoil (the resistivity) on the basis of a very large number of measurements of apparent resistivity made from the ground surface (Store *et al*., 2000). The electrical resistivity of a geological formation is a physical characteristic that determines the flow of electric current in the formation. Resistivity varies with texture of the rock, nature of mineralization and conductivity of electrolyte contained within the rock (Kouzana *et al*., 2010). Resistivity not only changes from formation to formation but even within a particular formation (Sharma, 1997). Resistivity increases with grain size and tends to maximum when the grains are coarse, also when the rock is fine grained and compact. The resistivity drastically reduces with the increase in clay content which is commonly dispersed throughout as coatings on grains or disseminated masses or as thin layers or lenses. In saturated rocks low resistivity can be due to increased clay content or salinity. Hence the resistivity surveys are the best suited for delineation of clay or saline zone (Kirsh, 2009).

The subject of this geophysical investigation is to complete our previous study by Vertical Electrical Sonding (VES), through execution of Electrical Resistivity Tomography (ERT) profiles. The apparent resistivity measurements were conducted using a SYSCAL R1, IRIS instrument.

Vertical electrical sounding (VES)

VES is used to determine the resistivity variation with depth. It was applied in the ground assumed to be horizontal layered or with very little lateral variation. It's typically carried out in Schlumberger array, where the potential electrodes (M and N) are placed in a fixed position with a short separation and the current electrodes (A and B) are placed symmetrically

on the outer sides of the potential electrodes. After each resistivity measurement the current electrodes are moved further away from the centre of the array. In this way the current is stepwise made to flow through deeper and deeper parts of the ground. For large distances between the current electrodes, the distance of the potential electrodes is increased to ensure that the measured voltage is above the noise level and the lower detection level of the instrument (Telford *et al*., 1990).

The VES curves were interpreted using the available software program (WinSEV 6.0, 1D) and unacceptable errors in the apparent resistivity curves were removed during processing. The interpretation results were based as possible using all available drilling information through the surveyed area. A total number of 47 vertical electrical soundings were carried out in the survey area along 11 profiles (Figure 2). The Schlumberger array was applied with half current electrode spacing (AB/2) starting from 2 m to 800 m. In VES, the theoretical investigation depth is about AB/5 (Kirsch, 2009).This spacing is sufficient to reach adequate depths covering the plio-quaternary aquifer in the study area (Bouderbala and Remini, 2014).

The transverse resistance is also used in this study, it is defined as the product of the true resistivity and thickness of the aquifer (TR = thickness * resistivity of layer). This parameter is often identified as a good estimate of the transmissivity value of the aquifer matrix (saturated zone). The use of TR parameter for the saturated zones can help to delineate the influenced sector by seawater and to view the most favorable zones of good intrinsic hydraulic conductivity.

Electrical resistivity tomography (ERT)

ERT is an advanced geophysical technique used to imaging sub-surface structures from electrical resistivity measurements made at the surface. ERT profiles consist of a modeled cross-sectional (2-D) plot of resistivity (Ω·m) versus depth. After the reception of the pseudo-section of measured apparent resistivity, it is converted into true resistivity using RES2DINV inversion program in order to produce the 2D resistivity cross-section image (Dahlin, 1996).

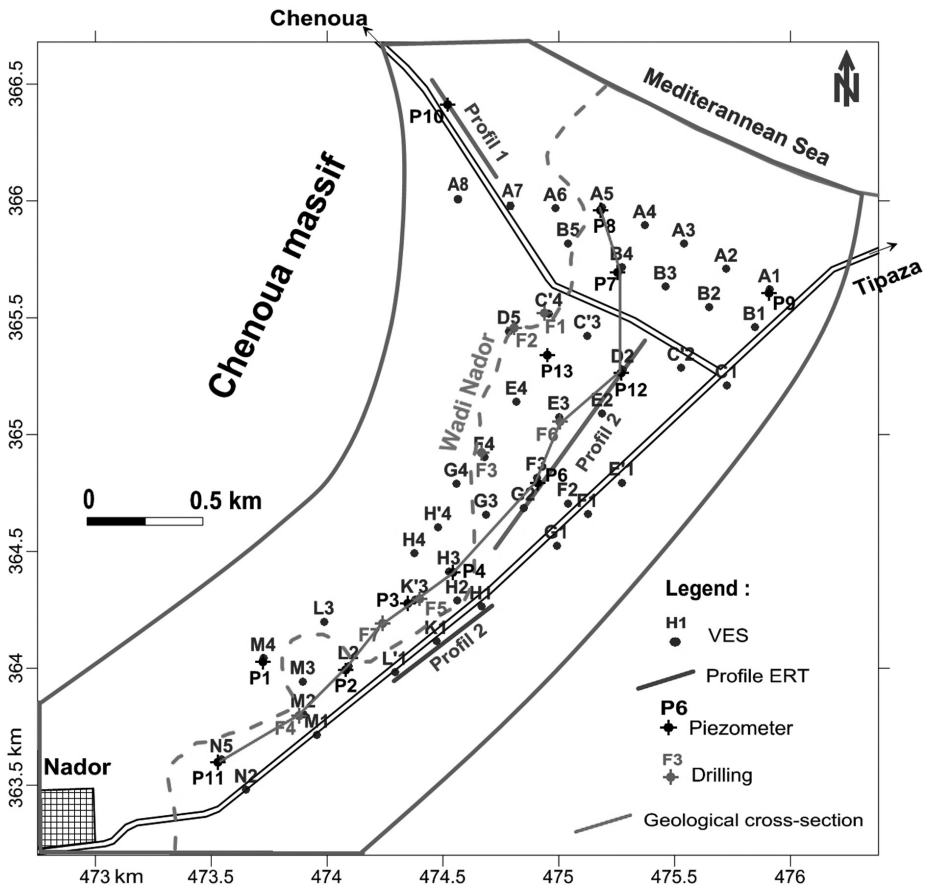

Figure 2. Situation of VES and ERT profiles in the study area.

The output from the RES2DINV displays three sections, i.e., measured and calculated apparent resistivity pseudo-sections and the inverse model resistivity section. The pseudo-sections are a qualitative way of presenting spatial variation of the measured or calculated apparent resistivity along cross-section and do not reflect the true depth and true formation resistivity (Dahlin, 1996).

In the present study, the geophysical investigation using ERT profiles has been carried out at 3 locations in the area (Figure 2). The locations of these profiles were chosen in three different places (upstream, centre and downstream of the plain) and based also on the available monitoring wells for calibration purposes. Wenner-Schlumberger array with 20 m electrode spacing was used to collect resistivity data, in order to reach an investigation depth of about 100 m.

Correlation of the VES and ERT results with geological information

The geoelectric resistivity of sediments is one of the most variable physical properties, especially in a very complicated sedimentlogical environment that dominates alluvial areas. Therefore, the ambiguities in interpretation may occur and it becomes very necessary to correlate the mesured VES data with the available drillings data (Gununagha Rao *et al*., 2011). This enables us to assign the geoelectric units to the corresponding lithologic units (a correlation must be found between the resistivities of layers inverted from the VES data with the geology of drillings) and consequently put a reliable control on the interpretation of the subsurface sequence in the study area. Data from seven drillings were analyzed and used to correlate the results of the VES geoelectrical surveys and to determine the electrical characteristics of the rock units with depth.

Results and Discussion

Piezometric map

The studied aquifer is characterized by a thick reservoir of relatively high hydraulic conductivity and transmissivity, as well as a substratum that dips below sea level (approximately -80 m). This indicates a direct contact between the Plio–Quaternary aquifer of freshwater and the saltwater wedge, as illustrated in Figure 3. This poses an important vulnerability with respect to the marine water entries towards the aquifer (Bouderbala *et al*., 2014).

The analysis of the piezometric map related to the wet period (April 2012), allowed the characterization of the flow directions of the water table and the evolution of the hydraulic gradient of the aquifer (Figure 4). The map shows that the lines of groundwater flows converge towards the axis of the synclinal, which constitutes the principal drainage axis of the Plio–Quaternary aquifer. This map also indicates the existence of the piezometric water level '0 m' inside the plain. A reverse flow

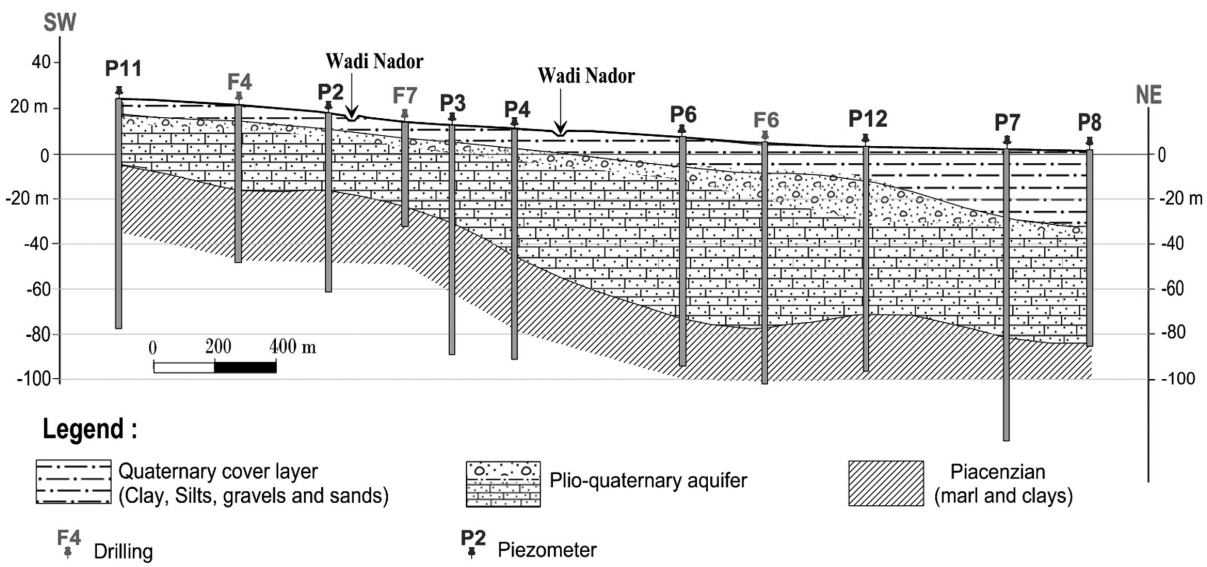

Figure 3. Geological cross-section parallel to the synclinal axis.

direction of the groundwater is observed. This change of direction is related to groundwater overexploitation from pumping near the sea, which generates an important mixture between marine water and groundwater. These mixtures are a consequence of groundwater salinization, in which the degree depends on the effective precipitation rate and pumping.

Geophysical study

Electrical resistivity of the soil can be considered as a proxy for the spatial and temporal variability of many other soil physical properties (i.e. structure, water content, or fluid composition). Because the method is non-destructive and very sensitive, it offers a very attractive tool for describing the subsurface properties without digging (Sarwade *et al*., 2007). Seventeen VES were done near to seven drillings and ten piezometers. It is relevant to note that, at present, all the piezometers in the study area are clogged and have been abandoned; only three of the drinking water supply drillings remain operational, namely F3, F5, and F7. Examination of SEV models realized close to drillings and piezometers, which defined resistivities and thicknesses of the layers, permitted to determine the scale of resistivities for our electrical prospection, as shown in Figures 5a, 5b and 5c. (Bouderbala and Remini, 2014):

- Quaternary cover layer: between 5 and 25 Ωm;

- Plio-Quaternary aquifer with brackish water: between 6 and 36 Ωm;

- Plio-Quaternary aquifer with fresh water: between 30 and 50 Ωm;

- Plaisancian marly clays substratum: between 5 and 10 Ωm.

Vertical electrical sounding

The interpretation of the apparent resistivity values of VES has indicated three subsurface layers. A surface layer consisting of quaternary cover (silt, clay sand and gravel), a second layer consisting by plio-quaternary aquifer (stones and conglomerate of ancient quaternary, sand and limestone and sandstone of upper pliocene). The aquifer indicates a direct contact with sea, the thickness of the aquifer increases regularly from upstream to downstream. The bedrock (substratum) as a third layer consists of marls plaisancian (Bouderbala and Remini, 2014). The examination of 11 transverse geoelectric profiles together shows that the aquifer traces a syncline in a SW-NE orientation, whereby the sections also indicate dips down from the eastern and western borders towards the axis of the syncline. This

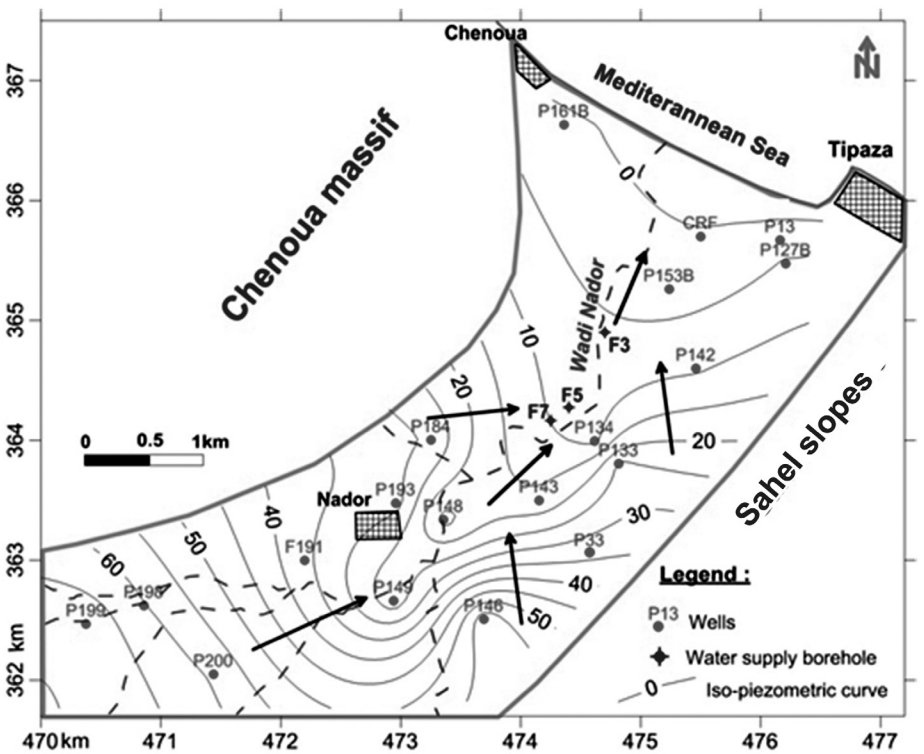

Figure 4. Piezometric map of Nador aquifer (April 2012).

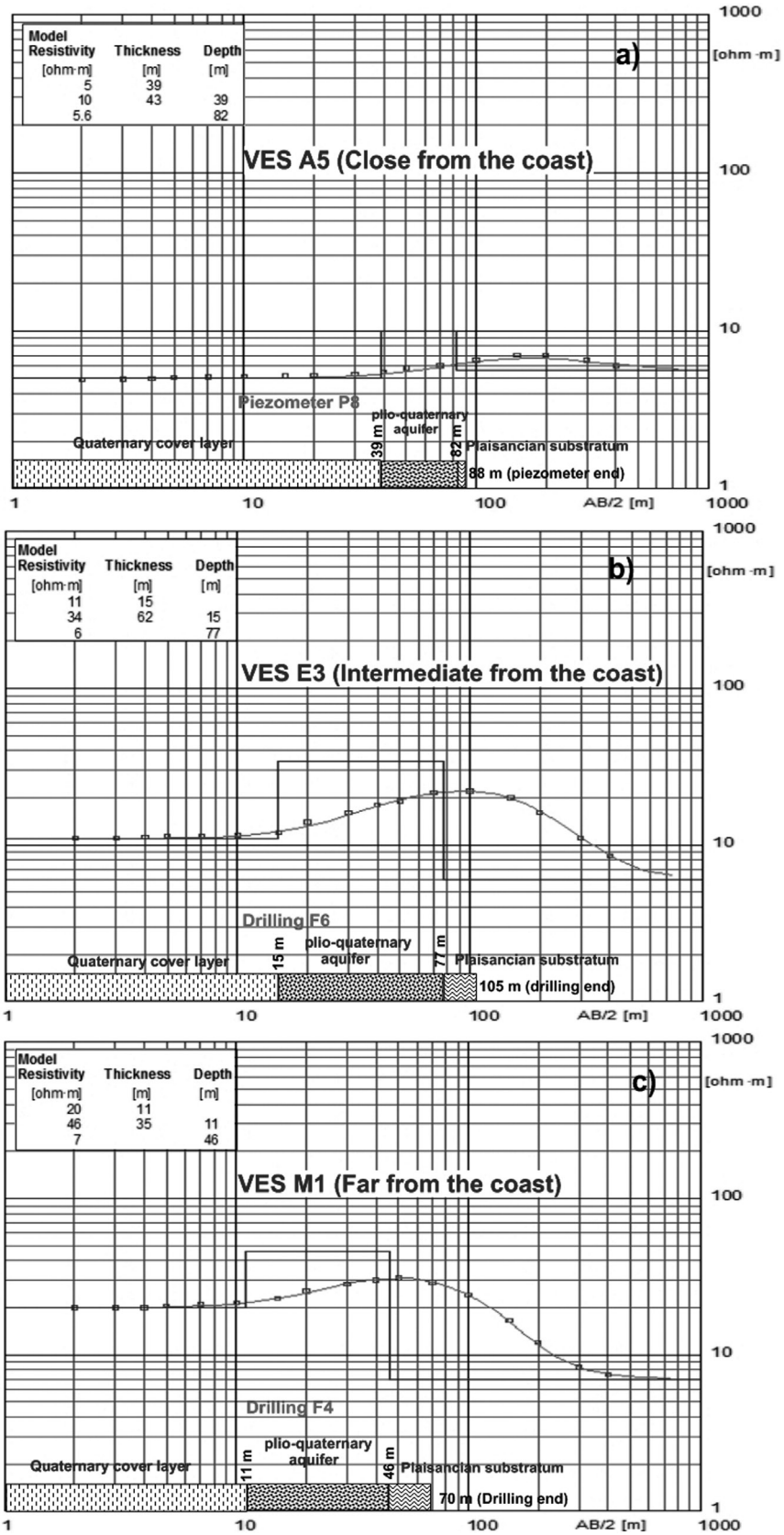

Figure 5. Examples of VES models realized near to drilling and piezometer a) Close from the coast, b) intermediate from the coast, c) far from the coast.

aquifer's layers reach its maximum thickness of 60 m at the points VES D5 and E3. The cross sections also show how the Plio-Quaternary aquifer is overlaid by a variable layer (up to 30 m thick) of clayey sediments. Except where the aquifer formations outcrop on the east and western boundaries, these clays locally confine the aquifer.

The transverse resistance (TR) map of the Plio-quaternary aquifer (Figure 6) shows that the values of TR vary from 1800 to 600 Ohm.m² near the coast. The low values of TR near the coast are probably related to marine intrusion processes. However, the low values of RT in the upstream of the plain are related to the low thickness.

In the central sector, the values of transverse resistance are the highest of the plio-quaternary aquifer, where the thickness is more than 40 m, the resistivity is about 40 and 45 Ω.m . This sector is characterized also by good interstitial and fissure hydraulic conductivity, which can reach 6.83×10^{-4} m.s^{-1}. On the basis of this map, it is possible to delineate the extension of saltwater into the aquifer, it is about 2 km inland, near the F profile.

Electrical resistivity tomography (ERT)

In the present study area geophysical investigations using ERT surveys have been carried out at 3 locations in the Nador plain. Wenner-Schlumberger array with 20m electrode spacing was used to collect resistivity data which provides adequate resolution of sub-surface. The depth of investigation is 50 m for profile 1,100 m for profile 2 and about 80 m for profile 3. The ERT profiles showed resistivity values that varied laterally and at depth (Figure 7).

The profile P1 (oriented NW-SE) was located in the coastal sector (500 m from the shore). It shows two distinct levels of resistivity, the upper layer with resistivity >15 Ωm until a depth of 25m, due to the existence of a quaternary alluvial formation (clay and gravel), while the low resistivity of < 5 Ωm, for a depth lower than 25m, is due to the saturated plio-quaternary aquifer with saline water.

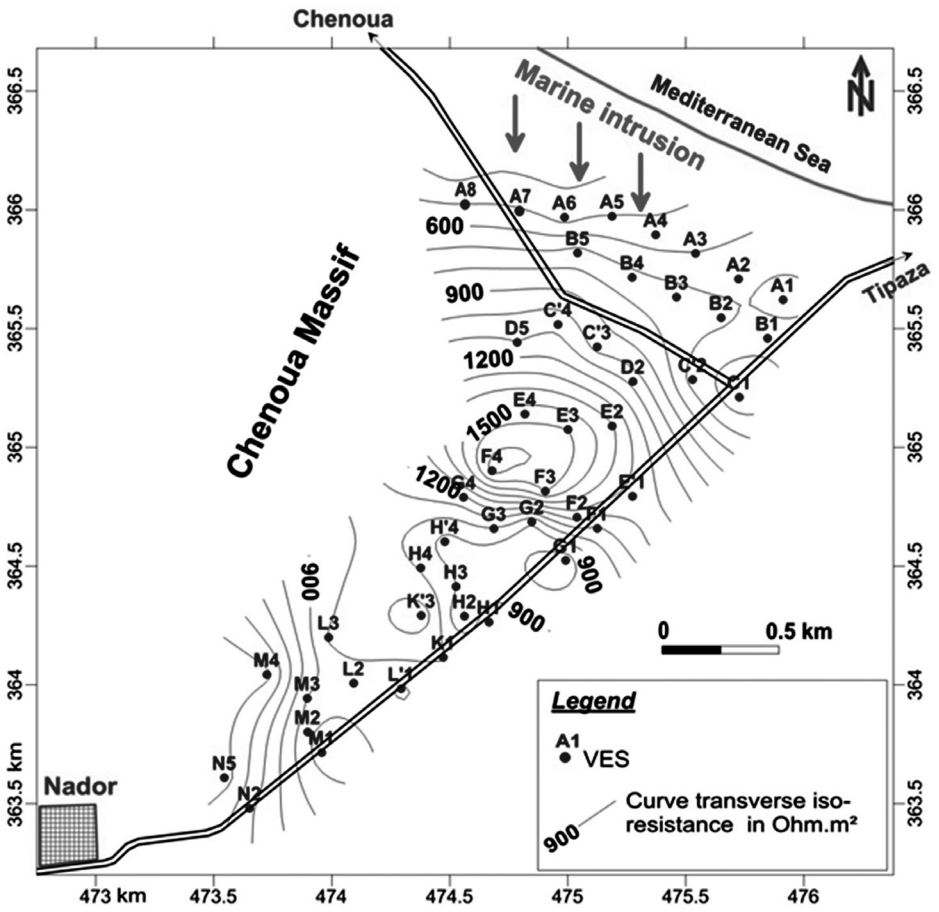

Figure 6. Transverse resistance map of the Nador plio-quaternary aquifer.

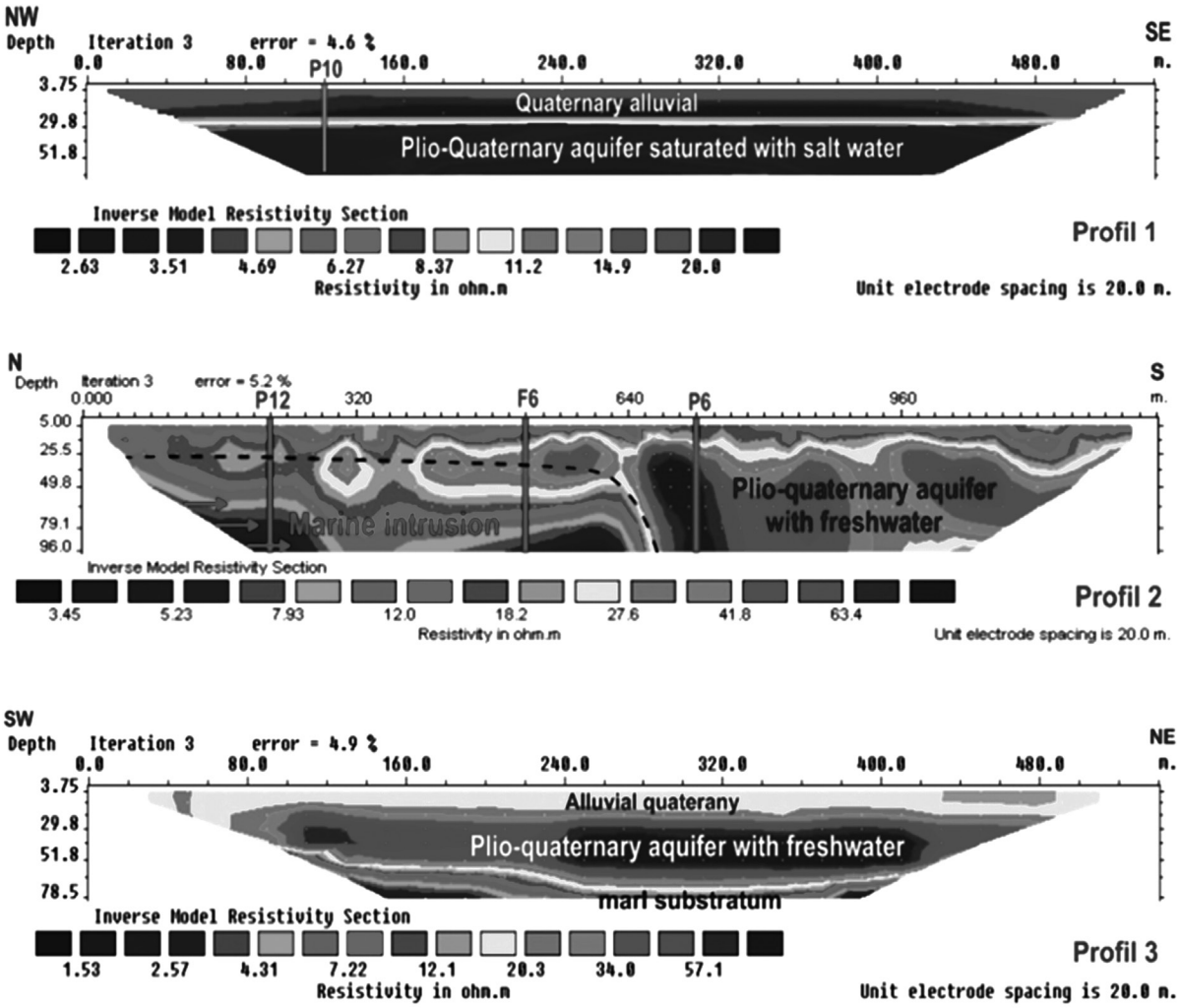

Figure 7. Geo-electrical resistivity profiles in the study area.

The profile P2 (orientated N-S), 1200m long, has been located in the center of the plain, perpendicular to the shore. The aquifer geometry and the extension of the salt wedge were ascertained from the electrical resistivity profile. It shows an upper layer of alluvial deposits with low resistivity of <20 Ωm, while at 25m depth in the north of the profile, the low resistivity value observed at depth between 50 to 100m is due to saline water after the overexploitation of groundwater accompanied to the low recharge rate.

Profile 3, was carried out upstream of the plain, 500 m long in the NE-SW direction. The layer in surface of quaternary alluvial exhibits moderate resistivity; between 10 and 12 Ωm, probably due to the presence of consolidated material mostly with silt and clay. Further, the profile shows, the freshwater saturated aquifer below the top layer with resistivity ranging between 35 and 60 Ω.m. The variability of the values is due to the heterogeneity of the aquifer. It shows also the presence of marl substratum of middle pliocene in the base with resistivity lower than 7 Ω.m.

Hydrochemical study

The results of physico-chemical analyses during the wet periods of 1995 and 2013 are given in Tables 1 and 2. The results show that water is characterized by an electrical conductivity being ranged between 1520 $\mu S.cm^{-1}$ and 8950 $\mu S.cm^{-1}$ for wet water 1995, and between 1360 $\mu S.cm^{-1}$ and 4400 $\mu S.cm^{-1}$ for wet water period 2013. The pH values are more than 7.0 in the two periods which indicates that the Nador groundwater is slightly alkaline in nature.

Table 1. Physicochemical analysis of groundwater in the Nador plain, April 1995 (wet period).

N° of well	CE $\mu S.cm^{-1}$	TDS $mg.L^{-1}$	pH $mg.L^{-1}$	NO_3^- $mg.L^{-1}$	HCO_3^- $mg.L^{-1}$	SO_4^{-2} $mg.L^{-1}$	Cl^- $mg.L^{-1}$	Na^+ $mg.L^{-1}$	Mg^{+2} $mg.L^{-1}$	Ca^{+2} $mg.L^{-1}$	K^+
P199	1 572	1 055	7.7	5	495	195	236	205	28	175	0
P200	2 560	1 740	7.4	25	542	154	585	325	52	213	0
P198	2 700	1 785	7.3	4	535	148	584	314	45	199	0
F191	1 520	1 016	7.6	55	325	81	295	135	37	149	6
P149	2 035	1 398	7.8	85	570	182	234	114	42	216	0
P184	2 070	1 390	7.1	8	415	195	390	186	55	162	4
P193	2 100	1 415	7.3	30	654	203	285	150	57	215	0
P143	2 080	1 435	7.8	35	420	224	300	169	45	176	0
P146	1 965	1 350	7.5	39	605	175	430	208	105	224	2
P134	1 820	1 210	7.3	65	465	182	225	140	35	205	0
P33	1 490	980	6.5	55	385	150	188	115	30	175	0
CRF	8 150	5 405	7.8	78	507	594	3 155	2 408	160	85	7
P133	2 425	1 620	7.4	45	435	220	467	275	49	165	0
P142	2 375	1 595	7.6	85	545	140	342	245	30	165	4
127B	4 735	3 185	7.7	65	385	420	1 585	1 135	151	90	2
P13	5 575	3 755	7.6	72	455	507	1 875	1 345	188	102	4
P153	7 710	5 145	7.7	38	472	558	2 725	2 005	180	95	8
P161	8 950	5 962	7.8	50	482	580	3 335	2 565	142	67	12

Table 2. Physicochemical analysis of groundwater in the Nador plain, April 2013 (wet period).

N° of well	CE $\mu S.cm^{-1}$	TDS $mg.L^{-1}$	pH $mg.L^{-1}$	NO_3^- $mg.L^{-1}$	HCO_3^- $mg.L^{-1}$	SO_4^{-2} $mg.L^{-1}$	Cl^- $mg.L^{-1}$	Na^+ $mg.L^{-1}$	Mg^{+2} $mg.L^{-1}$	Ca^{+2} $mg.L^{-1}$	K^+
P199	1418	975	7.2	18	380	116	156	85	29	158	0
P200	1661	1095	7.1	45	325	151	236	149	41	146	3.91
P198	1505	1030	7.3	15	386	153	205	123	37	164	3.91
F191	1590	1070	7.65	4	391	122	238	141	31	168	0
P149	1360	940	7.1	15	333	130	166	100	29	153	0
P184	1550	1060	7.6	40	420	124	228	150	43	158	3.91
P193	1455	995	7.8	35	410	113	218	134	45	152	0
P143	1368	890	7.6	75	390	102	176	95	44	157	3.91
P146	1625	1080	7.15	30	385	118	219	115	46	142	3.91
P134	1545	1020	7.65	70	355	441	270	135	135	164	3.91
P33	1435	985	7.55	24	288	320	270	131	45	167	0
CRF	1755	1145	7.6	16	352	391	225	124	99	175	3.91
P133	2025	1395	7.35	15	395	495	630	310	171	158	3.91
P142	3880	2610	7.2	50	392	1005	1600	1025	232	128	3.91
127B	3645	2452	7.3	28	460	935	1425	848	238	194	3.91
P13	2505	1655	7.9	35	398	636	892	552	192	130	3.91
P153	2915	1935	7.1	42	335	770	1120	645	208	164	3.91
P161	4400	2885	7.1	72	469	1080	2001	1288	284	168	7.82

The groundwater samples in this area of the years 1995 and 2013 were plotted on the graphs as cations versus anions expressed in milliequivalent percentage on the modified form of tri-linear diagram of Piper proposed by Chadha (1999). Eight water types that can be identified from the diagram depend on the relationship between alkaline earths (calcium and magnesium), alkali metals (sodium and potassium), weak acidic anions (carbonate and bicarbonate) and strong acidic anions (chloride and sulphate).

In 1995 (Figure 8a), the majority of the samples (more than 83%) are plotted in the 7th field, representing the Cl-SO_4–Na–Mg type, where the sodium and chloride are the dominant on groundwater thus showing a probable marine intrusion in part of the coastal area and urban pollution in the upstream area, where (Na + K) > (Ca + Mg) and (Cl + SO_4) > (CO_3 + HCO_3), such a water type generally creates salinity problems. While the rest of samples (less than 17%) are plotted in the 6th field representing Ca–Mg–Cl–SO_4 type, where (Ca + Mg) > (Na + K) and (Cl + SO_4) > (CO_3 + HCO_3), this water type is generally characterized by permanent hardness.

In 2013, the majority of the samples (72%) are plotted in the 6th field, representing Ca–Mg–Cl–SO_4 type, where (Ca + Mg) > (Na + K) and (Cl + SO_4) > (CO_3 + HCO_3), this water type is generally characterized by permanent hardness. While the rest of samples (27%) are plotted in the 7th field, representing the

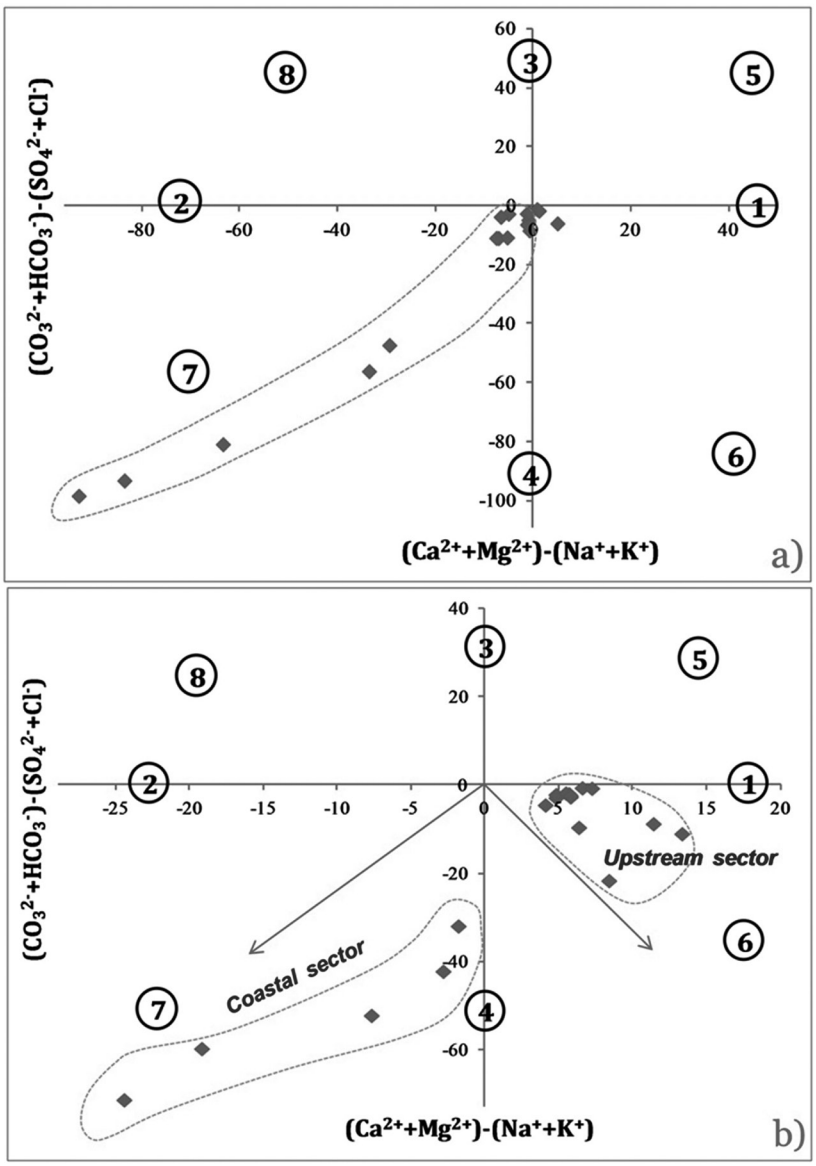

Figure 8. Chadha's diagram for groundwater of Nador plain a) in 1995 and b) in 2013.

Cl-SO_4–Na–Mg type, where the sodium and chloride are the dominant on groundwater thus showing a probable marine intrusion in this area, where (Na + K) > (Ca + Mg) and (Cl + SO_4) > (CO_3 + HCO_3), such a water type generally creates salinity problems. This indicate that the aquifer is essentially recharged by the excess of irrigation water coming from Boukourdane's dam and reuse water of wastewater treatment, and also due to the pumping reduction.

Electrical conductivity (EC)

Total ionised constituents of water denoted by EC greatly determine the quality of drinking water (Table 3). Groundwater had an average EC of 3435 µS.cm^{-1} in the year 1995 and had an average of 2090 µS.cm^{-1} in 2013. In 1995, only one groundwater sample (5.55%) with EC less than 1500 µS.cm^{-1} was permissible for drinking. Twelve groundwater samples were not-permissible for drinking, with EC range between 1500–3000 µS.cm^{-1} (66.67%) and five samples (27.78%) had EC higher than 3000 µS.cm^{-1}. Groundwater EC higher than 3000 µS.cm^{-1} depends on the weathering of the aquifer material, on the influence of anthropogenic activities polluting the ground surface and on a probable marine intrusion. While in 2013, after pumping reduction and the recharge by effective rainfall and by the excess of irrigation, five samples (27.28%) had EC less than 1500 µS.cm^{-1}, being permissible for drinking; ten samples (55.55%) were within the not-permissible for drinking with EC range of 1500–3000 µS.cm^{-1} and only three samples (16.67%) had EC higher than 3000 µS.cm^{-1}.

Total dissolved solids(TDS)

TDS is a measure of the combined content of all inorganic and organic substances contained in a liquid in molecular, ionized or micro-granular (colloidal sol) suspended form. In 1995, the TDS ranged from 980 to 5962 mg.L^{-1} in groundwater with a mean of 2302 mg.L^{-1}, and from 890 to 2885 mg.L^{-1} in 2013 with a mean of 1401 mg.L^{-1}. Classification of groundwater based on TDS is given in Table 4. Based on Davis and Dewiest (1966) classification, only one groundwater sample in 1995 was freshwater and five samples were freshwater in 2013, and the majority of samples were useful only for irrigation for the two years. High TDS may distort the taste of water and may cause gastrointestinal irritation in human beings (Howard and Bartram, 2003; Brindha and Kavitha, 2014).

Total hardness(TH)

TH depends on the calcium and magnesium content of water (Sawyer and McCarty, 1978) and is calculated as

$$TH\ (mg.L^{-1}) = 2.497\ Ca^{2+}\ (mg.L^{-1}) + 4.115\ Mg^{2+}\ (mg.L^{-1})$$

The totality of the groundwater samples in this area in 1995 and 2013 were very hard in nature (Table 5). Very hard waters may have adverse health effects like stone formation in kidney, calcification of arteries and other cardiovascular and stomach disorders. TH above 500 mg.L^{-1} (WHO, 2008) is not suitable for drinking.

Table 3. Classification of groundwater for drinking based on EC.

EC (µS.cm^{-1} at 25 °C)	Classification	1995		2013	
		Number of samples	% of samples	Number of samples	% of samples
< 750	Desirable	Nil	0	Nil	0
750 – 1500	Permissible	1	5.55	5	27.78
1500 – 3000	Not permissible	12	66.67	10	55.55
> 3000	Hazardous	5	27.78	3	16.67

Table 4. Classification of groundwater for drinking based on TDS (Davis and DeWiest, 1966).

TDS (mg.L^{-1})	Water type	1995		2013	
		Number of samples	% of samples	Number of samples	% of samples
< 500	Desirable for drinking	Nil	0	Nil	0
500 – 1000	Permissible for drinking	1	5.55	5	27.78
1000 – 3000	Useful for irrigation	12	66.67	10	72.22
> 3000	Unfit for drinking and irrigation	5	27.78	Nil	0

Table 5. Classification of groundwater for drinking based on TH (WHO 2008; Brindha and Kavitha, 2014).

TH ($mg.L^{-1}$)	Water type	1995		2013	
		Number of samples	% of samples	Number of samples	% of samples
< 75	Soft	Nil	0	Nil	0
75 – 150	Moderately high	Nil	0	Nil	0
150 – 300	Hard	Nil	0	Nil	0
300 – 500	Moderately hard	Nil	0	Nil	0
> 500	Very hard	18	100	18	100

Conclusion

Geophysical and hydrochemical analysis were carried out in the Nador plain, to delineate the area affected by the saline water and to identify the salinity origin in this aquifer. The hydrochemical study reveals that the groundwater in this coastal aquifer is slightly alkaline in nature. The sequence of the major cations and anions in the groundwater for the coastal sector was $Na^{+}>Mg^{2+}>Ca^{2+}>K^{+}$ and $Cl^{-}>SO_4^{2-}>HCO_3^{-}$ for 83% of the samples in 1995, and 28% in 2013. The alkali metal (Na) exceeds the alkaline earths (Mg^{2+} and Ca^{2+}) and strong acidic anions (Cl^{-} and SO_4^{2-}) exceed the weak acidic anion (HCO_3^{-}). The analysis of physico-chemical values suggest that the coastal samples fall under very poor quality classes and the groundwater in this sector is not suitable for drinking. It clearly indicates that this coastal sector is significantly affected by a seawater intrusion. Surface electrical resistivity surveys were carried out in this area, with the aim to delineate the salinity of groundwater and its subsurface configuration. The resistivity result revealed a decreasing for the aquifer layer in coastal sector which indicates increase of salinity with depth. The differences in resistivity are associated with the various lithology types and variations in water saturation. This allowed determining the extent of saltwater intrusion inland, approximately 1600 m into the Plio-Quaternary aquifer.

References

Abu-Zeid N., Bianchini G., Santarato G., Vaccaro C., 2004. Geochemical characterization and geophysical mapping of landfill leachates: the Marozzo canal case study (NE Italy). *Environ. Geol.,* 45, 4, 439–447.

APHA 2005. Standard methods for the examination of water and wastewater, 21st edn. American Public Health Association, Washington, DC.

Bouderbala A., Remini B., 2014. Geophysical Approach for Assessment of Seawater Intrusion in the Coastal Aquifer of Wadi Nador (Tipaza, Algeria). *Acta Geophys.,* 62, 6, 1352-1372. DOI: 10.2478/s11600-014-0220-y.

Bouderbala A., Remini B., Pulido-Bosch A., 2014. Hydrogeological characterization of the Nador Plio-Quaternary aquifer, Tipaza (Algeria), *Bol. Geol. Min.,* 125, 1, 77-89.

Bouderbala A., 2015., Groundwater salinization in semi-arid zones: an example from Nador plain (Tipaza, Algeria). *Environ. Earth Sci.*, 73, 9, 5479-5496.

Bouderbala A., Remini B., Hamoudi A.S., Pulido-Bosch A., 2016. Assessment of groundwater vulnerability and quality in coastal aquifers: a case study (Tipaza, North Algeria). *Arabian J. of Geosci.,* 9, 3, 1-12.

Brindha K., Kavitha R., 2014. Hydrochemical assessment of surface water and groundwater quality along Uyyakondan channel, south India. *Environ. Earth Sci.*, online. DOI 10.1007/s12665-014-3793-5.

Chadha D.K., 1999. A proposed new diagram for geochemical classification of natural waters and interpretation of chemical data. *Hydrogeol. J.,* 7, 431–439.

Dahlin T., 1996. 2D resistivity surveying for environmental and engineering applications. First Break, 14, 275–284.

Davis S.N., DeWiest R.J.M., 1966. Hydrogeology. John Wiley and Sons Inc, NY.

Gurunadha Rao V.V.S., Tamma Rao G., Surinaidu L., Rajesh R., Mahesh J., 2011. Geophysical and geochemical approach for seawater intrusion assessment in the Godavari Delta basin, A.P., India, *Water Air Soil Pollut*. 217,

1-4, 503-514, DOI: 10.1007/s11270-010-0604-9.

Howard G., Bartram J., 2003. Domestic water quality, service level and health. World Health Organization, Geneva.

Kirsch R., 2009. Groundwater geophysics, A tool for hydrogeology, 2nd edn. Springer Verlag, Berlin, 493p.

Kouzana L., Benassi R., Ben Mammou A., Felfoul M.S., 2010. Geophysical and hydrochemical study of the seawater intrusion in Mediterranean semi arid zones. Case of the Korba coastal aquifer (Cap-Bon, Tunisia). *J Afr. Earth Sci.,* 58, 2, 242–254.

Nowroozi A.A., Stephen B.H., Henderson P., 1999. Saltwater intrusion into the freshwater aquifer in the eastern shore of Virginia: a reconnaissance electrical resistivity survey. *J. Appl. Geophys.,* 42, 1–22. doi:10.1016/s0926-9851(99)00004-x.

Pulido-Leboeuf P., 2004. Seawater intrusion and associated processes in a small coastal complex aquifer (Castell de Ferro, Spain). *Appl. Geochem.,* 19, 1517–1527.

Sarwade D.V., Nandakumar M.V., Kesari M.P., Mondal N.C., Singh V.S., Singh B., 2007. Evaluation of seawater ingress into an Indian atoll. *Environ. Geol.,* 52, 2, 1475–1483. DOI 10.1007/s00254-006-0592-7.

Sawyer C.N., McCarty P.L., 1978. Chemistry of Environmental Engineering, 3rd ed. Series in Water Resources and Environmental Engineering, McGraw–Hill, NY.

Schoenleber J.R., 2005. Field Sampling Procedures Manual. Department of environmental protection, New Jersey, p 574.

Sharma P.V., 1997. Environmental and engineering geophysics. Cambridge University Press, Cambridge, 475 p.

Sherif M., El Mahmoudi A., Garamoon H., Kacimov A., Akram S., Ebraheem A., Shetty A., 2006. Geoelectrical and hydrogeochemical studies for delineating seawater intrusion in the outlet of Wadi Ham, UAE, *Environ. Geol*., 49, 4, 536-551, DOI: 10.1007/s00254-005-0081-4.

Store H., Storz W., Jacobs F., 2000. Electrical resistivity tomography to investigate geological structures of earth's upper crust. Geophys. Prospect., 48, 455–471.

Telford W.M., Geldart L.P., Sheriff R.E., 1990. Applied Geophysics, 2nd ed., Cambridge University Press, Cambridge, 770 p.

WHO 2008. Guidelines for drinking-water quality. World Health Organization, Geneva, Switzerland. 564p.

Geofísica Internacional (2016) 55-4: 255-266

Original paper

Establishing the range of background for radon variations in groundwater along the Serghaya fault in southwestern Syria

Mohamed Al-Hilal*

Received: September 06, 2015; accepted: June 21, 2016; published on line: October 01, 2016

DOI: 10.19155/geofint.2016.055.4.3

Resumen

Se midió la presencia a largo plazo de radón en el agua en dos manantiales kársticos que salen de la zona de falla de Serghaya en el suroeste de Siria. El objetivo de este trabajo es determinar el rango ambiental del radón a lo largo de dicha falla, lo cual en la región representa una rama promimete en el sistema de fallas de Mar Muerto. Se analizaron los datos obtenidos de forma estadística y los valores medios de radón fueron estandarizados en términos de probabilidad de magnitud, con la finalidad de permitir distinguir entre las variaciones normales de radón y las de otros valores anómalos o geotecnónicos. Los resultados revelaron una gama ambiental general de la concentración de radón que varía entre 5.000 y 13.000 Bqm^{-3} y, por lo tanto, todos los valores de radón que se encuentran fuera de este intervalo se consideraron anómalos. Sin embargo, existen ramas de altas concentraciones de radón con valores pico de más del doble a nivel de fondo; pudieron observarse durante el monitoreo en ambos muelles durante el periodo de 1992 a 1994. Estos valores anormales de radón se correlacionaron positivamente al momento de altas precipitaciones, y no se registró actividad sísmica durante este período. Por lo tanto, los cambios en la tensión de la cortesa no parecen verse reflejados en las concentración de radón, sino que la mayoría se debe a las altas precipitaciones. Lo anterior confirma la utilidad de la aplicación de radón como un importante indicador natural en investigaciones hidrogeológicas.

Palabras clave: Radón ambiental, agua subterránea, primavera kárstica, Falla de Serghaya, Syria

Abstract

Long-term groundwater radon measurements were carried out in two selected karstic springs emerging from the Serghaya fault zone in southwestern Syria. The work is aimed at determining the range of radon background along the concerned fault, which represents a prominent branch segment of the Dead Sea Fault System in the region. The obtained data was statistically analyzed and the mean radon values have been standardized in terms of probability of magnitude in order to enable the separation between normal radon variations from other anomalous or geotectonic related values. The results revealed a general background range of radon concentration varying between 5000 and 13000 Bqm^{-3}, and thus all radon values lying outside this range were considered anomalous. However, remarkable clusters of high radon concentrations with peak values more than twice times the background level, were observed in both monitoring springs through the period (1992-1994). These abnormal radon values were positively correlated with simultaneous time of high precipitations, while no significant earthquake activities were recorded in the region during that period. Therefore, such radon signals do not seem to be a reflection of regional changes in crustal strain, but rather they mostly indicate evidences of radon response to the groundwater table fluctuations due to high precipitations. These consequences may confirm the usefulness of radon application as an important natural tracer in hydrogeological investigations.

Key words: Radon background, groundwater, karstic spring, Serghaya fault, Syria

M. Al-Hilal*
Department of Geology
Atomic Energy Commission of Syria (AECS)
P.O Box 6091, Damascus, Syria
*Corresponding author: cscientific@aec.org.sy

Introduction

The western margins of the Arabian Plate are represented by an active divergent boundary of the Red Sea and the left lateral Dead Sea Fault System (DSFS) that extends for about 800 km from the Gulf of Aqaba in the south to the Taurus Mountain in southern Turkey. The system ranks among the largest strike-slip faults in the world and represents a key element of the Eastern Mediterranean tectonic framework (Barazangi *et al*., 1993; Brew *et al*., 2001). As the (DSFS) continues its way towards Lebanon and western Syria, it follows a great restraining bend that consists of several outstanding active segments including the Yammouneh fault (YF) and the Serghaya fault (SF). This study focuses mainly on the (SF), a remarkable branch of the (DSFS) cutting through the Anti-Lebanon ranges, with local deflection towards northeast (Figure 1).

Radon isotope (^{222}Rn), for simplicity called "Radon" in the following, is a daughter nuclide of radium (^{226}Ra), which in turn is produced from the decay series of uranium (^{238}U). As a naturally occurring radioactive gas, radon is widely utilized in various fields of earth sciences, such as hydrogeological studies Pane *et al*., 1995; Han *et al*., 2006; Surbeck, 2007); detecting buried active faults (Baubron *et al*., 2002; Al-Hilal and Al-Ali, 2010) and monitoring seismic activities (Teng, 1980; Kuo *et al*., 2006; Erees *et al*., 2007). Furthermore, radon method is commonly used in most uranium exploration programmes due to its efficiency, low cost and simplicity (Dyck, 1975; Gingrich, 1984; Jubeli *et al*., 2000).

The first national programme for correlating radon variations with seismic records of Syria began in 1992 and the results of those studies have been reported (Al-Hilal and Mouty, 1994). Afterwards, periodical radon measurements, based on monthly intervals, were continued during the nineties of the last century in western Syria (Al-Hilal *et al*., 1998). Further groundwater radon measurements were resumed during the years from 2007 to 2009 with particular focus on the Serghaya fault as

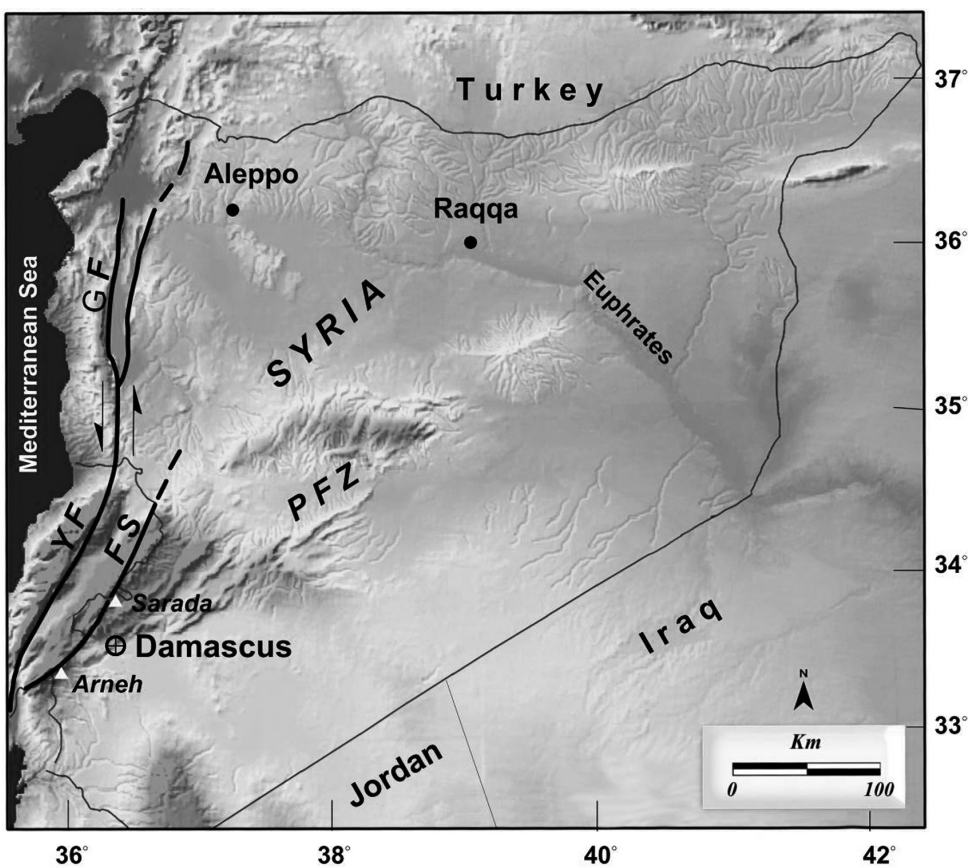

Figure 1 A location map showing the sites of *Arneh and Sarada* radon monitoring stations in southwestern Syria. Abbreviations; SF: Serghaya Fault, YF: Yammouneh Fault, GF: Ghab Fault, PFZ: Palmyride fold zone.

a unique active structural component of the (DSFS) in southwestern Syria. Considering the limited capability at this period of the radon monitoring programme in the country, it could be more reasonable to orient the efforts towards establishing the background of radon changes in groundwater as a range rather than as an absolute value. Such efforts would also help to set up an accessible data bank that may assist in evaluating the real potential hazard along the concerned fault and thereby reducing seismic risk in the region. Accordingly, the main objective of this study is to make use of the available set of radon data for setting the range of background for radon variations in groundwater along the Serghaya fault zone. The estimated range of background is regarded to be a significant step in the radon-monitoring programme, as it may assist the distinction of usual groundwater radon changes from other anomalous values that might be caused by either geotectonic disturbances or other hydrogeological and environmental factors.

Tectonic setting of the Serghaya fault zone

The Serghaya fault represents a major tectonic feature in Syria that can be traced approximately 120 km from the Golan Heights in southwestern Syria, traversing through the Syrian–Lebanese border to the eastern edge of the Bekaa Valley of Lebanon.

As a unique seismically active structure evinced by many historical catastrophic earthquakes, the northeast trending Serghaya fault attracted the interest of international earth scientists in the last decade who studied the tectonic evolution and the paleoseismicity of the region compiling various techniques (Ambraseys and Barazangi, 1989; Gomez *et al*., 2003). One of the main results of these researches reveals that the Serghaya fault is probably active and capable of generating large earthquakes in the future. These findings were based on extensive geologic observations and geomorphologic evidences of active

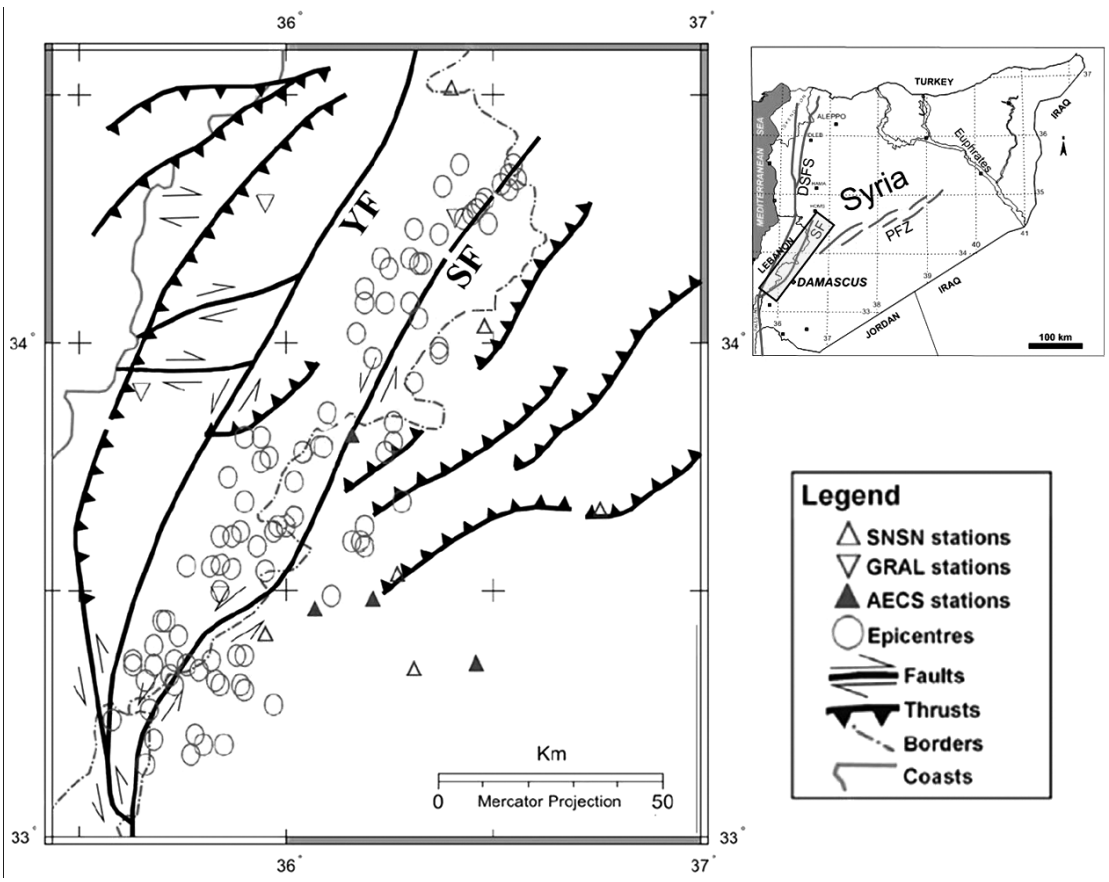

Figure 2. Distribution of earthquake epicenters (red circles) occurred on (SF) zone during the period 1995-2009. The triangles stand for the seismic stations of three networks: Syrian National Seismological Network (SNSN), Atomic Energy Commission of Syria (AECS), and Geophysical Research Arrays of Lebanon (GRAL). (Modified after Asfahani and Abdul-Wahed (2013)).

tectonics along the fault zone including large stream valley deflections, fault scarps and faulted recent alluvial deposits (Gomez *et al*., 2001). Thus, the concerned fault should be an essential element in any regional seismic hazard assessment, particularly with its close proximity to Damascus (30 km) and Beirut (60 km), two highly populated and cultivated cities.

On the other hand, Asfahani and Abdul-Wahed (2013) carried out a recent study based on the analysis of instrumentally observed earthquakes that occurred on Serghaya fault during the period (1995-2009). They found that little number of low magnitude events characterizes the Serghaya fault, with the biggest earthquake recorded during their study period not exceeding magnitude 3.9. Thus, they concluded that the fault might pass through a seismic quiescence extending from 1900 up to now, in comparison to other active branch segments of the (DSFS) such as the Yammouneh fault (Figure 2).

For that reason, there are only very limited data available on the application of radon measurement technique as an earthquake precursor along the concerned fault, except for the previous attempts made by the author (Al-Hilal and Mouty, 1994; Al-Hilal *et al*., 1998). The lack of such information is mostly due to the state of inactivity, which specifically characterized the (SF) zone at this current period. Nevertheless, radon monitoring technique has been extensively used elsewhere in the world for gaining additional information on precursory performance (Teng, 1980; Kuo *et al*., 2006). In addition, the tectonic influence of variable stress on underground radon concentrations has been successfully proved in several seismic regions throughout the world (Tansi *et al*., 2005). Radon concentrations may change in response to crustal motion, such as compression, expansion and tilting of the ground prior to and during an earthquake event. Such movements would be expected to form new microfractures and cracks and cause changes in the groundwater flow system with deformation of the water-bearing layers near the radon monitoring site (Choubey *et al*., 2007; Erees *et al*., 2007). These processes may enhance the release of radon from original rocks, and thereby increase its level in the groundwater. However, there is always a probability for false prediction, as radon increases do not conclusively prove a definite relation with earthquake activities. Therefore, radon changes in groundwater may be used only as an indicator of a regional stress build-up, and thereby a possible earthquake precursor.

Geological setting

Sedimentary and some volcanogenic rocks of Jurassic, Cretaceous, Paleogene, Neogene and Quaternary ages are the main geological formations exposed in the study area (Ponikarov, 1963). However, Jurassic and Cretaceous massive layers of limestone, dolomitic limestone and dolomite are the most common deposits that predominantly outcropped throughout Mount Harmon (2814 m. a. s. l) and Anti-Lebanon Chain Mountains in southwestern Syria. In view of that, two major lithological-stratigraphical successions of Jurassic and the Middle Cretaceous thick carbonate strata have extensively evolved into karstic aquifers in the region (Burdon and Safadi, 1965).

The general geology of the Sarada spring site consists mainly of a thin cover of sandy loams belonging to the Quaternary that underlain conglomerates and sands of Neogene age. The site is surrounded by a set of ring faults, separating the spring site from other older outcrops of karstified limestone and marl strata of Cretaceous age (Figure 3).

The site of Sarada spring is also bounded from the south by the Zabadani Valley, which is characterized by flat and gently dipping alluvial pebble beds and sandy clays of the Quaternary. Thick Cretaceous and Jurassic calcareous sequences underlie these formations uncomfortably. On the other hand, the rock exposures in the site of Arneh spring are mainly represented by Jurassic fractured complex aquifer of intensively thick karstified limestone and dolomite formations. Besides, evidence of past tectonic deformations such as extrusive volcanic dikes and steeply dipping faulting and V-shaped valleys can be also observed at the vicinity of the site of Arneh spring (Figure 4).

Finally, it is worth mentioning that the geological formations of the survey region, including the area of the Serghaya fault zone and its surroundings, are generally characterized by a notable decrease of radioactivity level due to the lack of any natural radioactive source such as igneous acidic rocks or other uraniferous formations. In view of that, radon concentration in soil gas measured in some geological outcrops in the close vicinity of Sarada and Arneh springs, were found to be generally low and varying between 3500 and 5000 Bqm^{-3} for the Quaternary sediments and recent soil cover; and from 1300 to 1500 Bqm^{-3} for limestone rocks. Furthermore, the result of chemical analysis, using γ-ray spectrometric

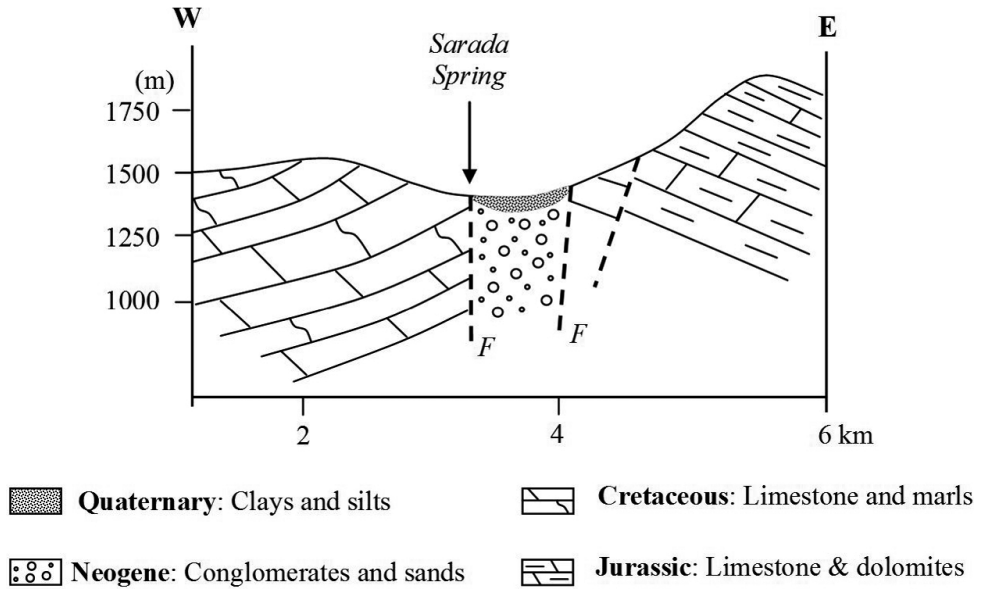

Figure 3. Geological cross-section through *Sarada* radon monitoring station. The dashed line is the position of the proposed fault (*F*).

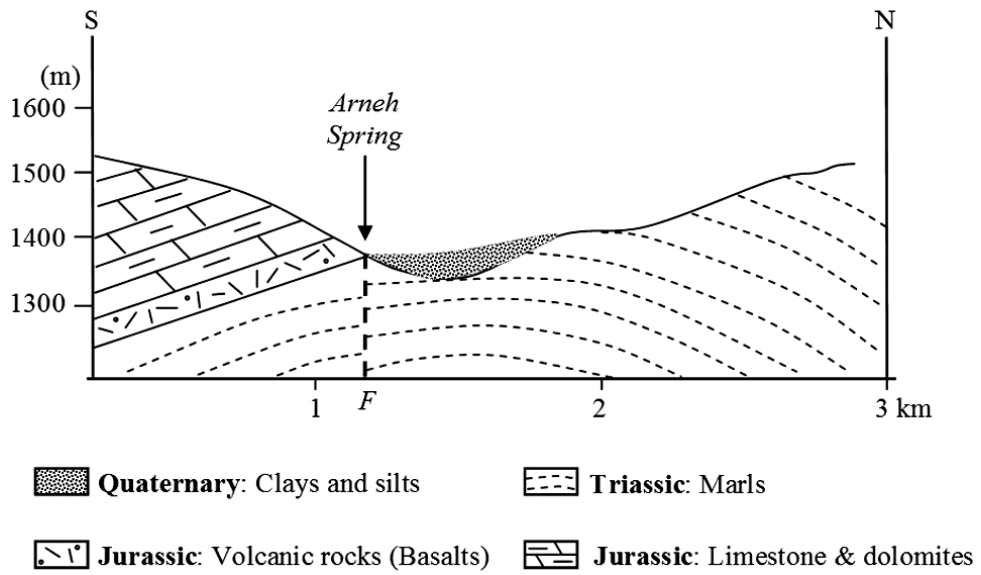

Figure 4. Geological cross-sections through *Arneh* radon monitoring station. The dashed line is the position of the proposed fault (*F*).

technique, for radium (^{226}Ra) concentration in water samples taken from Sarada and Arneh springs revealed low average values of 2±0.5 Bqm^{-3} and 2±1 Bqm^{-3} respectively.

Hydrogeochemical properties of the monitoring springs

Two main karstic springs, namely Sarada and Arneh were selected for long-term radon monitoring in groundwater along the Serghaya fault zone in southwestern Syria (Figure 1). The locations of these springs have been chosen according to data from the historical seismicity of Syria, (Sbeinati *et al*., 2005); geologic and geomorphologic evidences of active tectonics in the concerned area as reported by Gomez *et al*. (2003) as well as a detailed hydrogeological isotope survey in Damascus basin carried out by Kattan (1997).

Sarada monitoring station, (36°.16'E, 33°.80'N), represents a karstic spring emerging from Cretaceous carbonate strata on the northern side of the (SF) segment, 35 km northwest of Damascus, with altitude of 1380 meter above sea level (m.a.s.l). The Sarada aquifer exhibits circuit spring water that is characterized by a calcium-magnesium and bicarbonate water type (Ca-Mg-HCO_3). The hydrochemical properties of the Sarada spring revealed a quite fresh water since the total dissolved solids (TDS) equal 404 mg l^{-1}, the dominant pH value is 7.58, with average temperature of 13 °C and general electrical conductivity (E.C.) value of 473 µScm^{-1}.

Arneh station, (35°.88'E, 33°.36'N), is also a natural karstic spring emerging from Jurassic massif fissured rocks on the southern part of the (SF), at the centre of the Mount Hermon, 45 km southwest of Damascus, with altitude of 1358 (m.a.s.l). A calcium-magnesium and bicarbonate type also distinguishes the groundwater of Arneh spring, which is typically characterized the karstic aquifers in the area. The main hydrochemical parameters of the spring reveal fresh water with total dissolved solids (TDS) of 141 mg l^{-1}, 7.58 pH value, average temperature of 12 °C and general E.C. value of 222 µScm^{-1}.

Studying some major karst springs in Damascus limestone aquifer systems, Kattan (1997) found that groundwater bodies of most karst springs emerging from Anti-Lebanon mountain chain in southwestern Syria are mainly originated from direct infiltration of meteoric precipitation in the exposure zones with a strong positive relationship between infiltrated water of rainfalls and discharges. Further, the karstic aquifers in the region, including Sarada and Arneh springs, are characterized by the occurrence of fractures, conduits, sinkholes, caves and other karstified calcareous layers with high flow velocities of and relatively short transit time for the infiltrated rainwater to approach chemical equilibrium with rocks (Burdon and Safadi, 1965; Bakalowicz, 2005). Such extensive network of solution cavities would provide pathways for facilitating the movement of significant bulk flow of soil gases including radon, which is naturally released from rock surfaces and moves into the surrounding fluids where it can migrate by the mechanism of diffusion and fluid transport due to the influence of pore-fluid circulation processes. Thus, groundwater that is in contact with the radium-bearing rocks and soil will be a receptor of radon emanating from the surroundings geological environment by means of permanent alpha recoil in micro-pore or fracture walls. Although the radium activity in groundwater seems to be very low in both monitoring sites, as mentioned previously, the surface rainwater may possibly remove the available radon produced in the surficial soil cover and transport it down into the karst aquifer. Additional source of probable radon feeding could be due to the mechanism of pushing out old waters, after a long dry period, by the new arrival of fresh waters taking a considerable amount of radon during its passage through permeable layers at shallow depth.

Materials and methods

The apparatus used for degassing radon in groundwater was "Model WG-1001 Vacuum Water Degassing System" manufactured by Pylon Electronics, Canada. The instrument is designed for accurate and rapid extraction of radon from water samples. In practice, a 190 ml water sample is transferred to a graduated cylinder with the bubbler valve closed. The system is evacuated with a hand pump and the gas is drawn through a closed-circuit from the water sample into a scintillation cell coated internally with silver-activated zinc sulphide (Figure 5). Five minutes bubbling period was found to remove about 75 % of the dissolved radon from a 190 ml sample. The radon sample must be allowed to decay inside the scintillation cell for about three hours after sampling so that the radon daughters come into equilibrium with the radon gas. After that, the scintillation cell is placed into the counter (RM-1003 Radon Detector), where the alpha activity is measured in counts per minute, and then converted to radon concentration. The counter was frequently calibrated during the survey, using a standard test cell containing a source of ^{226}Ra with known activity. The calibrations ensured an acceptable detection limit, and thus it is believed that the measurements may give reasonable determinations of radon concentration in groundwater. Additionally, it is important to point out that the noticeable low values of radon concentration in groundwater of the study area could be justified in general by the low corresponding values of radium (^{226}Ra) content found in water samples taken from the same springs. The chemical analysis for ^{226}Ra was performed using γ-ray spectrometric technique, and the results revealed concentration values of 2±0.5 Bqm^{-3} and 2±1 Bqm^{-3} for Sarada and Arneh spring waters respectively. As mentioned previously, the reason for the general decrease of radioactivity levels over the surveyed geological area is mostly referred to the lack of any natural radioactive source such as granites or other igneous acidic rocks.

Results and discussion

Table 1 summarizes the basic statistical characteristics of radon data, which were performed along the Serghaya fault during the nineties of the last century, besides the years 2007 and 2009. The analysis includes the main hydrochemical properties of the monitoring springs, besides the mean value of radon concentration ($\bar{x}$), standard deviation (σ) and the coefficient of radon variability (CV%), which reflects the degree of homogeneity, the higher the coefficient of variability, the lower the homogeneity of the radon values. The (CV%) value is examined for the degree of radon variability in each monitoring station separately through the following formula:

$$CV\% = (\sigma / x) \text{ x } 100 \quad (1)$$

Where *CV* is the coefficient of variability, x is the mean value and σ is the standard deviation.

Radon concentration was sampled monthly for 89 and 70 times at Sarada and Arneh springs respectively. As the level of the measured radon concentration seemed to be quite variable, it was more realistic to view the radon background as a range rather than as an absolute value. For that reason, the abnormal radon values in both monitoring stations have been isolated, and the rest of the ordinary data were statistically analyzed in order to recognize a possible range of normal radon fluctuations in groundwater. In principle, the level of common

Table1. Radon and radium concentrations, besides some hydrochemical properties of two karstic springs emerging from the Serghaya fault zone, a branch of the Dead Sea fault system in southwestern Syria. Abbreviations; EC: electrical conductivity, TDS: total dissolved solids.

Monitoring Site	**Sarada Spring (33˚.80N, 36˚.16E)**	**Arneh Spring (33˚.36N, 35˚.88E)**
Geology of the aquifer	*Middle Cretaceous complex: karstified limestone, conglomerates and sands*	*Upper Jurassic complex: karstified dolomitic limestone, marls and basalts*
Altitude (m.a.s.l)	1380	1358
Number of radon samplings	89	70
Coefficient variability CV (%)	26	32
^{222}Rn mean value (Bqm^{-3})	8000±1500	9000±2000
^{226}Ra mean value (Bqm^{-3})	2±0.5	2±1
Water temperature (˚C)	13	12
PH value	7.58	7.96
E.C. (μScm^{-1})	473	222
TDS (mg l^{-1})	404	141

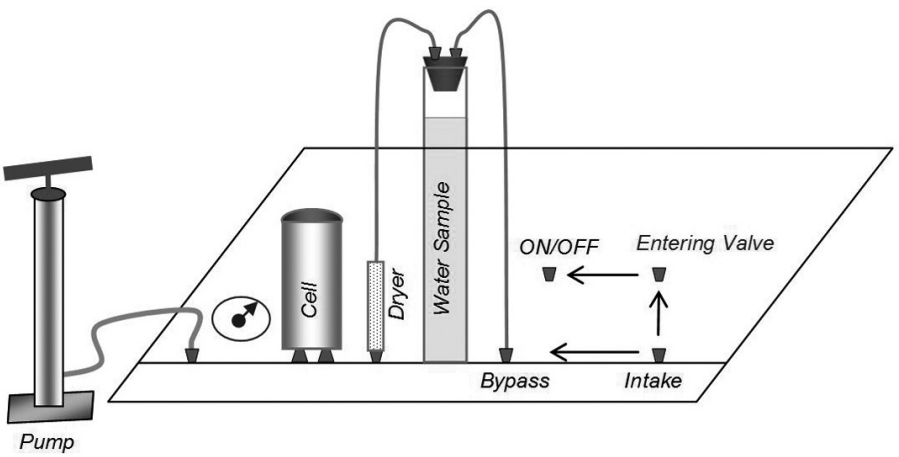

Figure 5. Schematic diagram showing the main parts of the Pylon WG-1001 Water Degassing System.

radon changes was estimated to be at the mean value plus or minus two standard deviations ($\bar{x}$ ±2σ), and any value of radon concentration out of this range could be assumed an anomaly. In view of that, the mean of normal radon value ($\bar{x}$) at Sarada station was determined as 8000 Bqm^{-3} with a standard deviation of 1500, compared to a mean value of 9000 Bqm^{-3} and a standard deviation of 2000 for Arneh station. As a result, it can be inferred that the majority of the normal radon data were concentrated within the range 5000-11000 Bqm^{-3} for Sarada spring (Figure 6a), and 5000-13000 Bqm^{-3} for Arneh spring (Figure 7a), which may be considered as the background values. According to these results, it can be noticed that a distinct number of anomalous radon signals were appeared in both monitoring stations, particularly during the time span from1992 to 1994. In other words, the radon time-series shown in Figures 6 and 7 revealed periods of synchronized radon anomalies, which occurred at a certain time but at no other times during the overall radon-monitoring period. One point of importance is the remarkable occurrences of these anomalously high radon values through the period 1992-1994, which represents the most wet duration in the study region during the 1990s (Abou Zakhem and Hafez, 2010). Besides, no significant seismic activities were recorded in the region throughout the same period (Asfahani and Abdul-Wahed, 2013). Thus, the noticeable increases of radon concentrations are most likely attributed to coincident increases of groundwater table due to high rainfalls, which normally leads to increasing the rate of discharge in the monitoring springs. These consequences may provide evidences of probable radon response to the oscillation of the groundwater table due to high precipitations, and thereby indicate the possible application of groundwater radon measurement as a useful tracer in hydrogeological studies.

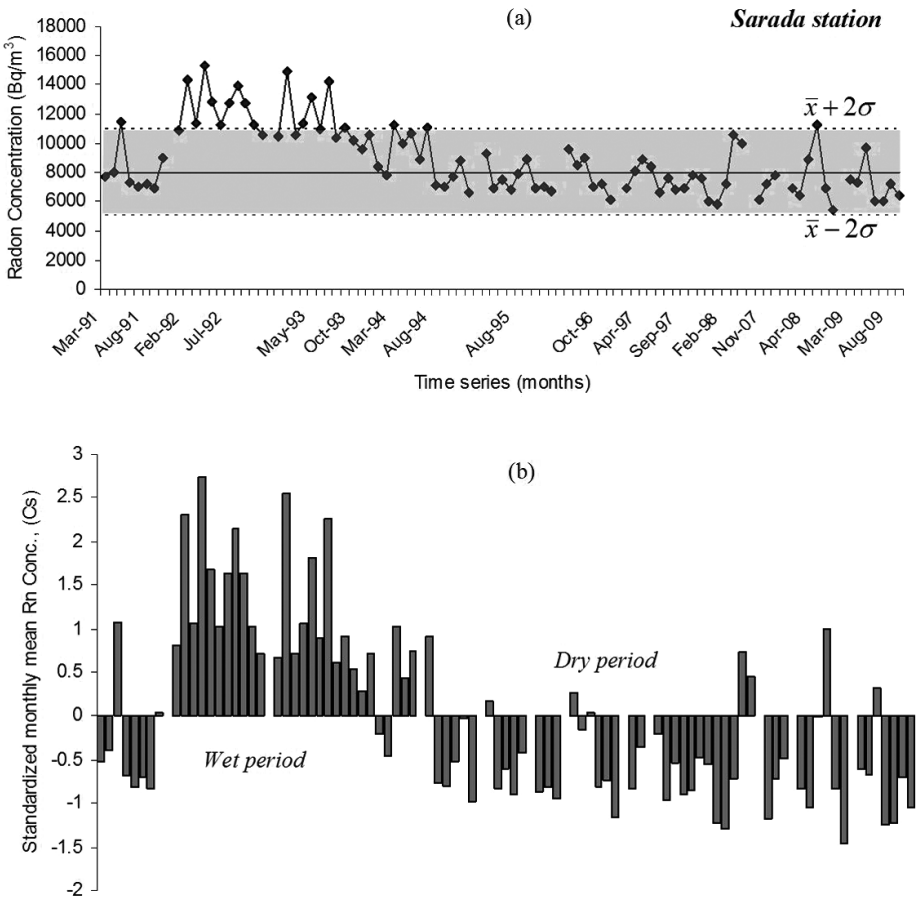

Figure 6. (a) Time series of groundwater radon concentration recorded monthly in Sarada station. The gray stripe indicates the range of normal radon background, (b) Standardized radon index, where positive values are correlated with the wet period, while negative values are related to the dry period..

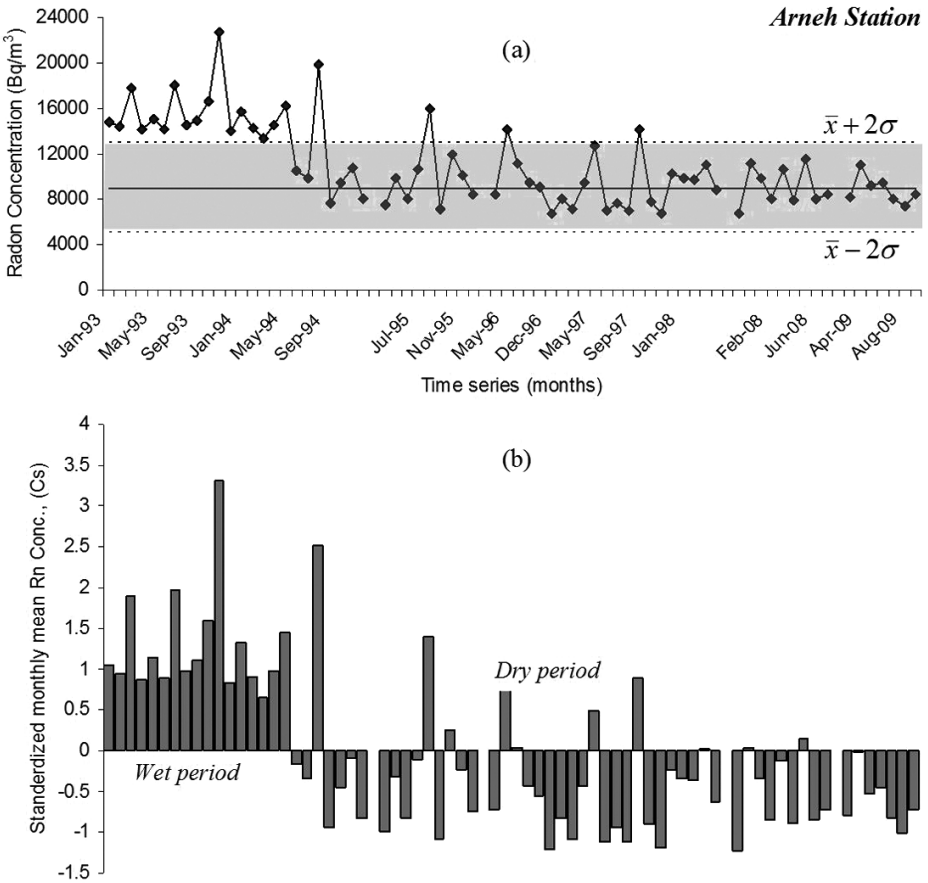

Figure 7. (a) Time series of groundwater radon concentration recorded monthly in *Arneh* station. The gray stripe indicates the range of normal radon background, (b) Standardized radon index, where positive values are correlated with the wet period, while negative values are related to the dry period.

In view of the prevailing climate of Syria, which is characterized by semi-arid to arid conditions, the country has undergone a sequence of dry periods since the early 1980s. These environmental circumstances caused a strong trend towards hydrological drought with a clear decline of the groundwater resources. According to the record of rainfall data from the meteorological station of Damascus region during the period 1919-2008, the annual precipitation varied from 60 to 360 mm/year, with mean annual precipitation of 202±15 mm/year. However, a remarkable wet time with annual mean value of 315 mm/year, appeared through 1992-1994, and it is regarded as the most rainy period in the concerned area during the 1990s (Abou Zakhem and Hafez, 2010). Considering the previously mentioned results, it can be deduced that the exceptional groundwater radon signals, which have been recognized through this study appear to be well related with the average rate of precipitations in the area. Additionally, the Syrian Irrigation Ministry (2003) completed a study of water resources in Damascus basin through the 1982 to 2004. The study includes the average of annual period discharge values for most of the springs emerging from the basin, and the results revealed average annual discharge values of ~0.03 m^3s^{-1} and ~0.6 m^3s^{-1} for Sarada and Arneh springs respectively. This may explain the differences in the general level of radon concentration in both monitoring stations, where the average of normal radon content in Arneh spring (9000 Bqm^{-3}) seems to be relatively higher than the normal radon average (8000 Bqm^{-3}) in Sarada spring. Besides, the coefficient of radon variability in Arneh spring shows a higher value (CV = 32 %), compared to a relatively lower value of (CV = 26 %) in Sarada spring (Table 1). This discrepancy might be due to the hydrogeological nature of the concerned aquifers and the differences in the average volume of groundwater discharges. Arneh spring flows from thick fractured Jurassic formations with relatively higher

discharge rate, compared to poor discharge of groundwater from Cretaceous carbonate rocks in Sarada spring.

In order to get a better insight into the variability of radon content in groundwater, both radon time-series were standardized in terms of probability magnitude, which could help in representing the data in terms of probability of occurrence, and thereby assist recognizing anomalous radon signals (Crockett and Holt, 2011). The monthly mean values of radon concentration, *Ci*, have been standardized, *Cs*, by using the following formula:

$$Cs = (Ci - x)/\sigma \qquad (2)$$

Where $\bar{x}$ and σ, are the mean and the standard deviation of the series, respectively. The Standardized Radon Index (SRI) is a dimensionless index that is comparable to the Standardized Precipitation Index (SPI), where negative values indicate drop in the radon level, probably due to drought conditions (dry period) and positive or anomalous radon values may point to wet periods due to high precipitations (Figures 6b and 7b). The result of the standardized radon data shows synchronized peaks of similar durations corresponding to the wet period of 1992–1994.

Nevertheless, and apart from the influences of the wet period (1992-1994), the curves of radon concentration at both monitoring stations appear to fluctuate more or less around the mean value, except for some cases in which the radon level crosses the limits of the estimated range of normal radon variations, especially in Arneh spring (Figure 7). This reveals that radon concentration, during this monitoring period, does not appear to remain steady within a certain range, but rather it shows some changes with some abnormal peak values that appear in particular times through the dry period. These infrequent radon signals are most likely associated with the flood times that commonly occur at the end of the annual rainfall seasons, where groundwater table usually increases in the region during April and early May each year. Many researchers (e.g. Pane *et al*., 1995; Han *et al*., 2006; Surbeck, 2007) discussed the hydrogeological control of radon variations in karstic aquifers and the spatial correlation with changing groundwater levels of the monitoring site due to decreasing or increasing precipitations. In view of their results, it has been found that occasional radon changes in groundwater usually appear in a restricted time of the year announcing the arrival of the new percolating rainwater after the rainfall season. Such increases of radon concentration in groundwater are most likely related to the effect of rainfall events, which cause the water table to rise up driving radon gas toward the surface. In addition, the infiltration of rainwater could also remove a considerable amount of radon from the ground during its passage through permeable layers at shallow depth. Subsequently, any radon input from the shallow layers covering the aquifer would be evidently detectable in the spring waters. Thus, radon concentration level and the discharge rate are usually correlated for most springs (Eisenlohr and Surbeck, 1995). Therefore, it is quite essential to consider such observations especially when measuring radon in seismically active areas. In fact, the radon signals, which are caused by hydrogeological processes, represent occasional and isolated changes that are usually confined to a wet period or a certain time of the year, commonly after high rainfall season. Whereas the seismic-induced radon variations represent a gradual increase followed by sudden changes with sharp peaks, and they are normally related to stress build-up or ground motion due to tectonic disturbances, which may occur at any time of the year.

From the seismic point of view, although the seismic record of the Serghaya fault reveals that the fault is historically active (Gomez *et al*., 2001; Sbeinati *et al*., 2005), the present earthquake activity along the fault zone is quite low, with no coincident occurrences of any major seismic events during the time of this monitoring period (Dakkak *et al*., 2005). Moreover, Asfahani and Abdul-Wahed (2013) have performed a comprehensive evaluation of earthquake activity along the (SF), including the establishment of an earthquake catalogue for the concerned fault through the period from 1995 to 2009. They found that the earthquake activity along the (SF) produces little number of low-magnitude events. Therefore, it is thought that the fault passes currently through a relative quiescence, in comparison to other active seismic parts of the (DSFS), such as the (YF) of Lebanon and the Gulf of Aqaba. Accordingly, hydrogeological processes rather than seismic activities are presumably the main factors controlling the variations of radon concentration in groundwater of both monitoring springs, particularly through the wet period 1992–1994.

Conclusion

Based on statistical analysis of long-term radon measurements data from two karstic springs located on the Serghaya fault zone, the range of background for radon variations were found

to be varying between 5000 and 13000 Bqm^{-3}, and all values of radon concentration beyond this range are assumed to be anomalous. Radon time-series revealed periods of synchronized anomalies, which appeared at a certain time during the overall radon monitoring period. These anomalous radon signals were positively correlated with a remarkable wet period prevailed through the years (1992-1994), whereas no significant seismic activity occurred in the region during that period. The correlation between the level of radon concentration and the rate of precipitation has been interpreted using the Standardized Radon Index (SRI), which enhanced the comparison process of data, and showed simultaneous radon peaks of similar durations corresponding with the above mentioned wet period. These observations clearly indicate that hydrogeological processes and the rate of groundwater discharge are the main factors controlling the variations of radon level in groundwater in both springs through the time window of this monitoring. On the other hand, the present study proved also the importance of establishing the range of background for radon changes in groundwater, which may assist the separation between common radon fluctuations from other anomalous values. Determining such range of background would be a useful step in the ongoing research programme for future monitoring of the Serghaya fault, which represents a prominent seismic segment of the (DSFS) in southwestern Syria, in order to evaluate its seismic hazard and behavior.

Acknowledgment

The author would like to express his gratitude and thanks to Professor I. Othman, Director General of the Atomic Energy Commission of Syria (AECS), for his constant encouragement. Thanks are also due to all my colleagues in the Geology Department of (AECS) for their support. I gratefully acknowledge the anonymous reviewers for their valuable comments and suggestions that substantially improved the quality of the manuscript.

References

Abou Zakhem B., Hafez R., 2010, Climatic factors controlling chemical and isotopic characteristics of precipitation in Syria. *Hydrol. Process.*, 24, 18, 2641-2654.

Al-Hilal M., Al-Ali A., 2010, The role of soil gas radon survey in exploring unknown subsurface faults at Afamia B Dam, Syria. *Rad. Meas.,* 45, 219-224.

Al-Hilal M., Mouty M., 1994, Radon monitoring for earthquake prediction on Al-Ghab fault of Syria. *Nucl. Geophys.,* 8, 291-299.

Al-Hilal M., Sbeinati R., Darawcheh R., 1998, Radon variations and microearthquakes in western Syria. *App. Rad. Isot.,* 49, 117-123.

Ambraseys N., Barazangi M., 1989, The 1759 earthquake in the Bekaa valley: implications for earthquake hazard assessment in the East Mediterranean Region. *J. Geophys. Res.,* 94, 4007-4013.

Asfahani J., Abdul-Wahed M., 2013, Evaluation of Earthquake Activity along the (SF), Syria, from Instrumental Seismic Data. *Acta Geophys.,* 61, 37-59.

Bakalowicz M., 2005, Karst groundwater: a challenge for new resources. *Hydrogeol. J.,* 13, 148–160.

Barazangi M., Seber D., Chaimov T., Best J., Litak R., Saad D., Sawaf T., 1993, Tectonic evolution of the northern Arabian plate in western Syria. Recent Evolution and Seismicity of the Mediterranean Region, E. Boschi *et al*. (eds.), PP.117-140.

Baubron J.C., Rigo A., Toutain J.P., 2002, Soil gas profiles as a tool to characterize active tectonic areas: the Jaut Pass example (Pyrenees, France). *Earth Planet. Sci. Lett.,* 196, 69–81.

Brew G., Barazangi M., Al-Maleh A.K., Sawaf T., 2001, Tectonic and geologic evolution of Syria, *GeoArabia*, 6, 573–616.

Burdon D.J., Safadi C., 1965, The karst groundwaters of Syria. *J. Hydrol*., 2, Issue 4, p. 324-347.

Choubey V.M., Mukherjee P.K., Bajwa B.S., Walia Vivek, 2007, Geological and tectonic influence on water–soil–radon relationship in Mandi–Manaliarea, Himachal Himalaya. *Environ. Geol.,* 52, 1163–1171.

Crockett RGM, Holt C P., 2011, Standardised Radon Index (SRI): a normalization of radon data-sets in terms of standard normal variables. *Nat. Hazards Earth Syst. Sci.,* 11, 1839–1844.

Dakkak R., Daoud M., Mreish M, Hade G., 2005, The Syrian National Seismological Network (SNSN): Monitoring a major continental transform fault. *Seismol. Res. Lett.,* 76, 437-445.

Dyck W., 1975, Geochemistry applied to uranium exploration. Uranium Exploration, 75, *Geol. Surv. Can.*, pp. 33-47.

Eisenlohr L., Surbeck H., 1995, Radon as a natural tracer to study transport processes in a karst system; an example from the Swiss Jura, C.R. Acad. Sci. Paris, t.321, série IIa, 761-767.

Erees F.S., Aytas S., Sac M.M., Yener G., Salk M., 2007, Radon concentrations in thermal waters related to seismic events along faults in the Denizli Basin, Western Turkey. *Rad. Meas.,* 42, 80–86.

Gingrich JE., 1984, Radon as geochemical exploration tool. *J. Geoch. Exp.,* 21, 19-39.

Gomez F., Meghraoui M., Darkal AN., Sbeinati R., Darawcheh R., Tabet C., Khawlie M., Charabe MK., Barazangi, M., 2001, Coseismic displacements along the (SF): an active branch of the (DSFS)in Syria and Lebanon, *J. Geol. Soc*., 158, 3, 405-408.

Gomez F., Meghraoui M., Darkal AN., Hijazi F., Mouty M., Suleiman Y., Sbeinati R., Darawcheh R., Al-Ghazzi R., Barazangi M., 2003, Holocene faulting and earthquake recurrence along the Serghaya branch of the (DSFS)in Syria and Lebanon, *Geophys. J. Int*. 153, 3, 658-674.

Han YL., Tom Kuo MC., Fan KC., Chiang CJ., Lee YP., 2006, Radon distribution in groundwater of Taiwan. *Hydrogeol. J.,* 14, 173–179.

Jubeli Y., Al-Hilal M., Rajja G., Al-Ali A., 2000, Radiometric Profiles of Uranium Dispersal Pattern Adjacent to Cretaceous Phosphatic Sediments in Wadi Qasser Al-Hallabat Basin, Central Syria. *Exp. Min. Geol.,* 7, 4, 313-319.

Kattan Z., 1997, Environmental isotope study of the major karst springs in Damascus limestone aquifer systems: Case of the Figeh and Barada springs. *J. Hydrol.,* 193, 161-182.

Kuo T., Fan K., Kuochen H., Hana Y., Chuc H., Lee Y., 2006, Anomalous decrease in groundwater radon before the Taiwan M6.8 Chengkung earthquake. *J. Environ.Rad.,* 88, 101-106.

Pane MB., Seidel JL., Monnin M., Morin JP., 1995, Radon as a tracer of fluid motion in fractured aquifers. Gas Geochemistry, Edited by Claude Dubois, University of Franche-Comte, Besancon, France 325-334.

Ponikarov VP., 1963, The Geological Map of Syria, Damascus sheet, scale 1:200000, Technoexport, Ministry of Industry, Damascus, Syria.

Sbeinati R., Darawcheh R., Mouty M., 2005, The historical earthquakes of Syria: an analysis of large and moderate earthquakes from 1365 B.C. to 1900 A.D., *Ann. Geophy.,* 48, 3, 347-435.

Surbeck H., 2007, Dissolved gases as natural tracers in karst hydrogeology; radon and beyond. Center of Hydrogeology (CHYN), University of Neuchâtel, Emile-Argand 11, CH- 2007 Neuchâtel, Switzerland.

Syrian Irrigation Ministry, 2003, Water Resources in "Barada and Aa-waj Basin", unpublished internal report in Arabic, 170p.

Tansi C., Tallarico A., Iovine G., Folino Gallo M., Falcone G., 2005, Interpretation of radon anomalies in seismotectonic and tectonic-gravitational settings: the south-eastern Crati graben (Northern Calabria, Italy). *Tectonophysics*, 396, 181–193.

Teng T., 1980, Some recent studies on groundwater radon content as an earthquake precursor. *J. Geophys. Res*., 85. 3089.

Geofísica Internacional (2016) 55-4: 267-274

Original paper

Cardiovascular mortality in northwestern Russia in relation with geomagnetic disturbances

Oleg Shumilov*, Elena Kasatkina, Tatiana Koshcheeva and Alexey Chramov

Received: January 08, 2016; accepted: August 08, 2016; published on line: October 01, 2016

DOI: 10.19155/geofint.2016.055.4.4

Resumen

El objetivo del estudio fue identificar en el noroeste de Rusia los impactos de las perturbaciones geomagnéticas, los factores socioeconómicos y antropogénicos en la mortalidad causada por enfermedades cardiovasculares (CVE, por sus siglas en ingles). Se analizaron 9,057 muertes por CVE en la ciudad de Kirovsk (península de Kola, 67.6 N, 33.7 E), relacionadas con las estaciones del año de 1948 a 2010. Se aprecian tres picos significativos en el número total de muertes en varones por CVE: en mayo, septiembre e invierno. El pico máximo de mayo predominó para los varones, excepto en la población de mayor edad (≥ 70 años). Parece que se relaciona con cuestiones emocionales y físicas derivadas del aumento de hormonas en primavera. En cuanto a las mujeres, se mostraron dos máximos significativos de muertes por CVE en otoño e invierno, y un pico en primavera insignificante. La distribución estacional de las tormentas geomagneticas moderadas (50 <Ap<100 nT) tenía un patrón bimodal con picos de primavera y otoño. Este patrón bimodal derivado de la variación estacional también se encuentra presente en los grupos mayores de edad (≥ 70 años), tanto en hombres como en mujeres. El análisis con el Método Multi-Taper (MTM, por sus siglas en inglés) reveló períodos de ~9-10 años, ~ 4.7 años y ~2.3 años, con un nivel de certeza de ≥90%. Estos períodos parecen coincidir con los principales ciclos de variaciones del índice aa de la actividad geomagnética. En la región de este estudio no se detectó una relación significativa entre la contaminación atmosférica y la mortalidad por enfermedades cardiovasculares.

Palabras clave: actividad geomagnetica, muertes por enfermedades cardiovasculares.

Abstract

The aim of the study was to identify the impact of natural (geomagnetic disturbances), socioeconomic and man-made factors on mortality from cardiovascular diseases (CVD) in Northwestern Russia. Data from 9057 CVD deaths in Kirovsk town (Kola Peninsula, 67.6 N, 33.7 E) were analyzed with respect to seasons of the year from 1948 to 2010. Total male CVD deaths showed three significant peaks in May, September and winter. The May maximum was dominant for all males, except for the oldest age (≥70 years) group and seemed to be caused by emotional and physical effects of increased hormones in spring. Total female CVD deaths showed two significant maxima in autumn and winter and one insignificant spring peak. Seasonal distribution of the moderate (50<Ap<100 nT) magnetic had a bimodal pattern with spring and autumn peaks. This bimodal pattern of seasonal variation is also present in the female and male oldest age (≥70 years) groups. Multi-Taper-Method (MTM) spectral analysis revealed periods of ~9-10 years, ~4.7 years and ~2.3 years at confidence level of ≥90%. These periods seem to coincide with the main cycles of variations of the aa-index of geomagnetic activity. There is no significant association of air pollution and CVD mortality at the region.

Key words: geomagnetic activity, cardiovascular deaths.

O. Shumilov*
E. Kasatkina
Polar Geophysical Institute
Fersmana str. 14, 184209 Apatity
Murmansk Oblast, Russia
*Corresponding author: oleg@aprec.ru

T. Koshcheeva
Main Hospital, Kola Science Centre RAS
Fersmana str. 58a, 184209 Apatity
Murmansk Oblast, Russia

A. Chramov
Baltic State Technical University
Krasnoarmeyskaya str. 1, 197372
St.-Petersburg, Russia

Introduction

According to the World Health Organization, every year about 17 million people globally die of Cardiovascular diseases (CVD), particularly from heart attacks and strokes. CVD remain to be the leading cause of mortality, accounting for nearly 50% of all deaths in the European Region (WHO, 2013). Development of the demographic crisis in the past decade in Russia made it necessary to study the dynamics of CVD mortality.

When studying the impact of environmental parameters changes on the dynamics of CVD-related deaths a question arises about the relative role of socioeconomic and natural factors. In Russia mortality has increased steeply in the first part of the 1990s, after the collapse of the Soviet Union (Shkolnikov *et al*., 1998; Norstrom, 2011). Possible explanations of this recent phenomenon have been discussed in the literature including social stress, medical care collapse, environmental pollution or alcohol consumption (Shkolnikov *et al*., 1998; Norstrom, 2011). All these interpretations were socioeconomic in nature. On the other hand, a number of studies were devoted to a possible relationship between some heliogeomagnetic factors and CVDs (Villorezi *et al*., 1994a,b; Stoupel *et al*., 1995; Shumilov *et al*., 1998, 2003; Halberg *et al*., 2000; Cherry, 2002; Cornelissen *et al*., 2002; Palmer *et al*., 2006; Kleimenova *et al*., 2007; Breus *et al*., 2008; Mendoza and Diaz-Sandoval, 2000; Mendoza and de la Peña, 2010; Diaz-Sandoval *et al*., 2011; Samsonov *et al*., 2014). For example, a significant increase has been established in the heart attacks and strokes (13% and 7.5% respectively) during large magnetic storms (Breus *et al*., 2008). Unfortunately, most of these studies were performed at low and middle latitudes, where the effect of heliogeophysical factors is insignificant. Conversely, at high latitudes, where electromagnetic disturbances caused by solar activity are strongest and, therefore, can be regarded as one essential environmental factor, almost no such studies were carried out. There are only few works concerning the effect of cosmophysical factors on human health in the magnetically active auroral zone (Shumilov *et al*., 2003, 2014) and in the relatively geomagnetically quiet polar cap zone (Shumilov *et al*., 1998) and subauroral latitudes (Samsonov *et al*., 2014).

In this work, we aimed to establish the effect of geomagnetic disturbances and other environmental factors on CVD mortality in the town of Kirovsk (Kola Peninsula, Northwestern Russia), which is known to be in the zone of maximum occurrence of auroras and their related geomagnetic disturbances.

Data and methodology

Statistical data of the period 1948-2010 (756 months) for Kirovsk town (67.6 N, 33.7 E) have been used in the analysis. Date, gender and age were recorded for each case. Information for this study was obtained from the official death certificates that were collected in the registry office.

Kirovsk is a town on the Kola Peninsula, 175 km south of Murmansk, with a population of approximately 30 thousands. It is located right at the auroral zone of geomagnetic activity, where the intensity and occurrence level of geomagnetic disturbances and pulsations grow in a wide frequency band. On the other hand, Murmansk Oblast is one of the industrialized and densely populated regions of Russia, where copper-nickel, iron, apatite-nepheline and rare-earth ores are widely developed and processed.

The rates of CVD mortality were calculated (number of cases per 100 thousand people) both for women and men. The seasonal distribution data validity was verified with the help of Student criterion, using MATLAB applied software package. Periodicity studies in yearly number of CVD deaths were determined using the Multi-Taper Method (MTM) of the power spectrum analysis (Thomson, 1982), detrending the time series to obtain stationarity carried out by subtracting the trend (5th order polynomial fit). MTM spectral analysis was performed with the help of the SSA-MTM software toolkit (Ghil *et al*., 2002). Significance was tested at the 90% and 95% confidence level against a red-noise background (Ghil *et al*., 2002).

The Ap and *aa* indexes are measures of the general level of geomagnetic storm activity over the planet. In this study, daily Ap indices from 1 January 1948 to 31 December 2010 were obtained from the World Data Centre for Geomagnetism, Kyoto, Japan (http://wdc.kugi.kyoto-u.ac.jp). The yearly *aa* indexes were from the British Geological Survey (www.geomag.bgs.ac.uk).

Results

During the period (1948-2010) 9057 CVD deaths were investigated, 4082 of them were men. It is known that CVDs occur almost

equally in men and women, which is confirmed by the statistical data for Kirovsk. The largest number of CVD deaths occurred in 2002 (953.9 persons per 100 thousand people) and the smallest one occurred in 1960 (113.7).

Figure 1 presents variations of the rates of mortality from cardio-vascular diseases (I_h) in Kirovsk during the period 1948-2010. A sharp increase is seen in the CVD mortality level since 1991 (more than twice compared to the period of 1948-1990), which, most likely, was connected with socio-economic stresses of that period. As we can see from Figure 1a, in the first maximum of the curve (1996) the value of the rate (I_h=623) of CVD mortality exceeds almost three times the average value for the period of 1948-1990 (I_h=230). The detrended data are shown in Figure 1B.

MTM spectral analysis was applied to the annual detrended time series of I_h. MTM analysis revealed periods of ~9-10 years, ~4.7 years and ~2.3 years at confidence level of ≥90% (see Figure 2A). These peaks seem to coincide with the main spectral peaks of the aa-index of geomagnetic activity (see Figure 2B).

Seasonal patterns of CVD mortality for the period of 1948-2010 are illustrated in Figure 3. The comparative analysis revealed significant differences in seasonal distributions of CVD mortality in relation to sex and age groups. As we can see from Figure 3A, total male CVD deaths show two significant peaks in May and September. Another winter peak is also present, but is not significant. The May maximum is dominant for all males, but not for the oldest age (≥70 years) group (Figure 3B). In the oldest age group winter and September peaks are significantly higher, than the annual average (see Figure 3B). Total female CVD deaths show two significant maxima in winter and autumn and one insignificant spring peak (see Figure 3C). Seasonal distribution of the moderate magnetic storms for the period studied is also presented in Figure 3D. The bimodal pattern of spring and autumn peaks is evident at this distribution (see Figure 3D). This bimodal pattern of seasonal variation is also presented in the female and male oldest age (≥70 years) groups (see Figures 3B, C). It should be noted that winter peaks are presented in all seasonal variations of CVD death events.

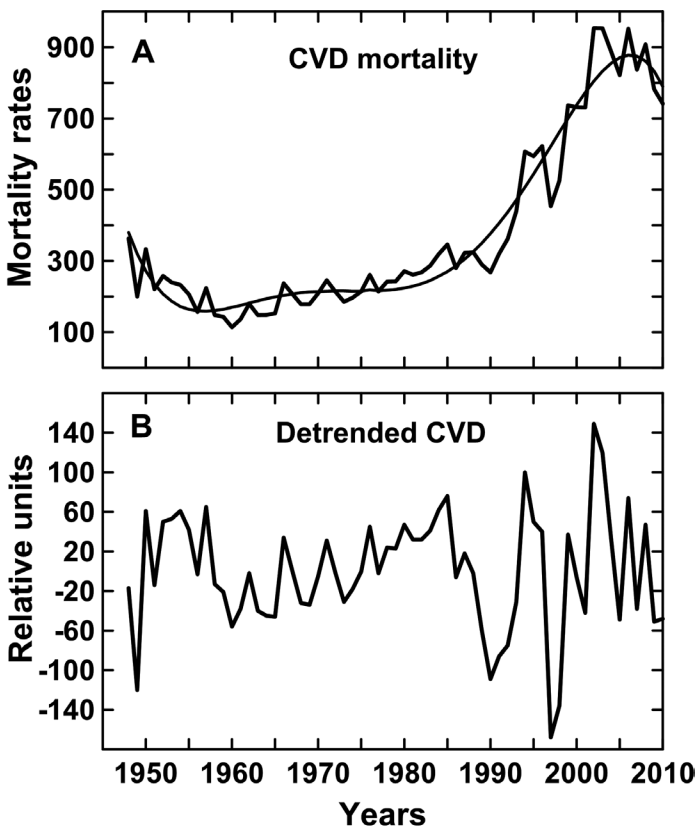

Figure 1. Variations of CVD mortality rates (the number of deaths per 100 000 persons) at Kirovsk during 1948-2010. (A) Original time-series (thick line) and a 5th order polynomial fit (dashed line). (B) Detrended CVD data obtained by subtracting the polynomial fit.

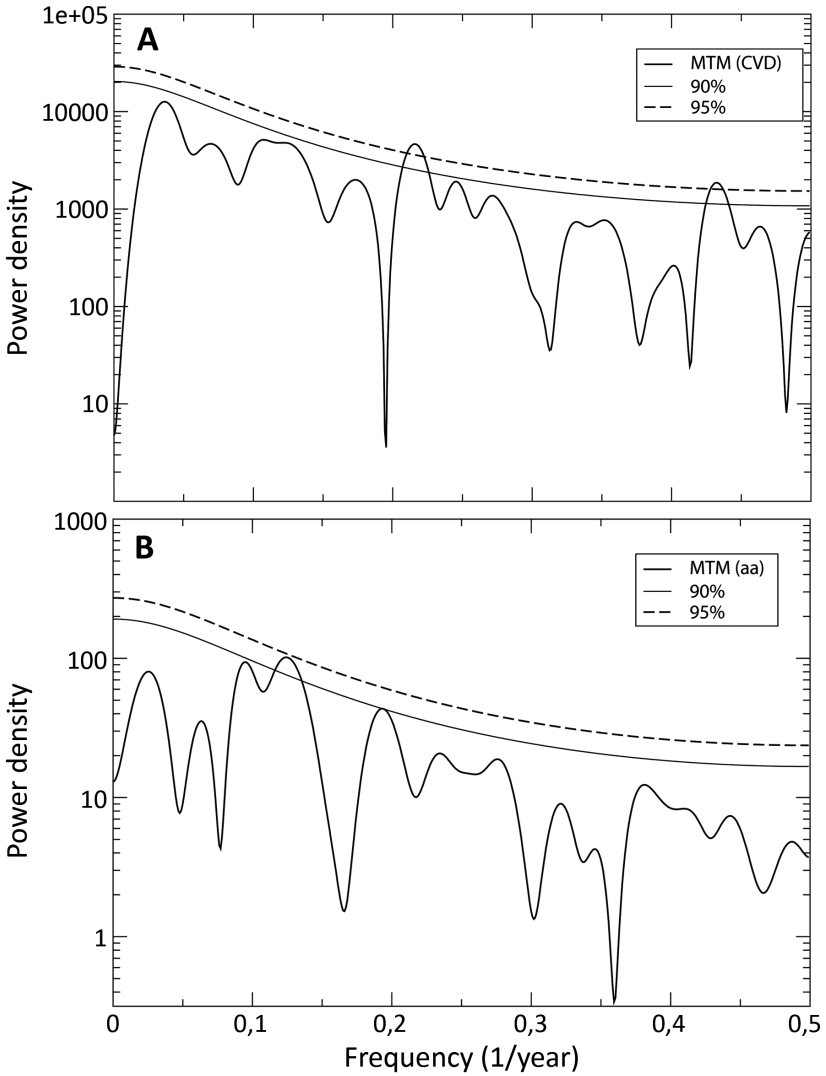

Figure 2. MTM spectrum analysis of CVD mortality rates at Kirovsk (A) and geomagnetic aa-indexes (B) over 1948-2010. The thin and dashed lines denote the 90% and 95% levels of significance respectively.

In this paper, the effect of air pollution on CVD mortality was assessed. Murmansk Oblast is one of the industrialized and densely populated regions of Russia. The world's largest producer of phosphate-based fertilizers Apatit company is located in Kirovsk. Another largest Russian nickel-copper plant "Severonikel" is located in the town of Monchegorsk (67.9N, 32.9E) at a distance of 80 km from the town of Kirovsk. Figure 4 shows the variation of CVD mortality I_h in Kirovsk and emissions of copper Cu, nickel Ni, sulfur dioxide SO_2 and solid substance Sd from "Severonikel" plant for the period from 1995 to 2009 (Karnachev *et al*., 2014). It is clearly seen that any connection between CVD deaths and air pollution does not exist.

Discussion

As it was noted earlier, a sharp increase has been observed in CVD death rate since 1991 (more than twice compared to the period of 1948-1990), which, most likely, was connected with socio-economic stresses during that time in Russia (see Figure 1A). It should be as well noted that in some studies this growth of mortality in Russia is explained by the end of the anti-alcohol campaign and increased alcohol consumption in the 1990s (Shkolnikov *et al*., 1998; Norstrom, 2011). Sure, as one can see from Figure 1b, some reduction in CVD mortality in the period of 1985 – 1991 seemed to be nearly connected to the period of the anti-alcohol campaign, but it was not

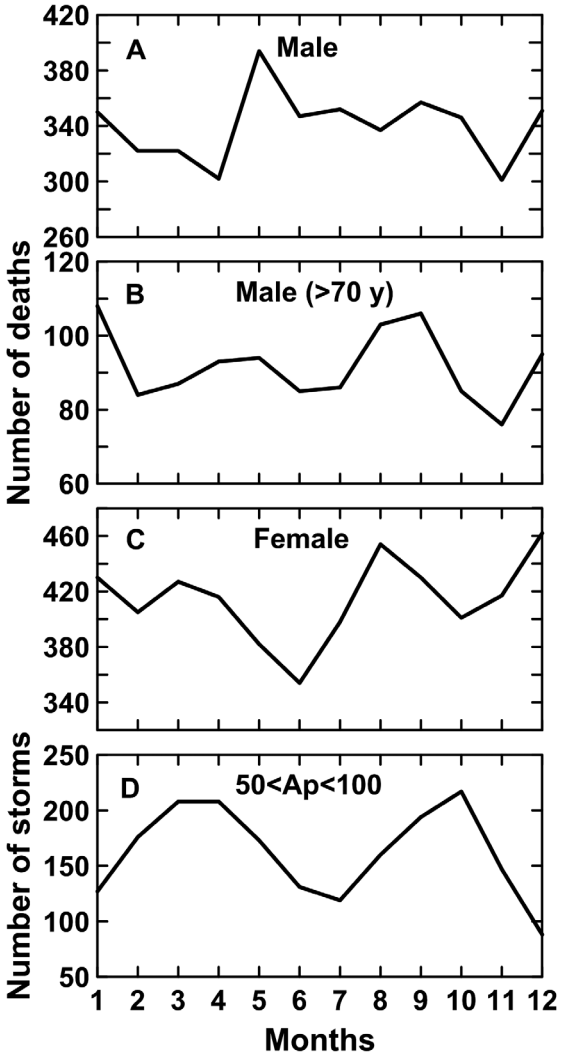

Figure 3. Seasonal distribution of the number of CVD deaths at Kirovsk for total male (A), for male old age (> 70 years) group (B) and for total female (C); seasonal distribution of the moderate (50<Ap<100 nT) magnetic storms (D).

significant compared with other variations. The subsequent sharp increase in CVD deaths was significantly higher than the previous level of it. This result does not contradict with the conclusion that socioeconomic dispossession might have been considered as a possible risk factor for CVD deaths (Pujades-Rodrígues *et al*., 2014).

Kola Peninsula is located within the auroral zone of geomagnetic activity. Due to the specific configuration of the geomagnetic field lines high latitudes are quite different from middle and low latitudes in the intensity and the spatial and temporal characteristics of the cosmophysical factors. As a rule those factors are more pronounced at here. The influence of cosmophysical factors on human health is reflected in Figure 2. Here the results of MTM-spectrum analysis of CVD death rate are given. Analysis of the distribution of CVD deaths in Kirovsk revealed periodicity of ~9-10 years attributed to solar cycle. The periods of ~4.7 years and ~2.3 years observed are also correlated with similar periodic variations in and geomagnetic aa-indexes (see Figure 2B). These periods seem to be the third and the fifth harmonics of the 11-year solar cycle, respectively.

Total female CVD deaths demonstrate two significant peaks in winter and autumn and one non significant spring peak (see Figure 3C). A similar pattern in CVD deaths is evident in the male oldest age (≥70 years) group (see Figure 3B). The bimodal pattern of seasonal variation with two equinoctial maxima is also presented in the seasonal distribution of the moderate magnetic storms (see Figure 3D). It is as well known that the bimodal pattern of seasonal variation with equinoctial maxima in March-April and September-October is typical for the distribution of the magnetic storms in the weak-to-moderate categories of storm intensity (Gonzalez *et al*., 2002). This seems to be connected to the seasonal change in the geometry of the Earth's magnetic field relative to the direction of the interplanetary magnetic field (Russel and McPherron, 1973). At the same time, it seemed to be difficult to associate the presence of the winter peak in total CVD deaths with geomagnetic activity. Note, that the seasonal pattern of CVD mortality with a winter peak is observed at some countries in both the Southern and Northern hemispheres, being higher at middle latitudes (Douglas *et al*., 1995; Douglas and Rawles, 1999; Healy 2003; Kleimenova *et al*., 2007; Diaz-Sandoval *et al*., 2011; Marti-Soler *et al*., 2014). Thus, the effect of winter peak in CVD mortality has a global nature. At some studies it had been concluded that temperature alone cannot explain the winter peak in CVD deaths (Douglas and Rawles, 1999; Healy, 2003; Diaz-Sandoval *et al*., 2011). As it concerns the May maximum in total male CVD deaths a similar result was obtained for all male admissions with coronary heart diseases (CHD) in Scotland (Douglas *et al*., 1995). These authors showed that the dominant May increase in CHD is a predominantly male phenomenon and replaced in the older male age group (> 75 years) by a bimodal pattern (Douglas *et al*., 1995). These conclusions are consistent with our results (see Figure 3A, B). Therefore, to our mind, the cause of the age related May peak in male CVD deaths seems to have no relation to geomagnetic activity. Douglas *et al*. (1995) suggested that

the male, age related May maximum in CHD was caused by emotional and physical effects of increased hormones in spring in men having cardiovascular disorder. Note that Mikkola *et al*. (2013) showed that there were sex-related differences in CVD mortality.

Thus the contribution of geomagnetic activity to the distribution of CVD deaths seems to be real, but not significant, socioeconomic factors being predominant. This confirms our previous studies, where it was shown that only in 15% of cases, geomagnetic activity had an adverse effect on the intrauterine development of the fetus at high latitudes (Shumilov *et al*., 2003). The influence of geomagnetic disturbances is predominant on female and older male (>70 years) CVD deaths.

Electromagnetic emissions (EME) are considered as the most probable cosmophysical factors that influence the human organism. Some studies suggest as a critical factor that affects the human cardiovascular system are geomagnetic micropulsations Pc1 and Pi1 having a frequency (0.2 – 5 Hz) comparable with the frequency of heart rate beatings (Kleimenova *et al*., 2007; Samsonov *et al*., 2014). Geomagnetic pulsations Pc1 are connected with geomagnetic storms and demonstrate a winter maximum in their occurrence (Kleimenova *et al*., 2007). In turn, micropulsations Pi1 are observed at high latitudes during geomagnetic substorms and seem to have a bimodal pattern with two equinoctial maxima in their seasonal distribution (Samsonov *et al*., 2014). So, the appearance of additional equinoctial maxima in the CVD death occurrence at high latitudes may be explained by the influence of micropulsations Pi1 on the heart rhythm (see Figure 3). Nearly similar seasonal pattern with multiple peaks was found in the ambulance calls for myocardial infarction in Yakutsk (subauroral latitudes) (Samsonov *et al*., 2014). Synchronization of rhythms of the heart with geomagnetic field variations can occur taking into account that the human organism is an open non-linear system being in the state of non-stable dynamic balance (Kleimenova *et al*., 2007; Breus *et al*., 2008; Samsonov *et al*., 2014).

Another important property of EME, found experimentally, is its capability of affecting the secretion of melatonin – one of the main hormones (the hormone of pineal gland or epiphysis) (Weydahl *et al*., 2001). Melatonin is one of the most important regulators of the immune system and biological rhythms in animals and men acting as a free radicals absorber and an antioxidant in organism (Cherry, 2002). It was shown that at high latitudes the geomagnetic disturbances, with a well manifested daily course, perform the part of an exterior synchronizer of biological processes in human organism by affecting the melatonin production (Weydahl *et al*., 2001).

Note that our results showed no significant association between air pollution and CVD mortality (see Figure 4). This does not contradict to other studies where the main pollutants affecting the cardiovascular diseases and mortality are fine particles and SO_2 (Dockery, 2001; Lin *et al*., 2004). Most of these results were obtained exclusively for highly urbanized regions (Dockery, 2001; Lin *et al*., 2004).

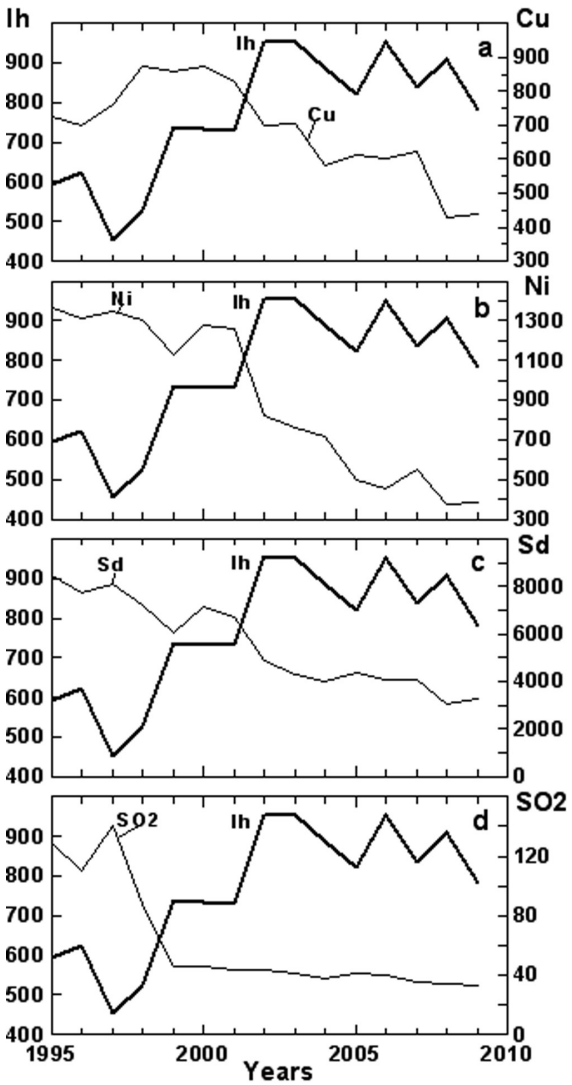

Figure 4. Variations of CVD mortality rates *Ih* at Kirovsk (curve 1) and emissions of atmospheric pollutants by "Severonikel" plant (curve 2): Cu (tons/year) (a), Ni (tons/year) (b), fine particles Sd (tons/year) and SO_2 (thousands tons/year).

Conclusions

1. A sharp increase has been observed in CVD death occurrence in Kirovsk since 1991 (more than twice compared to the period of 1948-1990), which, more likely, was connected to socio-economic stresses during that period in Russia. Some reduction of CVD mortality rate in the period of 1985 – 1991 seemed to be caused by some effects of the anti-alcohol campaign, however it was not significant compared with other variations.

2. Our analysis revealed significant differences in seasonal distributions of CVD mortality depending on sex and age groups and their response to external geomagnetic disturbances. The influence of geomagnetic disturbances is predominant in female and older male (>70 years) CVD deaths. The cause of the age related May peak in male CVD deaths seems to have no relation to geomagnetic activity being explained by emotional and physical effects of increased hormones of men during spring time.

3. MTM-spectral analysis of the distribution of CVD death events in Kirovsk revealed periodicity of ~9-10 years attributed to the solar cycle. The periods of ~4.7 years and ~2.3 years are rather well correlating with similar periodic variations in geomagnetic aa-indexes.

4. The contribution of geomagnetic activity to the variations of CVD death rate seems to be real, but not significant, socioeconomic factors are predominant.

5. Our results demonstrated no significant association between air pollution and CVD mortality in the region.

References

Breus T., Ozheredov V.A., Syutkina E.V., Rogoza A.N., 2008, Some aspects of the biological effects of space weather. *J. Atmos. Solar-Terr. Phys., 70*, 436-441.

Cherry N., 2002, Schumann resonances, a plausible biophysical mechanism for the human health effect of solar/geomagnetic activity. *Nat. Hazards, 26*, 279-331.

Cornelissen G., Halberg F., Breus T., Syutkina E.V., Baevsky R., Weydahl A., Watanabe Y., Kuniaki O., Siegelova J., Fiser B., Bakken E.E., 2002, Non-photic solar associations of heart rate variability and myocardial infarction. *J. Atmos. Solar- Terr. Phys., 64*, 707-720.

Diaz-Sandoval R., Erdelyi R., Maheswaran R., 2011, Could periodic patterns in human mortality be sensitive to solar activity? *Ann. Geophys., 29*, 1113-1120.

Dockery D.W., 2001, Epidemiologic evidence of cardiovascular effects of particulate air pollution. *Environ. Health Perspect., 109*, 483-486.

Douglas A.S., Rawles J., 1999, Latitude-related changes in the amplitude of annual mortality rhythm. The biological equator in Man. *Chronobiol. Int., 16*, 199-212.

Douglas A.S., Dunningan M.G., Allan T.M., Rawles J.M., 1995, Seasonal variation in coronary heart disease in Scotland. *J. Epidemiol. Comm. Health, 49*, 575-582.

Ghil M., Allen R.M., Dettinger M.D., Ide K., Kondrashov D., Mann M.E., Robertson A.W., Saunders A., Tian Y., Varadi F., Yiou P., 2002, Advanced spectral methods for climatic time series. *Rev. Geophys., 40*, 3.1-3.41.

Gonzalez A.L.C., Silbergleit V.M., Gonzalez W.D., Tsurutani B.T., 2002, Irregularities in the semiannual variation of the geomagnetic activity. *Adv. Space Res., 30*, 2215-2218.

Halberg F., Cornelissen G., Otsuka K., Watanabe Y., Katinas G.S., Burioka N., Delyukov A., Gorgo Y., Zhao Z., Weydahl A., Sothern R.B., Siegelova J., Fiser B., Dusek J., Syutkina E.V., Perfetto F., Tarquini R., Singh R.B., Rhees B., Lofstrom D., Lofstrom P., Johnson P.W., Schwartzkopff O., 2000, Cross-spectrally coherent ~10.5- and 21-year biological and physical cycles, magnetic storms and myocardial infarctions. *Neuroendocrinol. Lett., 21*, 233-258.

Healy J.D., 2003, Excess winter mortality in Europe: a cross country analysis identifying key risk factors. *J. Epidemiol. Community Health, 57*, 784-789.

Karnachev I.P., Kokljanov E.B., Zagvozdina O.I., 2001, Harakteristika ustoichivogo razvitija v prirodoohrannoj i trudoohrannoj sferah dejateljnosti predprijatij Koljskogo Severa pri osvoeniji mineraljno-syrjevyh resursov regiona. (Characteristics of sustainable development in environmental and industrial areas of Kola Peninsula under the development of mineral resources in the region). *Proceedings of the MSTU, 14*, 743-750.

Kleimenova N.G., Kozyreva O.V., Breus T.K., Rapoport S.I., 2007, Seasonal variations of myocardial infarction and possible effects of geomagnetic micropulsations on the cardiovascular system in humans. *Biofizika, 52*, 1112-1119.

Lin C.A, Pereira L.A.A., Nishioka D.C., Conceicao G.M., Braga A.L., Saldiva P.H., 2004, Air pollution and neonatal deaths in San Paolo. *Braz. J. Med. Biol. Res., 37*, 765-770.

Marti-Soler H., Gubelman C., Aeschbacher S., Alves L., Bobak M., Bongard V., Clays E., de Gaetano G., Castelnuovo A., Elosua R., Ferrieres J., Guessous I., Igland J., Jorgensen T., Nikitin Y., O'Doherty M.G., Palmieri L., Ramos R., Sulo G., Vanuzzo D., Vila J., Barros H., Borglykke A., Conen D., Bacquer D., Donfrancesco C., Gaspoz J.-M., Giampaoli S., Giles G.G., Iacoveillo L., Kee F., Kubinova R., Malyutina S., Marrugat J., Prescott E., Ruidavets J.B., Scragg R., Simons L.A., Tamosiunas A., Tell G.S., Vollenweider P., Marques-Vidal P., 2014, Seasonality of cardiovascular risk factors: an analysis including over 230000 participants in 15 countries. *Heart, 100*, 1517-1523.

Mendoza B. and de la Pena, S.S.: Solar activity and human health at middle and low geomagnetic latitudes in Central America, Adv. *Space Res*., 46, 4, 449-459, 2010.

Mendoza B., Diaz-Sandoval R., 2000, Relationship between solar activity and myocardial infarctions in Mexico City. *Geofisica Internacional, 39,* 1-4.

Mikkola T.S., Gissler M., Merikukka M., Tuomikoski P., Ylikorkala O., 2013, Sex differences in age-related cardiovascular mortality. *Plos One, 8,* e63347, doi: 10.1371/journal.pone.0063347.

Norstrom, T., 2011, The role of alcohol in the Russian mortality crisis. *Addiction, 106*, 1957-1965.

Palmer S.J., Rycroft M.J., Cermack M., 2006, Solar and geomagnetic activity, extremely low frequency magnetic and electric fields and human health at the Earth's surface. *Surv. Geophys., 27*, 557-595.

Pujades-Rodriguez M., Timmis A., Stogiannis D., Rapsomaniki E., Denaxas S., Shah A., Feder G., Kivimaki M., Hemingway H., 2014, Socioeconomic deprivation and the incidence of 12 cardiovascular diseases in 1.9 million women and men: Implications for risk prediction and prevention. *Plos One, 9*, e104671, doi: 10.1371/journal.pone.0104671.

Russel C.T., McPherron R.L., 1973, Semiannual variation of geomagnetic activity. *J. Geophys. Res., 78*, 92-108.

Samsonov S.N., Kleimenova N.G., Kozyreva O.V., Petrova, P.G., 2014, The effect of space weather on human heart diseases in subauroral latitudes. *Izvestiya, Atmospheric and Oceanic Physics, 50*, 719-727

Shkolnikov V.M., Cornia G.A., Leon D.A., Mesle F., 1998, Causes of the Russian mortality crisis: evidence and interpretations. *World Development, 26*, 1995-2011.

Shumilov O.I., Kasatkina E.A., Raspopov O.M., 1998, Heliogeomagnetic activity and extreme situations in the zone of polar cap. *Biofizika, 43*, 670-676.

Shumilov O.I., Kasatkina E.A., Enikeev A.V., Khramov A.A., 2003, A study of the effect of geomagnetic disturbances in high latitudes on the intrauterine condition of fetus by the method of cardiomonitoring. *Biofizika, 48*, 374-379.

Shumilov O.I., Kasatkina E.A., Novikova T.B., Sutinen M.L., Chramov A.V., Enykeev A.V., 2014, Natural and man-made influences on suicides in northwestern Russia. *Nat. Hazards, 73*, 439-448.

Stoupel E., Abramson E., Sulkes J., Martfel J., Stein N., Handelman M., Shimshoni M., Zadka P., Gabbay U., 1995, Relationship between suicide and myocardial infarction with regard to changing physical environmental conditions. *Int. J. Biomet., 38*, 199-203.

Thomson D.J., 1982, Spectrum estimation and harmonic analysis. *IEEE Proc., 70*, 1055-1067.

Villoresi G., Breus T.K., Iucci N., Dorman L.I., Rapoport S.I., 1994a, The influence of geophysical and social effects on the incidences of clinically important pathologies (Moscow 1979-1981). *Physica Medica, 10*, 79-91.

Villorezi G., Kopytenko Y.A., Ptitsyna N.G., Tyasto M.I., Kopytenko E.A., Iucci N., Voronov P.M., 1994b, The influence of geomagnetic storms and man-made magnetic field disturbances on the incidence of myocardial infarction in St Petersburg (Russia). *Physica Medica, 10*, 107-117.

Weydahl A., Sothern R.B., Cornelissen G., Wetterberg L., 2001, Geomagnetic activity influences the melatonin secretion at latitude 70°N. *Biomedicine and Pharmacotherapy, 55*, 57-62.

World Health Organization. The European Health Report 2012: Charting the way to well-being. Geneva: World Health Organization Press, 2013.

Geofísica Internacional (2016) 55-4: 275-291

Original paper

Numerical simulation of multiple scattering of P and SV waves caused by near-surface parallel cracks

Rafael Ávila-Carrera*, Alejandro Rodríguez-Castellanos, Celestino Valle-Molina, Francisco José Sánchez-Sesma, Francisco Luzón and Ernesto González-Flores

Received: January 18, 2016; accepted: August 09, 2016; published on line: October 01, 2016

DOI: 10.19155/geofint.2016.055.4.5

Resumen

En este trabajo se investiga la difracción y dispersión de ondas P y SV por la presencia de grietas orientadas paralelamente localizadas cerca de una superficie libre. Se utiliza el Método Indirecto de Elementos de Frontera (IBEM) para estudiar el fenómeno de propagación de onda en un modelo con semi-espacio plano que contiene grietas. Se consideran varios ángulos de incidencia de ondas P y SV. Ya antes ha sido reportado en la literatura especializada que una grieta cercana a la superficie libre genera ondas superficiales difractadas cuyos espectros de amplitudes muestran picos de resonancia muy pronunciados. Tal efecto ha sido atribuido a resonancias locales de un estrato virtual entre la cara superior de la grieta y la superficie libre. Para nuestro caso de dos grietas paralelas cercanas a la superficie libre, los espectros de amplitudes muestran picos adicionales que pueden asociarse con la presencia de la segunda grieta. Si las grietas son de tamaño similar, la frecuencia característica de resonancia medida en la superficie libre corresponde principalmente al estrato equivalente formado por la grieta más somera y la superficie libre. Sin embargo, cuando la grieta más profunda llega a ser suficientemente larga con respecto a la grieta más somera, aparecen dos picos de frecuencias características de resonancias en los espectros medidos en la superficie. Nuestro trabajo también muestra ejemplos con sistemas de tres grietas. Esto ha resultado en una tarea intrincada, sobre todo en la identificación y caracterización de la respuesta sísmica del campo difractado generado por la segunda y tercera grietas y por su parte, la interpretación en el dominio del tiempo de las trazas obtenidas se vuelve bastante complicada. Los resultados en este trabajo han sido validados contra otros reportados en artículos clásicos. Con objeto de ilustrar la respuesta sísmica y los efectos de difracción múltiple debido a la presencia de sistemas de grietas, se proveen cálculos en el dominio del tiempo y la frecuencia.

Palabras clave: Modelo de propagación de onda, grietas cercanas a la superficie, respuesta sísmica.

R. Ávila-Carrera*
A. Rodríguez-Castellanos
C. Valle-Molina
E. González-Flores
Instituto Mexicano del Petróleo
Eje Central Lázaro Cárdenas 152
Gustavo A. Madero 07730
México CDMX, México
*Corresponding author: rcarrer@imp.mx

F. J. Sánchez-Sesma
Instituto de Ingeniería
Universidad Nacional Autónoma de México
Ciudad Universitaria
Delegación Coyoacán 04510
México CDMX, México

F. Luzón
Departamento de Física Aplicada
Universidad de Almería
Cañada de San Urbano s/n, 04120
Almería, Spain

Abstract

Scattering and diffraction of P and SV waves caused by parallel oriented cracks located near to a free surface are investigated in this work. The Indirect Boundary Element Method (IBEM) was applied for studying the wave propagation phenomena in a half-plane model that contain the cracks. Various incidence angles of P and SV waves are considered. Sometime before it has been reported that a near free-surface crack generates scattered surface waves whose amplitude spectra show conspicuous resonance peaks. Such effect has been attributed to local resonances originated in a virtual layer between the shallowest crack and the free surface. For our case of two parallel crack system, where cracks are located at different depths, the amplitude spectra show additional peaks, which can be associated with the presence of the second crack. Given similar sizes between these two cracks, the characteristic resonance frequency observed at the free surface corresponds mainly to the equivalent layer formed by the shallowest crack and the free surface. However, when the deepest crack becomes sufficiently large with respect to the shallow crack, two resonance characteristic frequency peaks appear in the measured spectra at the free surface. Some examples including a three crack system are also illustrated in our work. The identification and characterization of the seismic response for the scattered field generated by the second and third crack has been an intricate task and, the time domain interpretation of traces becomes quite complicated. The results in this paper have been validated against some other reported from classic papers. In order to show the seismic response and multiple scattering effects due to the presence of systems of cracks, calculations in frequency and time domain are provided.

Key words: wave propagation model; near surface cracks; seismic response.

Introduction

The solution of the inverse problems involved in the detection and characterization of cracks, given a scattered wave field, have represented significant technical challenges for executing non-destructive evaluations. In shale gas/oil reservoirs, aligned fractures and cracks are the main cause of rock anisotropy. The presence of cracks may generate a scattered wave field that contains essential amount of information about the geometry, size and depth of the cracks. Therefore, some areas of knowledge such as engineering, seismology and geophysics have had a considerable interest in studying scattered wave fields caused by sub-surface cracks over the past century (Mendelsohn *et al*., 1980; Brind and Achenbach, 1981; Achenbach and Brind, 1981). However, recent works indicate that the study of modifications in the wave propagation phenomena caused by cracks and fractures is still an important issue in physical sciences (Yang *et al*., 2008; Dineva *et al*., 2006, Rodríguez-Castellanos *et al*., 2007 and Ávila-Carrera *et. al*., 2009). In the case of near-surface cracks, it has been observed significant wave interaction between the free-boundary and discontinuities in the media, and valuable information is obtained by means of frequency analyses (Achenbach *et al*., 1983; Keer *et al.*, 1984).

Multiple scattering by cracks was studied extensively during early 90's. The applications were essentially bidimensional analyses (2D) for cross-hole surveys as reported in Liu *et al.,* (1989, 1991 and 1993). The analysis of field data encouraged the authors to determine the overall elastic properties of cracked rocks. The objective was to formulate effective medium expressions for elastic wave propagation models where the wavelengths are greater than the dimensions of the considered discontinuities. Consequently, a set of poro-elastic models was developed that include interconnected and non-interconnected cracks and voids (Hudson *et al*., 1996; Pointer *et al.,* 2000; Brajanovski *et al*., 2005). The impact of fractal distribution of cracks, inclusions and cavities has been also covered in the context of nearly realistic average of properties (Liu *et al*., 1999; Liu *et al*., 2000; Liu and Zhang, 2001; Tod *et al.,* 2002; Rao and Prasanna, 2006; Sherman *et al.*, 2013).

The three-dimensional modeling of wave scattering phenomena, caused by a single crack using Kirchhoff's approximation in the high frequency domain, allows now to determine the sizes and shapes of the cracks (Liu *et al*., 1997). The main purpose of the homogenization methods is to determine effective properties of elastic media containing

scattering with different shapes, random orientations and distributions. Generally, the analytical representations of the cracked-systems by means of their effective properties predicts very well the body wave velocities, in comparison with reported velocities measured in laboratory. In contrast, the application of the homogenization methods to describe the seismic response of complex fractured or heterogeneous media in both, high and medium frequencies regimes, has not been significantly studied. On the other hand, 2-D and 3-D seismic wave propagation simulations for a single, or multiple-scattering by different obstacles at intermediate frequencies, is currently a research topic.

The main aim of this article is to present the findings related to the identification and descriptions of the wave propagation phenomena through simple crack systems. Investigations of the seismic response and important alterations on the scattered fields provoked by cracks located near to a free surface of a media, were also conducted. Descriptions of different wave-crack interactions for shallow parallel-crack patterns might be meaningful to several engineering and seismology areas. It is likely that specialists working on evaluation of seismic field amplifications for earthquake site response, interpretation of full waveforms in borehole sonic logs (Ávila-Carrera *et al.,* 2011) or deviations of seismic energy in exploration of hydrocarbon reservoirs could be interested in the results of this numerical research.

In this work, the scattered displacement field generated by both single or multiple near-surface-parallel cracks in a half space under plane incidence of P or SV waves is presented. The Indirect Boundary Element Method (IBEM) was used to simulate the multiple scattering problem addressed in this work. This method is based on an integral representation of the scattered displacement field in terms of single-layer boundary sources, which are derived from Somigliana´s identity. The total displacement field in the cracked half space is calculated by adding both, the specified incident field (e.g. P- or SV-waves) in the non-cracked or intact half space, and the scattered field in the cracked media generated by suitable surface traction conditions over the free surface and the cracks faces.

In the case of a single crack oriented parallel to the free surface, our results are in good agreement with similar results reported by Achenbach *et al*. (1983). Otherwise, for a two- crack system, the classic solution provided by Achenbach *et al*. (1983) is not applicable due to constrains of the formulation. Therefore, we took advantage of the integral formulation to solve local interactions between scattered fields from the cracks and the free surface. The results give evidence that multiple cracks generate important alterations in the total displacement field for points placed at the free surface. Additional resonance peaks are generated and identified in the frequency domain by the presence of the second crack and its impact appears to be greater depending on the ratio length to the depth of the shallowest crack.

In addition, calculations of time histories and synthetic seismograms for a system of three cracks shows complex scattering patterns that become quite difficult to interpret. Finally, the computation of snapshots reveals that the wave field modifications caused by the deepest crack are undetectable, unless its relative length with respect to the shallower cracks is several times larger.

Description of the method

A finite or infinite continuous surface *S* could be considered in the two-dimensional Euclidean space. If the space is constituted by an elastic material, the field of displacements caused by harmonic excitation can be written, neglecting body forces, by means of the single-layer boundary integral equation:

$$u_i(x) = \int_S \phi_j(\xi) G_{ij}(x;\xi) dS_\xi \qquad (1)$$

where: $u_i(x)$ is the ith component of the displacement at point x; $G_{ij}(x;\ \xi)$ denotes the Green's function representing displacements produced along the i direction at x that are caused by applying a unitary force in direction j at point ξ; and $\phi_j(\xi)$ is the force density in the j direction at point ξ.

The product $\phi_j(\xi)dS_\xi$ represents a distribution of forces on the surface S. The sub-index in the differential operator denotes the variable on which the integration is carried out. This integral representation could be solved using the Somigliana's identity (Sánchez–Sesma and Campillo, 1991). Moreover, it has been probed that if $\phi_j(\xi)$ is continuous along S, then the field of displacements is continuous across S (Kupradze, 1963).

This integral representation allows the calculation of stresses and tractions by

directly applying the Hooke's law and Cauchy's equation, except for the case when x is equal to ξ on surface S that correspond to the boundary singularities. From a limiting process based on equilibrium considerations around an internal neighborhood of the boundaries and interfaces on which respective conditions are imposed, it is possible to write, for x on S,

$$t_i(x) = c\phi_i(x) + \int_S \phi_j(\xi) T_{ij}(x;\xi) dS_\xi \quad (2)$$

where: $t_i(x)$ is the ith component of traction, c=0.5 if x tends to the boundary S from the interior of the region, c=−0.5 if the variable x approaches to S from outside of the region, or c=0 if x is not at S. $T_{ij}(x; \xi)$ represents the traction from the Green's function, which means the traction in the i direction at a point x due to the application of a unit force in the j direction at ξ on S. Green's function for displacements and tractions are presented in Sánchez–Sesma and Campillo, (1991).

The configuration of the problem is depicted in Figure 1 in a Cartesian plane defined with axis X_1 (abscissas) and axis X_3 (ordinates) and the origin is located at the free surface. In this model, two parallel cracks are considered in the media at different depths. The crack 1 is the shallowest at a depth *d,* while the depth between crack 1 and 2 is equal to *c*. The total length of crack 1 is 2*a* and crack 2 has a length of 2*b*. It is easy to note that the cracks are centered with respect to axis X_3. Both, P and SV waves propagate towards the free surface with an angle of incidence γ. Finally, points A and B represent locations of interest for the numerical analyses at a distance e from axis X_3. Point A is positioned at the free surface level and point B is at the same depth of crack 1. Figure 2 shows the domain of the media and the boundary conditions of the problem and it is observed that the domain is divided in two regions (R and E). The boundary conditions for the domain regions are: $\partial R=\partial_1 R \cup \partial_2 R \cup \partial_3 R$ for region R and $\partial E=\partial_1 E \cup \partial_2 E$ for region E.

Boundary conditions

According to Figure 2, the traction-free boundary condition is considered at the free surface ($\partial_3 R$), then this can be represented by writing:

$$t_i^R(x) = 0, \quad x \in \partial_3 R \quad (3)$$

On the other hand, the interface zone between region R and E exhibit continuity of displacements and tractions that can be established as:

$$u_i^R(x) = u_i^E(x), \quad x \in \partial_1 R = \partial_1 E \quad (4)$$

$$t_i^R(x) = t_i^E(x), \quad x \in \partial_1 R = \partial_1 E \quad (5)$$

Also, the tractions are null along the cracks and therefore we have:

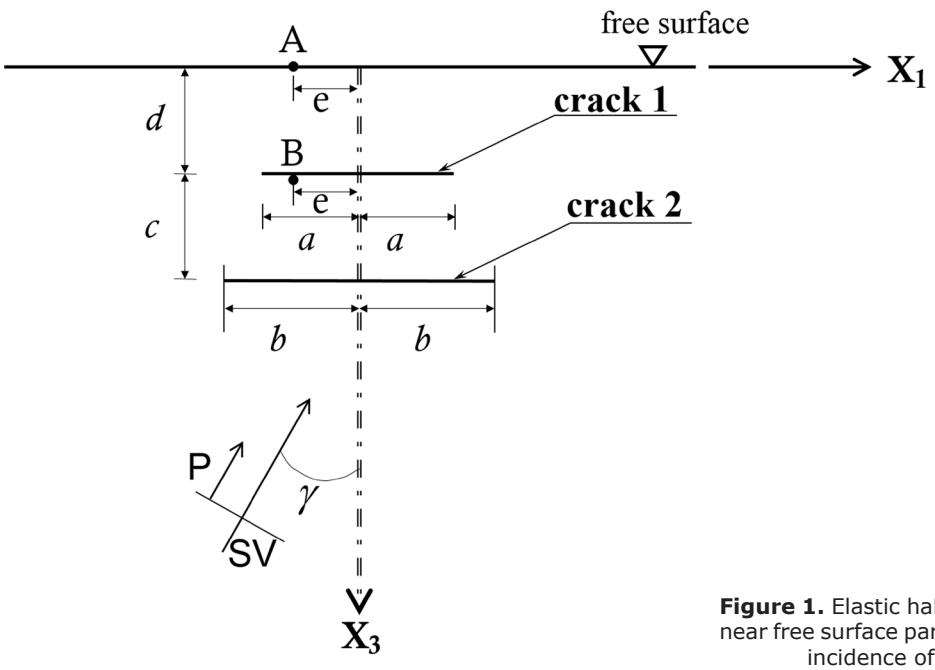

Figure 1. Elastic half-space that contains two near free surface parallel cracks excited by the incidence of P and SV waves.

$$t_i^E(x) = 0, \quad x \in \partial_2 E \tag{6}$$

and

$$t_i^R(x) = 0, \quad x \in \partial_2 R \tag{7}$$

Tractions and displacements on each region E and R can be estimated taking into account the contribution of the results in the free-field (results of the analytical solution of the half-space without cracks) adding the results of the diffracted field, then the equations (3) to (7) can be expressed as:

$$t_i^R(x) = t_i^{o^R}(x) + t_i^{d^R}(x) = 0, \quad x \in \partial_3 R \tag{8}$$

$$u_i^{d^R}(x) + u_i^{o^R}(x) = u_i^{d^E}(x) + u_i^{o^E}(x), \quad x \in \partial_1 R = \partial_1 E \tag{9}$$

$$t_i^{d^R}(x) + t_i^{o^R}(x) = t_i^{d^E}(x) + t_i^{o^E}(x), \quad x \in \partial_1 R = \partial_1 E \tag{10}$$

$$t_i^E(x) + t_i^{o^E}(x) = t_i^{d^E}(x) = 0 \quad x \in \partial_2 E \tag{11}$$

$$t_i^R(x) + t_i^{o^R}(x) + t_i^{d^R}(x) = 0 \quad x \in \partial_2 R \tag{12}$$

It is important to note that super-index o stands for the free field region, while super index d identifies the diffracted one. Now, using the integral representations of equations (1) for displacements and (2) for tractions, the equations from (8) to (12) can be expressed as:

$$\int_{\partial R} \phi_j^R(\xi) G_{ij}^R(x;\xi) dS_\xi - \int_{\partial R} \phi_j^E(\xi) G_{ij}^E(x;\xi) dS_\xi = u_i^{o^E}(x) - u_i^{o^R}, \quad x \in \partial_3 R \tag{13}$$

$$\int_{\partial R} \phi_j^R(\xi) G_{ij}^R(x;\xi) dS_\xi - \int_{\partial R} \phi_j^E(\xi) G_{ij}^E(x;\xi) dS_\xi = u_i^{o^E}(x) - u_i^{o^R}(x), \quad x \in \partial_1 R = \partial_1 E \tag{14}$$

$$c\phi_i^R(x) + \int_{\partial R} \phi_j^R(\xi) T_{ij}^R(x;\xi) dS_\xi - c\phi_i^E(x) - \int_{\partial E} \phi_j^E(\xi) T_{ij}^E(x;\xi) dS_\xi = t_i^{o^E}(x) - t_i^{o^R}(x), \quad x \in \partial_1 R = \partial_1 E \tag{15}$$

$$c\phi_i^E(x) + \int_{\partial E} \phi_j^E(\xi) T_{ij}^E(x;\xi) dS_\xi = -t_i^{o^E}(x), \quad x \in \partial_2 E \tag{16}$$

$$c\phi_i^R(x) + \int_{\partial R} \phi_j^R(\xi) T_{ij}^R(x;\xi) dS_\xi = -t_i^{o^R}(x), \quad x \in \partial_2 R \tag{17}$$

In order to solve numerically the system of integral equations constituted by equations (13) to (17), it is required to discretize them. It is assumed that $\phi_i^{R,E}(\xi)$ is constant in each element of the surfaces, which lead to a system of linear integral equations, where $\phi_i^{R,E}(\xi)$ are unknown. Then, the unknown $\phi_i^{R,E}(\xi)$ are obtained and used in the integral representation indicated by equations (1) and (2), and the complete displacement and traction values (in the diffracted and free fields) are determined at any point in the two-dimensional Euclidean space.

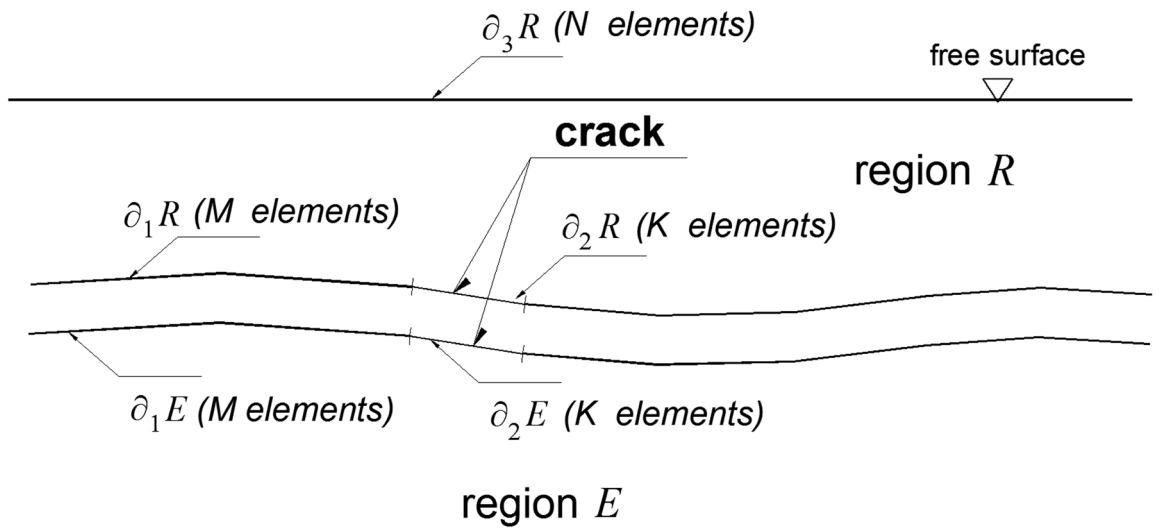

Figure 2. Configuration by regions R and E of the elastic half-space. The free surface is discretized in *N elements*, the crack in *K elements*, and the common interface among R and E in *M elements*.

In the IBEM formulation, we take advantage of the multiregion concept. Therefore, the elastic space is divided into two media. From this criterion, a virtual boundary emerges, which represents the continuity of tractions and displacements between the regions R and E (see $\partial_1 R$ and $\partial_1 E$ in Figure 2). The other boundary corresponds to the crack face, for which, traction free boundary conditions must be imposed. The virtual boundary should be extended at least $2a$ from the crack tip, this approach usually guarantees good accuracy in the computations.

In this paper, we show essentially the influence of near free surface cracks on the diffracted wave field measured by receivers placed at the free surface. Special boundary elements may be used to model the singularity at the crack tip in order to retrieve fracture mechanics parameters; for example, the Stress Intensity Factor (SIF). However, it has been shown that radiated waves are insensitive to stress concentrations. As shown here, the use of constant elements has been enough for the studied frequencies. Our results at the free surface evince very good agreement with those obtained by Achenbach *et al*. (1983).

Numerical results

In this section, numerical results obtained with IBEM on various sets of cracks systems are exhibited. The analysis of elastic wave propagation in the intact, bi-crack and triple-crack models of Figures 1 and 2 are presented. In this work, all the boundaries and interfaces are discretized into boundary elements. Three-hundred boundary elements are used for the validation case (K = 50, M = 100 and N = 150, for the maximum frequency calculated). For the extreme case of b/a=2, K = 100, M = 150 and N = 150 boundary elements are required. For all calculations, we consider 6-boundary elements per minimum wavelength and within each element Gaussian integration of 5 points is used. Section 3.1 reports the horizontal and vertical displacements changing with frequency for different crack configurations. In addition, Section 3.2 shows the wave propagation patterns in the mono-cracked and bi-cracked media by snapshots of the displacement field. Finally, Section 3.3 presents the synthetic seismograms associated with three-cracked media.

Results in frequency domain

The results obtained in this work were initially compared with those similar previously published by Achenbach *et al.* (1983) as presented in Figure 3. In this sense, the results correspond to a medium with a single crack excited by means of a P-wave with normal incidence. The elastic properties of the medium are: Poisson's ratio v=0.3, S-wave velocity β=100m/sec, four different ratios ($d/2a$) of normalized depth $d/2a$ =0.2 0.4, 0.6 and 1.0. For all cases, d is equal to the depth of crack 1 measured from the free surface and a=100m, stands for its length.

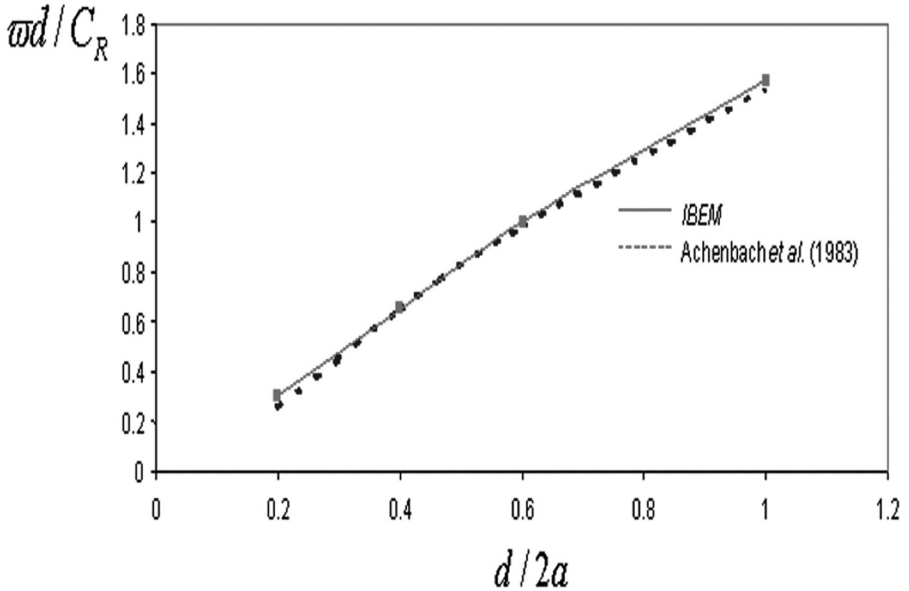

Figure 3. Curve that relates resonance frequency $\varpi d/C_R$ and $d/2a$. Continuous line represents the results obtained by our method. Dashed line represents those obtained by Achenbach *et al*. (1983).

Figure 3 shows the dimensionless resonance frequencies ($\frac{\omega d}{C_R}$) varying with ratio $d/2a$, where ϖ is the resonance frequency and C_R represents the Rayleigh's wave velocity. It is remarkable the good agreement between IBEM results with the results reported by Achenbach *et al*., (1983). As seen, the dimensionless frequency augments from about 0.3 to 1.6 as the normalized depth increases from 0.2 to 1.

Once the validation of our method was accomplished, several numerical examples were executed regarding a medium with two or more shallow parallel cracks subjected to P- or SV-waves incidence. Six case studies were considered to calculate both horizontal $|u|$ and vertical $|w|$ displacements at point A (see Figure 1, where e=0.75a) for vertical and oblique P-wave incidence with γ=0° and γ=30°, respectively. Results presented in Figure 4a and b correspond to normal incidence of P-waves. These cases are related to ratios b/a=0, 0.25, 0.75, 1.00, 1.50 and 2.00 (crack 1 is placed at $d/2a$=0.2 and c=d). The case when b/a=0 means that the crack 2 does not exist.

In Figure 4a, the magnitude of horizontal displacements $|u|$ at point A varying with the dimensionless frequency $\frac{\omega d}{C_R}$ are displayed. The maximum spectral amplitude of the single crack case, match very well with the spectral amplitudes of all ratios b/a≤1.0, which contain 2 cracks. The interpretation of such behavior is: 1) the presence of the second crack, for all ratios below 1.0, does not affect the first resonance frequency and, 2) the equivalent layer placed between the free surface and crack 1, with the direct incidence of the P-wave generates a coupled displacement field at point A. Therefore, it is clear that the diffracted field generated by crack 2 does not create alterations of the displacement field at point A. This zero-effect is particularly characterized when the size of crack 2 is equal or lower than the length of crack 1 and γ=0°. In contrast, also in Figure 4a, we can see that for cases when b/a>1.0 the compressional wave propagation through the zone formed between the free surface and crack 2, generates maximum spectral amplitudes at lower dimensionless frequency in comparison with the case of a single crack. In other words, the presence of crack 2 (when it is bigger than crack 1) generates maximum spectral amplitudes of the system associated with lower frequencies.

It is important to remark that for both ratios, b/a=1.5 and b/a=2.0, the resonance peaks still appear at a dimensional frequency about $\frac{\omega d}{C_R}$=0.30, but with lower amplitude in comparison with those cases related to b/a≤1.0. One possible explanation of the generation of the second peak in the cases b/a=1.5 and b/a=1.5 can be the local resonance in the region between crack 1 and the free surface. Likewise, Figure 4b presents a similar behavior and important amplifications of the vertical displacement field $|w|$ occur for the cases b/a=1.5 and 2.0 at low frequencies. For the two particular cases of Figure 4, additional resonance peaks at non-dimensional frequency about 0.32 are observed. However, the group of resonance peaks are almost imperceptible at the free surface. It is noted that the relative size of crack 2 with respect to the crack 1 size controls the spectral amplification response.

For the homogeneous case, when an incident P wave propagates through intact media (non-cracked) along the normal direction towards the free surface, only vertical displacements are expected. Consequently, there is not any conversion from P to S waves. This means that $|w|$=0 for all frequencies. Otherwise, when the incident compressional wave impacts the cracks, then horizontal displacements are generated (Figure 4a). The conversion of energy from P to S waves is present in the model. In fact, the particle motion determined at point A describes the horizontal component of the displacements caused by the eccentricity e (see Figure 1). It can be observed that there are non-zero amplitude values for all frequencies and for all b/a configurations.

In Figure 4b, a dip to zero of the vertical displacements is observed at a normalized frequency of about 0.35 (for all values of b/a). Among other wave characteristics, for example, creeping, crack-edge-effects or multiple-scattering, this displacement dropping could be attributed to two main facts: 1) there is a change of sign of the vertical displacement field relative to X_3 axis. In other words, the displacement field computed at the free surface is affected by the change of polarization; and 2) it is exhibited that at the normalized frequency of about 0.35, a generalized significant decrement of the amplitudes is given by the interferences and interactions of the P wave travelling up and down in this model. This feature might be considered as a spectral signature of the specific cracked configuration.

The fundamental dimensionless frequency (associated with the first and maximum spectral amplitude) of the system that contains

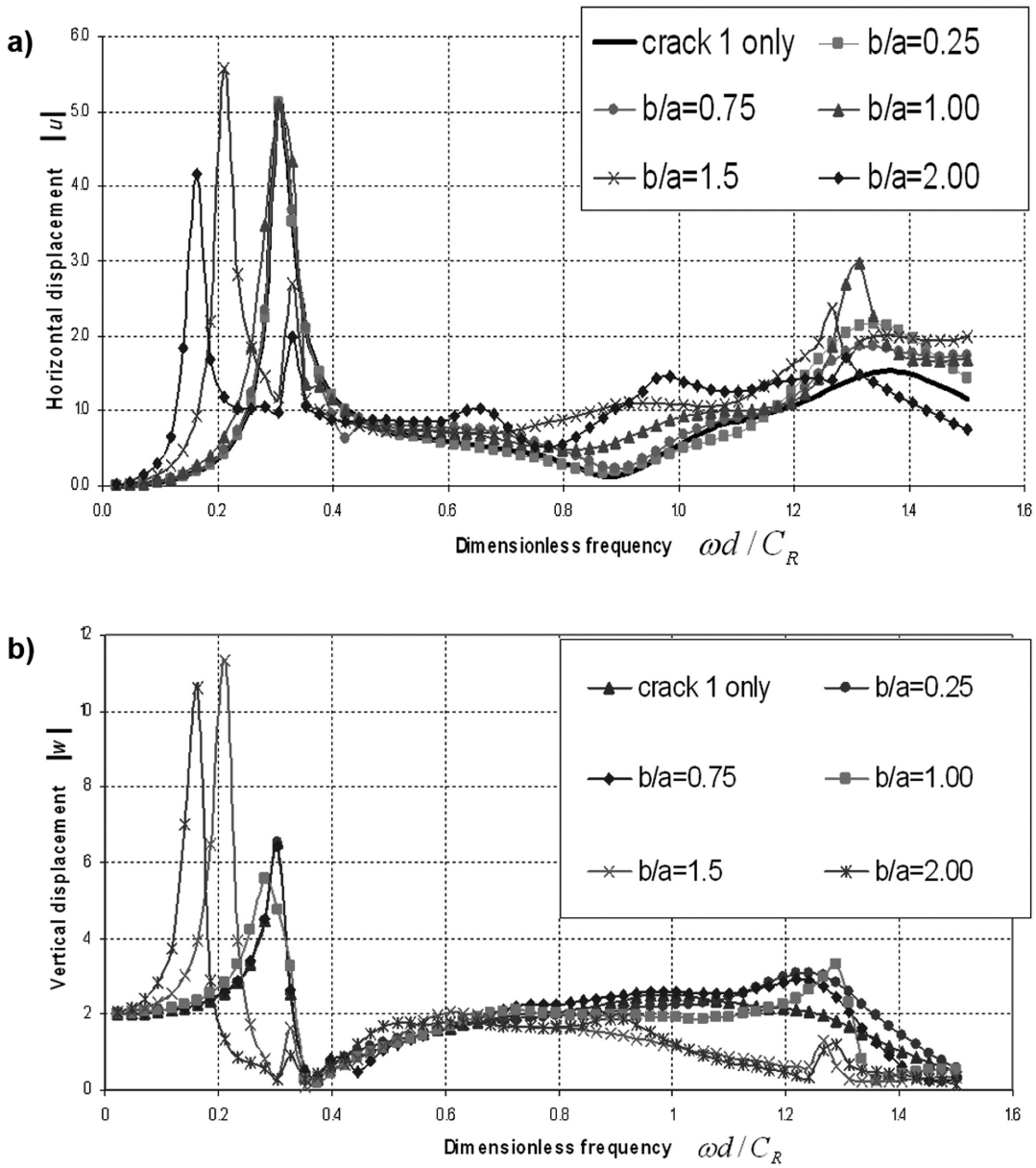

Figure 4. a) Horizontal displacements $|u|$ at point A for six ratios b/a *versus* dimensionless frequency $\omega d/C_R$ with vertical incidence of P waves. For the case of crack 1 only, the results can be expressed as the solution of Achenbach *et al*. (1983). b) Vertical displacements $|w|$ at point A for six ratios b/a *versus* dimensionless frequency $\omega d/C_R$ with vertical incidence of P waves.

two cracks varying with the ratio b/a is depicted in Figure 5. Here, it is possible to see that for the ratios $b/a \leq 1.0$, the resonance frequency of the system is controlled by the equivalent layer between crack 1 and the free surface. This phenomenon is attributed to the relative high compliance exhibited by the single crack system in comparison with the response of the virtual layer formed between crack 2 and the free surface, including crack 1. When the ratio is $b/a > 1.0$, the resonance frequency drops as b increases in comparison with a.

On the other hand, Figure 6 shows the variations of the absolute value of horizontal displacements calculated at points A and B of Figure 1 *versus* the dimensionless frequency. Three incidence angles of the P-wave are considered $\gamma = 0°$, 30° and 60°, the displacements associated with each case are depicted in Figures 6(a), (b) and (c), respectively. It was taken a unique ratio $b/a = 1.0$ for all the cases and points A and B were fixed at $b = 0.75a$. Clearly in all cases, the absolute horizontal displacements at point A are higher than the

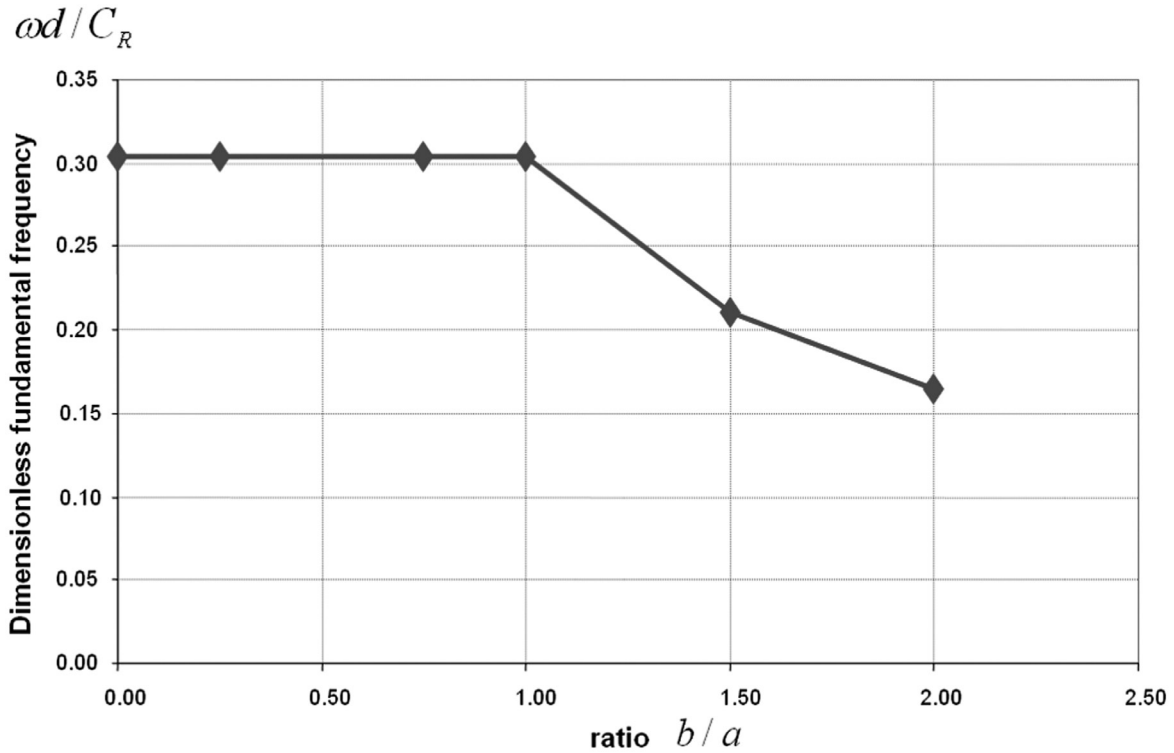

Figure 5. Variation of dimensionless fundamental frequency $\omega d/C_R$ when the ratio b/a increases.

displacements estimated at point B, this fact occurs independently of the angle of incidence. This effect can be interpreted as the maximum spectral ordinate given by the seismic response of the cracked system at the free surface. In addition, two conspicuous resonance peaks in the range $0.2 \leq \frac{\omega d}{C_R} \leq 0.4$ at point B are identified. The first peak could be associated with the local amplification of the fundamental frequency of the cracked system, while the second peak might correspond to the characteristic frequency of the virtual layer placed between crack 1 and crack 2. The second peak might be generated by the stiffness and thickness of the layer between crack 2 and crack 1 and it is almost imperceptible at the free surface, even with the variation of the incident angle. Therefore, if crack 2 is smaller than crack 1, the presence of the second peak might not be detected.

Snapshots of displacements

In order to show similarities and differences of the total diffractions generated by a single crack and two-parallel crack models, snapshots of the vertical displacements $|w|$ for five consecutive times are presented. We have studied the spatial distribution of amplitudes during a lapse of propagation time using meshes 400 x 240 m of evenly spaced receivers. The instant frames of time were obtained by convolution of a Ricker wavelet of t_p=1s and $\lambda_c=a/2$=50m of wavelength, followed by an inverse Fourier transform and then plotted as images. Snapshots are useful to understand by means of visualization, among other physical characteristics, the diffraction and polarization effects of the displacement field, particularly in time domain. In Figure 7 and 8, the snapshots that correspond to the single crack system are depicted in the left section of the figure, while the right portion covers the snapshots of the two-parallel crack system. In all cases, it is important to point out that the free surface is located at the bottom of each snapshot and the incident waves travel toward the free surface. The time increment between each correlative snapshots is 0.52 s. For simulations, a characteristic period of t_p=1s has been selected for the Ricker's incident pulse. Figure 7 shows normal P wave incidence exciting a medium with a single crack (left) and two cracks (right). For both cases, crack 1 is located at $d/2a$=0.2 while crack 2 is at $c=d$ and a ratio of b/a=0.25 is considered. For times t=1.95 and 2.47 s, the incident pulse is clearly seen as a

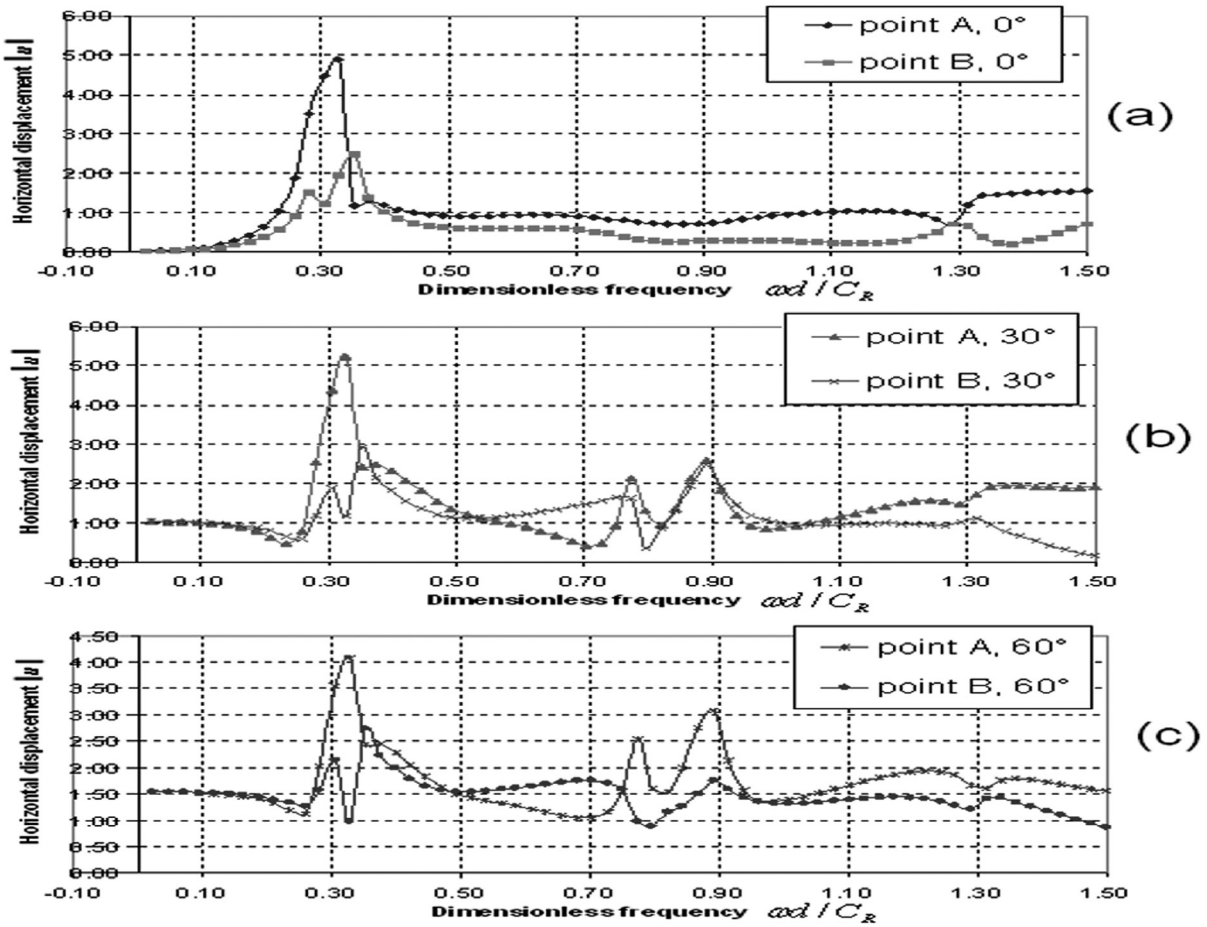

Figure 6 Horizontal displacements measured at points A and B *versus* dimensionless frequency $\omega d/C_R$, for three P waves incidence angles: (a) γ=0°, (b) γ=30° and (c) γ=60°.

lighter and complete bar. In contrast, diffracted wave fields are observed for times from t=2.99 to 4.03 s. A strong diffraction in the interior of the medium is observed at t=3.51 s in the single crack model. Otherwise, a completely different scattering pattern is seen for the case of two cracks, where less number of diffracted waves are produced from the smaller crack. The presence of the shorter crack reduces the wave amplitude of the incident field before it impacts the nearest free surface crack. In this case, despite of single and multiple scattering patterns exhibited at t=3.51 s, the displacement field observed at the free surface for both cases result very comparable. Similarly, the wave propagation patterns observed in Figure 7 were also detected for the oblique incidence of P waves (γ=30°) depicted in Figure 8, in which the displacement fields at the free surface are also controlled by crack 1.

Synthetic seismograms and seismic response

Following the two configurations of the problem depicted in Figure 9, a Cartesian plane was defined through axis X_1 (abscissas) and axis X_3 (ordinates) with the origin located at the free surface. The reference plane is considered to compute synthetic traces by means of the Fourier´s transform. In the synthetic seismograms presented here, a Ricker wavelet with central frequency, ω_c=1/, t_p=1s, t_s=3s s, s is used for all the examples. With the aim of avoiding aliasing effects, a quality factor Q= Q_E =Q_R Q=100 was maintained constant for both, P and SV waves. Such consideration permits the representation of hysteretic damping by using the factor $(1-i/2Q)$ over the dimensionless frequency $\frac{\omega d}{C_R}$ in general, three

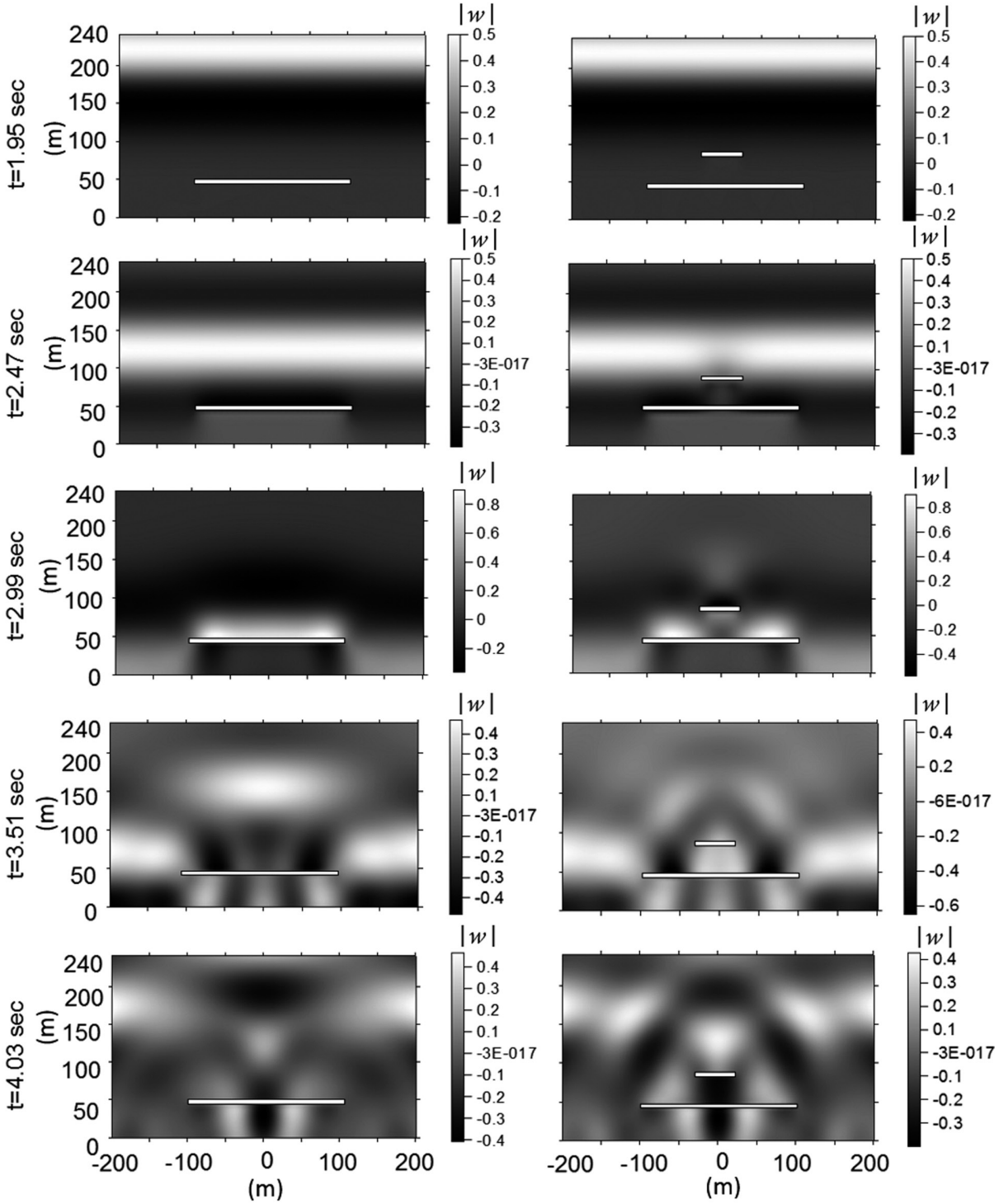

Figure 7. Snapshots representing the wave propagation phenomenon in a medium with cracks. Normalized vertical displacements for the case of a single crack (left) and two cracks (right) excited by a normal P wave incidence are depicted.

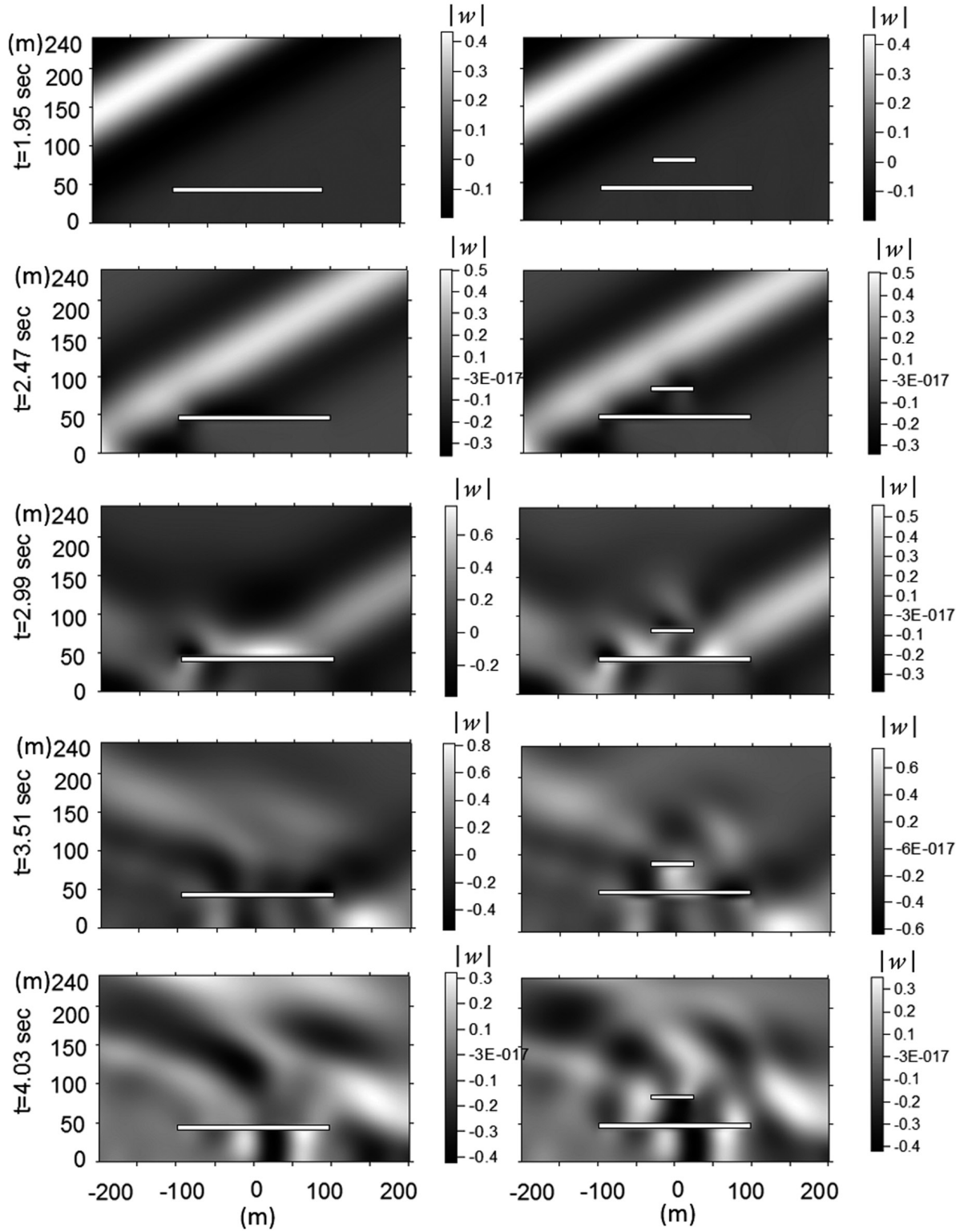

Figure 8. Snapshots representing the wave propagation phenomenon in a medium with cracks. Vertical displacements $|w|$ for the case of a single crack (left) and two cracks (right) excited by an oblique incidence of P wave are displayed.

parallel cracks are included in the media at different depths. Crack 1 is the shallowest at depth d, while depth between crack 1 and 2 is equal to c. The total length of crack 1 is $2a$ and crack 2 has a length of $2b$. The third and deepest crack, has a length of $2g$ with a depth of $d + c + f$ and ratio $d/2g$ =0.6. The cracks are centered with respect to axis X_3. Both, P and SV waves propagate towards the free surface with an angle of incidence γ. Finally, points A and B represent locations of interest for the numerical analyses at a distance e from X_3. Point A is positioned at the free surface level and point B is at the same depth of crack 1.

Figure 10 presents the synthetic seismograms for a case of three parallel cracks from the total displacement field for a row of surface receivers located horizontally ranging from X_1 = - 300 m to X_1 = 300 m. In all time histories, the total duration of the movement is t=8.4 s. The horizontal $|u|$ (Figures 10a and 10b) and vertical $|w|$ (Figures 10c and 10d) normalized components of displacement are shown for two different configurations for normal, γ=0° (left) and oblique, γ=30° (right) incidence of plane P waves. Figures 10a and c correspond to the model of crack 1 with length of a=100m and located at depth $d/2a$=0.2; while crack 2 has b=0.25 a with a depth c + d with $d/2a$=0.4 and $c = d$, and the third and deepest crack, has a length $g = b$ with a depth $d + c + f$, with $d/2g$=0.6 and $f = c = d$ (see Figure 9, Configuration 1). Moreover, configuration 2 is very similar to the first one, except that the deepest crack has a length d=100m. Time histories for this configuration can be seen in Figures 10b and 10d. The main difference between first and second configurations is that g=0.25a for the first one, and $a = b = g$ =100m (three parallel cracks of same lengths) for the second.

The purpose of this analysis is to illustrate how these two different model configurations produce very similar scattering patterns in terms of wave propagation. It is important to point out that basically the same displacement field is obtained at the free surface. Beyond analyses of the displacement field for both configurations and incidence angles, it is noted that both models exhibit very similar diffraction characteristics timewise. Inverse polarization patterns are clearly appreciated in the normalized horizontal $|u|$ displacements for both configurations. A strong delay of 1 s on the original wave front can be directly measured from the seismograms, particularly in those of vertical components (see Figures 10c and d). It can be seen a slightly larger perturbation in the second configuration in comparison with the results of the first configuration, for both incidence angles. However, these small differences in the behavior, do not provide sufficient factual information to define the presence of a second or third crack. We strongly recommend that if relevant information is required about seismic characterization of heterogeneities or scattering from surface seismograms, a detailed study of coda should be performed. Otherwise, properties as attenuation or anisotropy could be omitted.

In order to analyze in detail the influence of shear waves on the three-crack system and their surface seismic response, in Figure

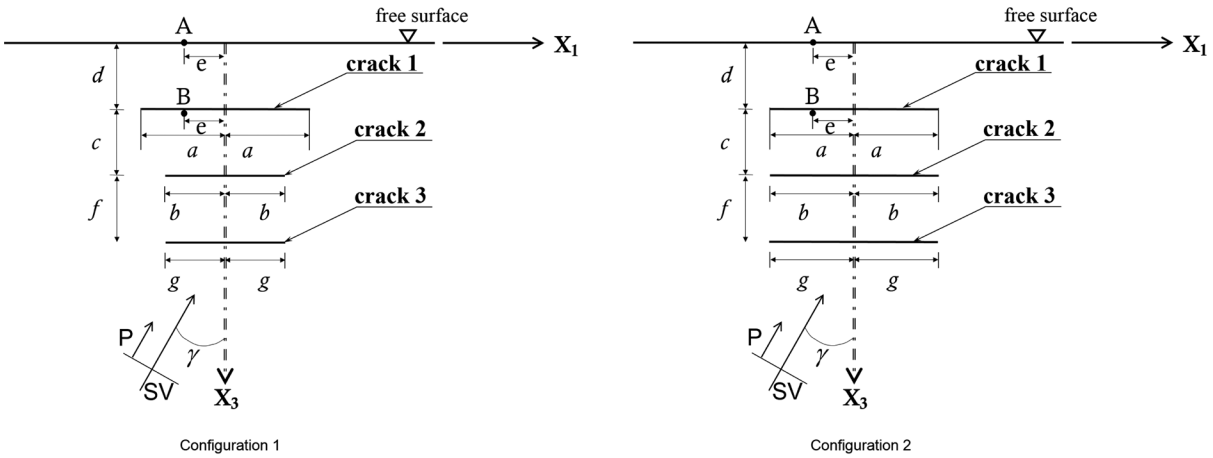

Figure 9 Two crack-model configurations that represent the elastic half-space containing three near free surface parallel cracks. The excitation is given by the incidence of P and SV waves. Configuration 1 shows three cracks with different lengths, while in configuration 2, three parallel cracks of same sizes are shown.

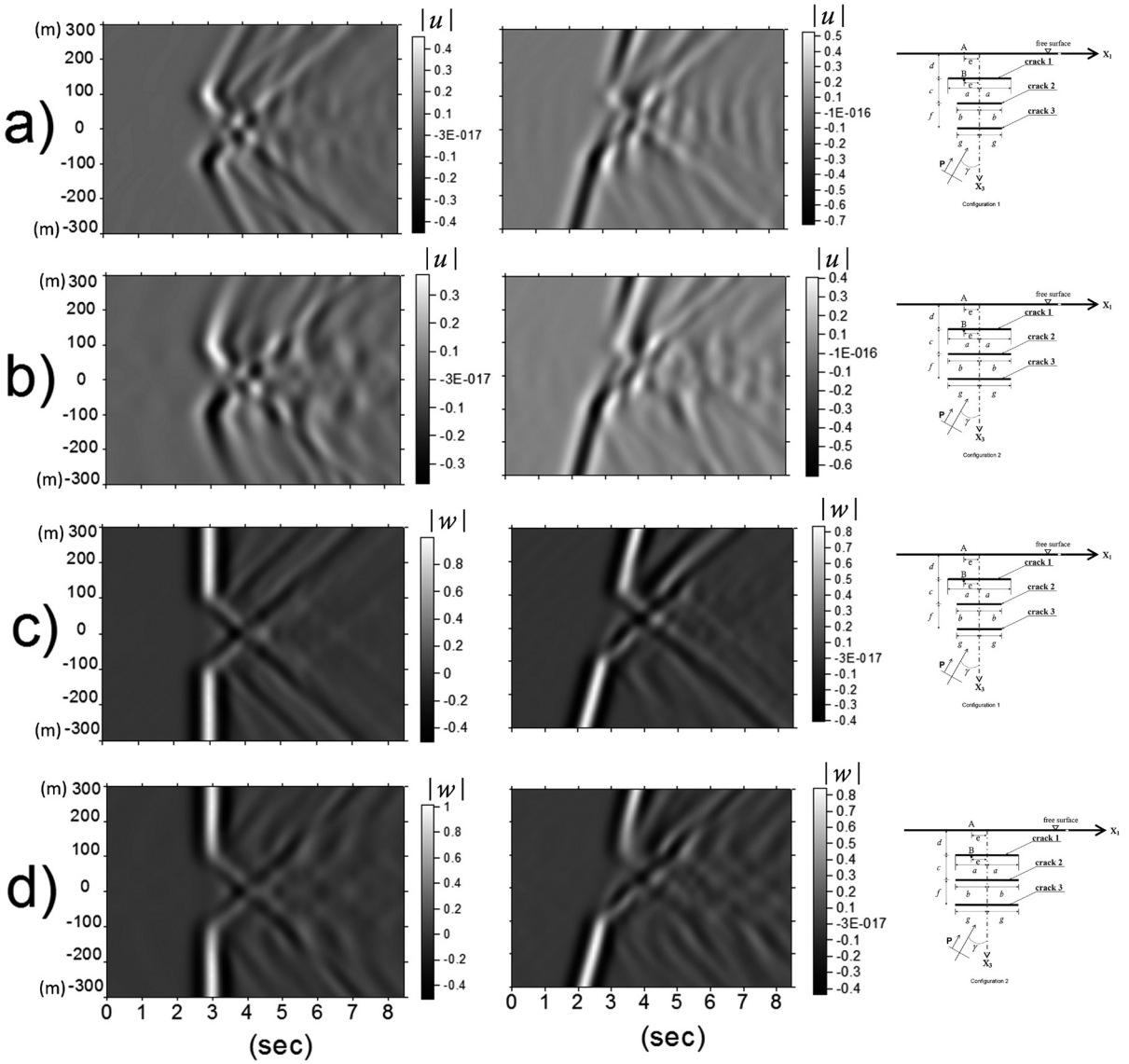

Figure 10. Synthetic seismograms of the displacement field for a line of surface receivers. Normalized horizontal displacements $|u|$ are shown in a) and b), while vertical ones $|w|$ in c) and d). The medium contains two different crack configurations, indicated at the right-hand side of the seismograms. The excitation is given by a normal (left) and oblique (right) P-wave incidence.

11 more analyses were executed for SV waves propagating with normal and oblique incidences, γ=0° and 30°, respectively. The results in Figure 11 are depicted in the same fashion as the previous case of incoming P waves (Figure 10). In general, the results obtained at the free surface for SV waves exhibit similar behavior compared with those observed for P waves. It is important to note in Figure 11, that the presence of a third crack does not give relevant information to identify its existence. Only a slight additional perturbation of SV waves for the three parallel cracks configuration and for both incidence angles is seen. These last set of results reinforce the previous partial interpretation; it is necessary to know and investigate the diffracted and scattered fields at the whole possible evaluation domains (a dense array of receivers and positions in time and frequency should be considered), otherwise, cracks behave like stronger reflectors of energy and their global effect can be poorly appreciated.

Concluding remarks

This article presents the application of the Indirect Boundary Element Method (IBEM) to calculate the response of a medium that contains a single, two or three near-free-surface-parallel cracks under the incidence of P and SV waves. The formulation presented here permits to treat the generated displacement fields by several interacting cracks with good efficiency. This numerical technique, which is based on an integral representation of the diffracted wave field, can be seen as a numerical accomplishment of the Huygens´ principle, since the diffracted waves are constructed at the boundaries and the cracks from where they are radiated. In order to validate the applicability of the IBEM to the problem of the propagation of elastic waves in cracked media, IBEM results reproduce very well those reported by Achenbach *et al*. (1983) for the case of a single near free surface parallel crack.

We studied six cases in the frequency domain and the impact in terms of scattering by the presence of one or two cracks was analyzed. A ratio b/a=0 (see Figure 1) means that crack 2 is not present and only one single crack is considered. In those cases, the horizontal displacements varying with frequency were compared with similar results obtained by Achenbach *et al*. (1983) and an excellent match was found. In addition, for ratios ranging $0<b/a\leq1.0$, the resonance peaks were controlled by the equivalent layer placed between crack 1 and the free surface and, vertical and horizontal displacements at point A were strongly affected at those resonance frequencies. However, when $b/a>1.0$ the resonance peak was dominated by the layer between crack 2 and the free surface. An extra resonance high frequency was detected which corresponds to a local resonant frequency of the virtual layer between crack 1 and the free surface (see Figure 4).

In all these cases, we have found that there are important difficulties to identify, in the frequency domain, the presence of a second crack located near to a free surface. This fact will be controlled by the characteristic excitation frequency range of the cracked medium and by the length of the second crack (see Figure 4). Moreover, for the particular case where crack 2 has a length of b/a=0.25, a time analysis was executed. It was observed that for both normal and oblique incidence of P waves, similar scattering patterns at the free surface are exhibited for the cases of single or two-near free surface parallel cracks. This observed feature leads to conclude that to identify the scattering effect caused by the presence of a second crack measured at the free surface in time domain, a detailed study of the multiple diffracted field by means of coda analysis or some amplitude decay methodology would be necessary; otherwise, important wave propagation phenomena as attenuation or anisotropy could be omitted.

Finally, two configurations containing three cracks excited by P and SV waves were analyzed. The results found also serious difficulties to extract information to identify the influence of the scattered field coming from the multiple patterns of the system. In fact, this set of results reinforce our interpretation that it is necessary to understand the diffracted and scattered fields generated in the whole model using results in both, frequency and time domains. In spite of this, cracks behave like stronger reflectors of energy and their global effect can be poorly appreciated and even more, as generally occurs in seismic studies, where measurements are only possible at the free surface.

Acknowledgements

This work was partially supported by Instituto Mexicano del Petróleo, under grants of The Shale Gas/Oil Project (Y.60021/Y.01001); by Fondo Sectorial CONACYT-SENER Hidrocarburos (FSCSH), under grant 205868. By CICYT Spain, under grants REN2002-04198-C02-02/RIES, by the European Community with FEDER and the research team RNM-194 of Junta de Andalucía, Spain. Some computations were performed at Instituto de Ingeniería-UNAM with partial support of DGAPA-UNAM, Mexico.

References

Achenbach J.D., Brind R.J., 1981, Scattering of surface waves by a sub-surface crack. *J. Sound Vibrat.*, 76, 43-56.

Achenbach J.D., Lin W., Keer L.M., 1983, Surface waves due to scattering by a near-surface parallel crack. *IEEE trans. Sonics Ultras.*, SU-30, 270.

Ávila-Carrera R., Rodríguez-Castellanos A., Sánchez-Sesma F.J., Ortiz-Alemán C., 2009, Rayleigh-wave scattering by shallow cracks using the indirect boundary element method, *J. Geophys. Eng.*, 6, 3, 221-230.

Ávila-Carrera R., Spurlin J.H., Valle-Molina C., 2011, Rayleigh-wave scattering by shallow cracks using the indirect boundary element method, *J. Geophys. Eng.,* 6, 3, 221-230.

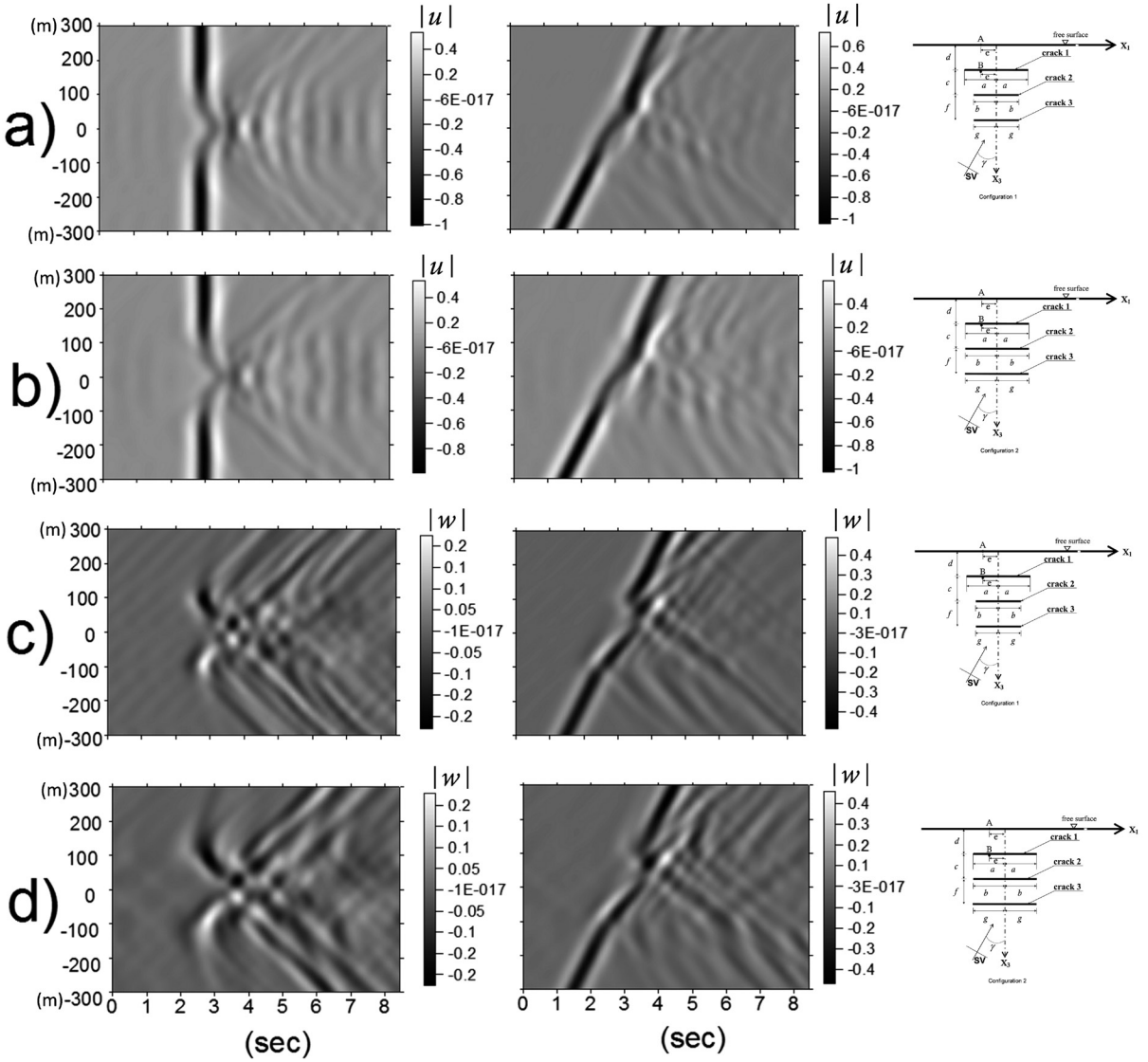

Figure 11 Synthetic seismograms of the displacement field for a line of surface receivers. Normalized horizontal displacements are shown in a) and b), while vertical ones $|w|$ in c) and d). The medium contains two different crack configurations, indicated at the right-hand side of the seismograms. The excitation is given by a normal (left) and oblique (right) SV-wave incidence.

Brajanovski M., Gurevich B., Schoenberg M., 2005, A model for P-wave attenuation and dispersion in a porous medium permeated by aligned fractured. *Geophys. J. Inter.*, 163, 572-384.

Brind R.J., Achenbach, J.D., 1981, Scattering of longitudinal and transverse waves by a sub-surface crack. *J. Sound Vib.,* 78, 555-563.

Dineva P., Manolis G.D., Rangelov T.V., 2006, Sub-surface Crack in Inhomogeneous Half-plane: Wave Scattering Phenomena by BEM, *Eng. Anal. Bound. Elem.*, 30, 350-362.

Hudson J.A., Liu E., Crampin S., 1996, The mechanical properties of materials with interconnected cracks and pores, *Geophys. J. Int.*, 124, 105-112.

Keer L.M., Lin W., Achenbach J.D., 1984, Resonance effects for a crack near a free surface. *J. Appl. Mech*., 51, 65-70.

Kupradze V.D., 1963, Dynamical problems in elasticity, In Progress in Solid Mechanics, I.N. Sneddon and R. Hill (Editors), North-Holland, Amsterdam. Vol., III,

Liu E., Crampin S., Booth D.C., 1989, Shear-wave splitting in cross-hole surveys: modeling, *Geophys.,* 54, 57-65.

Liu E., Crampin S., Queen J.H., 1991, Fracture detection using crosshole surveys and reverse vertical seismic profiles at the Conoco Borehole Test Facility, Oklahoma, *Geophys. J. Int.,* 107, 449-463.

Liu E., Crampin S, Queen J.H., Rizer W.D., 1993, Velocity and attenuation anisotropy caused by micrographs and macrofractures in a multiazimuthal reverse VSP, *Canadian J. Expl. Geophys.,* 29, 177-188.

Liu E., Crampin S., Hudson J.A., 1997, Diffraction of seismic waves by cracks with application to hydraulic fracturing, *Geophys.,* 62, 253-265.

Liu E., Zhang Z., Niu B, 1999, BEM simulation of multiple scattering of elastic waves by cracks, *Proc. Int. Conf. Boundary Element Techniques* July 1999, Queen Mary College, University of London, Ed. M.H. Aliabadi, 59-66.

Liu E., Queen J.H., Zhang Z., Chen D, 2000, Simulation of multiple scattering of seismic waves by spatially distributed inclusions, *Science in China Series E,* 43, 4-12.

Liu E., Zhang Z., 2001, Numerical Study of elastic wave scattering by cracks or inclusions using the boundary integral equation method, *J. Comp. Acous.* 9, 1039-1054.

Mendelsohn D.A., Achenbach J.D., Keer L.M., 1980, Scattering of elastic waves by a surface-breaking crack, *Wave motion*, 2, 277-292.

Pointer T., Liu E., Hudson J.A., 2000, Seismic wave propagation in cracked porous media, *Geophys. J. Int.,* 142, 199-231.

Rao M.V.M.S., Prasanna L.K.J., 2006, Amplitude distribution analysis of acoustic emissions and investigation of the development of brittle fracture in rock. *Indian J. of Pure and App. Phys.*, 44, 820-825.

Rodríguez-Castellanos A., Ávila-Carrera R., Sánchez-Sesma F.J., 2007, Scattering of Rayleigh-waves by surface-breaking cracks: An integral formulation, *Geofísica Internacional*,46, 241-248.

Sánchez-Sesma F.J., Campillo M., 1991, Diffraction of P, SV and Rayleigh waves by topographic features; a boundary integral formulation, *Bull. Seism. Soc. Am.*, 81, 1-20.

Sherman C.S., Rector J., Glaser S.D., 2013, Elastodynamic Simulation of Tunnel Detection Experiments in Heterogeneous Geological Media, *47th US Rock Mechanics/ Geomechanics Symposium,* June 23-26, San Francisco, CA, USA, ARMA, 13-614.

Tod S.R., Hudson J.A., Liu E., 2002, Modelling fluid flow in media containing bed limited cracks, *EAGE 64th Conf. and Exhib.,* Florence, Italy, Communication.

Yang P.S., Liu S.W., Sung J.C., 2008, Transient response of SH waves in a layered half-space with sub-surface and interactive cracks, *App. Math. Mod.*, 32, 595-609.